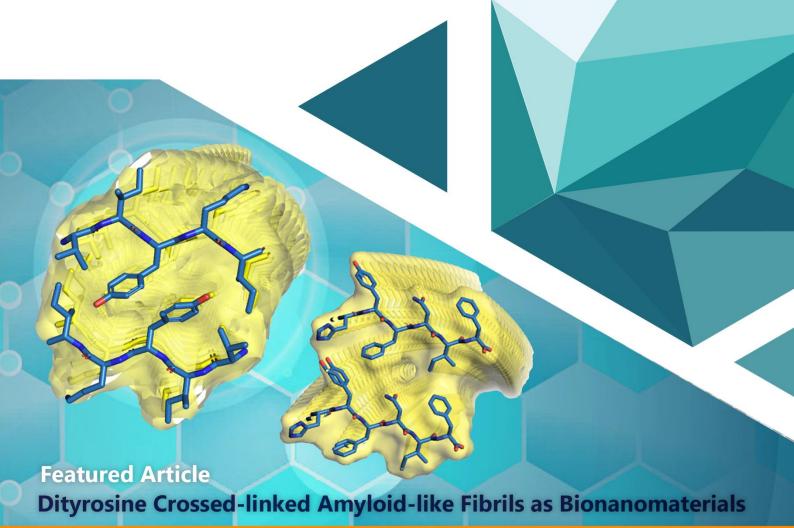
# raqi Journal of Nanotechnology IJN

synthesis and application

Year: 2020 Issue: 01



Academic Scientific Journals







# Iraqi Journal of Nanotechnology IJN

A scientific peer-reviewed journal published by AL-Sibd Center for Research and Scholarly Publishing

Issue: 01 Year: 2020

Address:

Iraq \_ Karbala \_ Imam Hussain Street Street No. 75 \_ House No. 4

Email address: ijn@srp-center.iq



# Editorial Board Editor in Chief



Asst. Prof. Dr. Yousif Khalaf Yousif

Ministry of Higher Education and Scientific Research - Iraq

### **Editorial Board Members**



Prof. Dr. Shamsoddin Mohajerzadeh

School of Electrical and Computer Engineering/ University of Tehran-Iran



Dr. Olusegun AMOS

Department of Science Laboratory Technology/ Kogi State Polytechnic/ Lokoja - Nigerian



Dr. Taghreed Hashim Al-Noor

University of Baghdad - Iraq



Dr. Ali T. Raissi

Florida Solar Energy Center / University of Central Florida - USA



Dr. Haider Hassan Alwan

Ministry of Oil - Iraq



Dr. Ali Hussain Rishak

Czech Technical University- Czech Republic



Dr. Alaa Abbas Fadhel
Al-Furat Al-Awsat Technical University - Iraq



Prem S. Thapa
University of Kansas-USA



Dr. Yahya Al-Khafaji University of Babylon - Iraq



Dr. Mohsin W. Yaseen

Ministry of Science and Technology - Iraq



Dr. Youssra Kareem

Mustansiriyah University - Iraq



Dr. Alaa Ali Hussain

Ministry of Higher Education and Scientific Research - Iraq



Dr. Alaa Jabbar Ghazai Al-Nahrain University- Iraq



Dr. Abbas Khammas Hussein

Director of Nanotechnology and Advance Materials Research Center



Dr. Ali Mohammed Al Mafarage ministry of electricity, iraq



Dr.Luma Majeed Ahmed Kerbala University, iraq

### introduction

Nanotechnology is going to be a main pushing factor behind the continuing technological revolution in the 21st century. Today, modernization is not limited to the tech sector development and its infrastructure, but also to the numbers of researchers, applications of nanoscience, in addition to Nanotechnology Characterization Laboratories (NCL), which have the potential of producing new materials and products that may revolutionize all areas of life.

Iraq, as a developing country, has suffered, for decades, from war and international isolation that have caused research and publication to fall behind in publishing high-quality academic articles, particularly in the cutting-edge area of nanotechnology, compared to other countries.

Hence, Al-Sibt center has set a distinctive goal to develop a research and establish a multidisciplinary journals managed by several academic professional and specialized industry experts in an attempt to bridge the research gap between Iraq and other developed countries. Consequently, the Iraqi Journal of Nanotechnology (IJN) is dedicated to publishing the most influential, innovative articles and applying some emerging nanotechnologies to areas fundamental to building technologically advanced and sustainable civilization; including such diverse areas as:

- Synthesis and Self-Assembly of Nanostructured Materials, Films Functionalization, Size-Dependent Properties of Nanocrystals, and Quantum Dots and Nanowires.
- Processing and Templating of Nanotubes and Nanoporous Materials.
- Tailoring of Polymeric Nanoparticles, Organic-Inorganic Nanocomposites and Biohybrids.
- Fabrication of Nano and Micro Electro Mechanical Systems.
- Design and Engineering of Structural and Functional Nanomaterials.
- Nanosystems for Biological, Medical, Chemical, Catalytic, Energy and Environmental Applications.
- Nanodevices for Electronic, Photonic, Magnetic, Imaging, Diagnostic and Sensor Applications.

### introduction count.

Nanotechnology is going to be a main pushing factor behind the continuing technological revolution in the 21st century. Today, modernization is not limited to the tech sector development and its infrastructure, but also to the numbers of researchers, applications of nanoscience, in addition to Nanotechnology Characterization Laboratories (NCL), which have the potential of producing new materials and products that may revolutionize all areas of life.

Iraq, as a developing country, has suffered, for decades, from war and international isolation that have caused research and publication to fall behind in publishing high-quality academic articles, particularly in the cutting-edge area of nanotechnology, compared to other countries.

Hence, Al-Sibt center has set a distinctive goal to develop research and establish multidisciplinary journals managed by several academic professional and specialized industry experts in an attempt to bridge the research gap between Iraq and other developed countries. Consequently, the Iraqi Journal of Nanotechnology (IJN) is dedicated to publishing the most influential innovative articles and applying some emerging nanotechnologies to areas fundamental to building technologically advanced and sustainable civilization; including such diverse areas as:

- Synthesis and Self-Assembly of Nanostructured Materials, Films Functionalization, Size-Dependent Properties of Nanocrystals, and Quantum Dots and Nanowires.
- Processing and Templating of Nanotubes and Nanoporous Materials.
- Tailoring of Polymeric Nanoparticles, Organic-Inorganic Nanocomposites and Biohybrids.
- Fabrication of Nano and Micro Electro Mechanical Systems.
- Design and Engineering of Structural and Functional Nanomaterials.
- Nanosystems for Biological, Medical, Chemical, Catalytic, Energy and Environmental Applications.
- Nanodevices for Electronic, Photonic, Magnetic, Imaging, Diagnostic and Sensor Applications.

## Aims & Scope

The Iraqi Journal of Nanotechnology (IJN) is an international, open access, peer-reviewed journal published by Al-sibd center for research and scholarly publishing. IJN is the first journal focusing on a top-notch topics like Nanotechnology in Iraq. The journal designed to represent and make the Iraqi universities research activities internationally visible and accessible.

IJN offers a multidisciplinary source of information in all subjects and topics that focuses on the science of nanotechnology in a wide range of industrial and academic applications and the most significant advancements in science.

IJN provides an ideal forum for presenting original reports of theoretical and experimental nanoscience and nanotechnology research. The journal publishes original articles in the following areas:

- 1- Nanomaterials and Nanocomposites
- 2- Nanodevices and Nanosensors
- 3- Nanotechnology in fuel and energy
- 4- Nanotechnology in green chemistry
- 5- Nanomedicine

# Reviewers' Responsibilities

Reviewers are required to provide written, competent and unbiased feedback in a timely manner on the scholarly merits and the scientific value of the manuscript.

The reviewers assess manuscript for the compliance with the profile of the journal, the relevance of the investigated topic and applied methods, the originality and scientific relevance of information presented in the manuscript, the presentation style and scholarly apparatus.

Reviewers should alert the Editor to any well-founded suspicions or the knowledge of possible violations of ethical standards by the authors. Reviewers should recognize relevant published works that have not been cited by the authors and alert the Editor to substantial similarities between a reviewed manuscript and any manuscript published or under consideration for publication elsewhere, in the event they are aware of such. Reviewers should also alert the Editor to a parallel submission of the same manuscript to another journal, in the event they are aware of such.

Reviewers must not have conflict of interest with respect to the research, the authors and/or the funding sources for the research. If such conflicts exist, the reviewers must report them to the Editor without delay.

Any selected referee who feels unqualified to review the research reported in a manuscript or knows that its prompt review will be impossible should notify the Editor without delay.

Reviews must be conducted objectively. Personal criticism of the author is inappropriate. Reviewers should express their views clearly with supporting arguments.

Any manuscripts received for review must be treated as confidential documents. Reviewers must not use unpublished materials disclosed in submitted manuscripts without the express written consent of the authors. The information and ideas presented in submitted manuscripts shall be kept confidential and must not be used for personal gain.

## **Authors' Responsibilities**

Authors warrant that their manuscript is their original work, that it has not been published before and is not under consideration for publication elsewhere. Parallel submission of the same manuscript to another journal constitutes a misconduct and eliminates the manuscript from consideration by Iraqi Journal of Nanotechnology.

In case a submitted manuscript is a result of a research project, or its previous version has been presented at a conference in the form of an oral presentation (under the same or similar title), detailed information about the project, the conference, etc. shall be provided in a footnote / Acknowledgments. A paper that has already been published in another journal cannot be reprinted in Iraqi Journal of Nanotechnology.

It is the responsibility of each author to ensure that manuscripts submitted to Iraqi Journal of Nanotechnology are written with ethical standards in mind. Authors affirm that the manuscript contains no unfounded or unlawful statements and does not violate the rights of third parties. The Publisher will not be held legally responsible should there be any claims for compensation.

#### Reporting standards

A submitted manuscript should contain sufficient detail and references to permit reviewers and, subsequently, readers to verify the claims presented in it. The deliberate presentation of false claims is a violation of ethical standards.

Authors are exclusively responsible for the contents of their submissions and must make sure that they have permission from all involved parties to make the data public.

Authors wishing to include figures, tables or other materials that have already been published elsewhere are required to obtain permission from the copyright holder(s). Any material received without such evidence will be assumed to originate from the authors.

# **Editorial Responsibilities**

The Editor-in-Chief is responsible for deciding which articles submitted to Iraqi Journal of Nanotechnology will be published. The Editor-in-Chief is guided by the Editorial Policy and constrained by legal requirements in force regarding libel, copyright infringement and plagiarism.

The Editorial Board reserves the right to decide not to publish submitted manuscripts in case it is found that they do not meet relevant standards concerning the content and formal aspects. The Editorial Staff will inform the authors whether the manuscript is accepted for publication within two weeks from the date of the manuscript submission.

Editor must hold no conflict of interest with regard to the articles they consider for publication. If an Editor feels that there is likely to be a perception of a conflict of interest in relation to their handling of a submission, the selection of reviewers and all decisions on the manuscript shall be made by the editor.

Editorial Board shall evaluate manuscripts for their intellectual content free from any racial, gender, sexual, religious, ethnic, or political bias.

The Editor and the Editorial Staff must not use unpublished materials disclosed in submitted manuscripts without the express written consent of the authors. The information and ideas presented in submitted manuscripts shall be kept confidential and must not be used for personal gain.

# Copyright

Authors retain copyright of the published papers and grant to the publisher the non-exclusive right to publish the article, to be cited as its original publisher in case of reuse, and to distribute it in all forms and media. Articles will be distributed under the Creative Commons CC BY 4.0 license, the terms and condition is available on: https://creativecommons.org/licenses/.

Authors may enter the separate, additional contractual arrangements for non-exclusive distribution of the journal published paper (e.g., post it to an institutional repository or publish it in a book), with an acknowledgement of its initial publication in this journal.

# **Authorship**

Authors must make sure that all only contributors who have significantly contributed to the submission are listed as authors and, conversely, that all contributors who have significantly contributed to the submission are listed as authors. If persons other than authors were involved in important aspects of the research project and the preparation of the manuscript, their contribution should be acknowledged in a footnote or the Acknowledgments section.

### **Conflict of interest**

Authors should disclose in their manuscript any financial or other substantive conflict of interest that might have influenced the presented results or their interpretation.

# **Open Access Policy**

Iraqi Journal of Nanotechnology is an Open Access Journal. All articles can be downloaded free of charge under the CC BY 4.0 License.

The journal does not charge any fees at submission, reviewing, and production stages.

#### **Peer Review**

The submitted manuscripts are subject to a peer review process. The purpose of peer review is to assists the Editorial Board in making editorial decisions and through the editorial communication with the author it may also assist the author in improving the manuscript.

This journal uses double-blind review, which means that both the reviewer and author identities are concealed from the reviewers, and vice versa, throughout the review process.

The choice of reviewers is at the Editors' discretion. The reviewers must be knowledgeable about the subject area of the manuscript; they must not be from the authors' own institution and they should not have recent joint publications with any of the authors.

All of the reviewers of a manuscript act independently and they are not aware of each other's identities. If the decisions of the two reviewers are not the same (accept/reject), the Editor may assign additional reviewers.

During the review process Editor may require authors to provide additional information (including raw data) if they are necessary for the evaluation of the scholarly merit of the manuscript. These materials shall be kept confidential and must not be used for personal gain.

The Editorial team shall ensure reasonable quality control for the reviews. With respect to reviewers whose reviews are convincingly questioned by authors, special attention will be paid to ensure that the reviews are objective and high in academic standard. When there is any doubt with regard to the objectivity of the reviews or quality of the review, additional reviewers will be assigned.

# Procedures For Dealing With Unethical Behavior

Anyone may inform the editors and/or Editorial Staff at any time of suspected unethical behavior or any type of misconduct by giving the necessary information/evidence to start an investigation.

#### Investigation

- Editor-in-Chief will consult with the Editorial Board on decisions regarding the initiation of an investigation.
- During an investigation, any evidence should be treated as strictly confidential and only made available to those strictly involved in investigating.
- The accused will always be given the chance to respond to any charges made against them.
- If it is judged at the end of the investigation that misconduct has occurred, then it will be classified as either minor or serious.

#### Minor misconduct

Minor misconduct will be dealt directly with those involved without involving any other parties, e.g.:

- Communicating to authors/reviewers whenever a minor issue involving misunderstanding or misapplication of academic standards has occurred.
- A warning letter to an author or reviewer regarding minor misconduct.

# Procedures For Dealing With Unethical Behavior, count.

#### Major misconduct

The Editor-in-Chief, in consultation with the Editorial Board, and, when appropriate, further consultation with a small group of experts should make any decision regarding the course of action to be taken using the evidence available. The possible outcomes are as follows (these can be used separately or jointly):

- Publication of a formal announcement or editorial describing the misconduct.
- Informing the author's (or reviewer's) head of department or employer of any misconduct by means of a formal letter.
- The formal, announced retraction of publications from the journal in accordance with the Retraction Policy (see below).
- A ban on submissions from an individual for a defined period.
- Referring a case to a professional organization or legal authority for further investigation and action.

When dealing with unethical behavior, the Editorial Staff will rely on the guidelines and recommendations provided by the Committee on Publication Ethics (COPE): http://publicationethics.org/resources/.

### **Retraction Policy**

Legal limitations of the publisher, copyright holder or author(s), infringements of professional ethical codes, such as multiple submissions, bogus claims of authorship, plagiarism, fraudulent use of data or any major misconduct require retraction of an article. Occasionally a retraction can be used to correct errors in submission or publication. The main reason for withdrawal or retraction is to correct the mistake while preserving the integrity of science; it is not to punish the author.

Standards for dealing with retractions have been developed by a number of library and scholarly bodies, and this practice has been adopted for article retraction by Iraqi Journal of Nanotechnology in the electronic version of the retraction note, a link is made to the original article. In the electronic version of the original article, a link is made to the retraction note where it is clearly stated that the article has been retracted. The original article is retained unchanged, save for a watermark on the PDF indicating on each page that it is "retracted."

### Disclaimer

The views expressed in the published works do not express the views of the Editors and Editorial Staff. The authors take legal and moral responsibility for the ideas expressed in the articles. Publisher shall have no liability in the event of issuance of any claims for damages. The Publisher will not be held legally responsible should there be any claims for compensation.

# **Acknowledgment of Sources**

Authors are required to properly cite sources that have significantly influenced their research and their manuscript. Information received in a private conversation or correspondence with third parties, in reviewing project applications, manuscripts and similar materials, must not be used without the express written consent of the information source.

# **Plagiarism**

Plagiarism, where someone assumes another's ideas, words, or other creative expression as one's own, is a clear violation of scientific ethics. Plagiarism may also involve a violation of copyright law, punishable by legal action.

Plagiarism includes the following:

- •Word for word, or almost word for word copying, or purposely paraphrasing portions of another author's work without clearly indicating the source or marking the copied fragment (for example, using quotation marks);
- •Copying equations, figures or tables from someone else's paper without properly citing the source and/or without permission from the original author or the copyright holder.

Please note that all submissions are thoroughly checked for plagiarism by turnitin.

Any manuscript that shows obvious signs of plagiarism will be automatically rejected.

In case plagiarism is discovered in a paper that has already been published by the journal, it will be retracted according to Retraction policy.

# Fundamental errors in published works

When an author discovers a significant error or inaccuracy in his/her own published work, it is the author's obligation to promptly notify the journal Editor or publisher and cooperate with the Editor to retract or correct the paper.

By submitting a manuscript, the authors agree to abide by the Iraqi Journal of Nanotechnology's Editorial Policies.

# **Self-archiving Policy**

The Iraqi Journal of Nanotechnology allows authors to deposit pre-print in an institutional repository and non-commercial subject-based repositories or to publish it on Author's personal website (including social networking sites, such as ResearchGate, Academia.edu, etc.) and/or departmental website, at any time after acceptance for publication Full bibliographic information (authors, article title, journal title, volume, issue, pages) about the original publication must be provided and a link must be made to the article's DOI.

# Index

Title	page
Editorial Board	iii
introduction	V
Aims & Scope	vii
Reviewers' Responsibilities	viii
Authors' Responsibilities	ix
Editorial Responsibilities	х
Copyright	хi
Authorship	xi
Conflict of interest	хi
Open Access Policy	хi
Peer Review	xii
Procedures For Dealing With Unethical Behavior	xiii
Retraction Policy	χv
Disclaimer	χv
Acknowledgment of Sources	xv
Plagiarism	xvi
Fundamental errors in published works	xvii
Self-archiving Policy	xvii
index	xviii
Design and On-Line Test of Nano Electro-Mechanical Switch	1
A Review of Important Prerogatives Using of Atmospheric- Pressure Plasma Jet to Sterilize Hospitals and Quarantine Room to Reduce the Spread of Diseases in Iraq	7
Effect of silver doping on structural and photocatalytic circumstances of ZnO nanoparticles	13
Synthesis and Characteristics of (PAV-PAVC-Ti) Nanocomposites	23
Dityrosine Crossed-linked Amyloid-like Fibrils as Bionanomaterials	31
Optical and Structural Properties of CdS Quantum Dots Synthesized Using (MW-CBD) Technique	44
Effect of Nano-coating on Molten Salts for Turbine Blades	53
Controlling the Tube Diameter of SWCNTs Using High Melting Point Promotors	64
(Au, Ag)/Alo.o8Ino.o8Gao.84N/ (Au, Ag) Metal-semiconductor- metal (MSM) Photodetectors	72



# Iraqi Journal of Nanotechnology synthesis and application



Journal Homepage: https://publications.srp-center.iq/index.php/ijn

#### Design and On-Line Test of Nano Electro-Mechanical Switch

#### Maha Khalid Kadhim<sup>1</sup>, Waleed Khalid Kadhim<sup>2</sup>, Maryam Adnan Al-Ethary<sup>3</sup>

- 1- Ministry of Higher Education & Scientific Research, University of Karbala, College of Engineering, Department of Biomedical Engineering, Karbala, Iraq, E-mail: <a href="mailto:maha.k@uokerbala.edu.iq">maha.k@uokerbala.edu.iq</a>.
- 2- Waleed Khalid Kadhim, Ministry of education, Directorate of Education Babylon, Hilla, Iraq, E-mail: Welidkalid37@gmail.com.
- 3- Maryam Adnan Al-Ethary, Ministry of education, Directorate of Education Babylon, Hilla, Iraq, E-mail: mariem20132420@gmail.com.

#### **Keywords:**

Nano-electro-mechanical System (NEMS);

Creep;

Wear; Crack;

On-line monitoring;

Bias superposition test.

#### **Abstract**

In this paper, Nano Electro-Mechanical Switch (NEMS) was designed and simulated by using MATLAB simulation, then was tested by the on-line test through bias super-position. This switch has 4.5 nm thickness, offers low power dissipation, and permits nonstop observing of all essential jobs. On the other hand, some challenges are facing this Nano system. One of them is very difficult to resonators collective products with the same characteristics. The fabrication process was also complex and much hardness occurred during repetitive operations, which failure and stiction caused problems. In this work, a comparison between the response of a fault-free system and the system with some failures has been carried out. The test results showed a decrease in pullin voltage with increasing overlap area as a result of wear failure mechanism in Nano Switch (NS). Creep in (NS) affected the value of the young modules and this increased the output voltage, also the crack in the beam of (NS) increased the effective mass and decreased output signal.

#### Introduction

There are many kinds of test techniques, have been used for integrated sensors such as Software-Based Self-test (SBST), System-On-Chip (SOC) testing, Built-in self-test (BIST), on-line test through bias superposition, electro-thermal stimulus test, etc. These tests are employed to detect errors and faults that appear during the system operation and affect the response of the device. Also, they indicate that the system in failure mode, which decreases the effectiveness of the mechanism.

All previous checks can be also separated into (On-line and Off-line) tests [1]. System-On-Chip (SOC) test and Built-in self- test (BIST) can be done when the device is offline, immediate the test cannot be operated under normal condition and have dangers in its output waveform if the medium is uncontrolled and perturbed. Heating the structure through the dispersing element is the way used to test the cantilever structure of the electro-thermal stimulus. These kinds of tests are called off-line because they cannot be performed during the work of the sensors [1, 2].

SBST and Wavelet-Analysis of Measurements (WAM) are online tests but with difficult and complex steps. In this paper, the NEM switch was monitored on-line by utilizing the bias superposition method to test it this technique was named online test through bias superposition. In this technique, the check signal (second signal) was added to the measurement input signal (carrier or first signal) by using an adder so the characteristics of the first signal must be selected differently from the characteristics of the second signal.

Furthermore, the second signal needs to exist chosen exclusive the bandwidth of the switch [3]. This manner is a low-cost way, simple, and is utilized to escape troubles in switch results, ensuring that the test result depends totally on the result of the first input rather than the exterior things induced by [1, 2]. Several researches are utilized this test method to check different types of Micro Electro Mechanical Systems (MEMSs) where on-line monitoring bias superposition method for

integrated micro capacitive accelerometer (2.6mm2.6mm) accelerometer area with 10 thick of accelerometer mass) was presented [4].

When the device operates without any fault then it is called the first case and if a defect was adopted, it is called the second case, however, the effect of disturbances caused by the environment in this work was not taken into consideration. Therefore, the system proposed by [5] in which the on-line test method through bias superposition is used with a micro accelerometer that has an area equal (2.6 mm×2.6 mm) and with 100 thick accelerometer mass. In this paper, disturbance due to the surrounding environment is considered when the thick of the Nano accelerometer mass is 3.3nm.

#### **Principles of Bias Superposition**

Figure 1 illustrates the general structure for the bias superposition technique where the test stimulus is placed inside the configuration of the Nanoelectromechanical switch to check if it works normally and gives us accurate outcomes or not because of a certain kind of failure mechanism. The bias superposition technique is a simple and low-cost method because it does not require modifications to the design of the device to generate the stimulus.

Typically, a square wave signal with half of the period is ON (duty cycle is 50%) and is utilized as a second signal. This second signal (test signal) is modulated with an input signal (duty cycle is 70%). It can be recognized that the output of test signal is non-ideal and need filtration; therefore, suitable filters are required to extract the acceptable output information [5]. Then to know this sensor is worked without any defect and is offered the correct outcome or not due to a certain kind of defect. We make a comparison between the two test signals and if the output signal of two cases is similar in phase, amplitude, and frequency, this means Nano switch (NS) has no-fault and operates with no defect otherwise the device operates with fault.

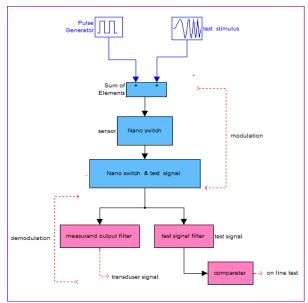


Figure 1 Test of (NS) including Bias Superposition

#### Nano Electromechanical switch

#### Overview

In this paper, the NEM switch was taken as a case study. This switch consists of two parallel plates (movable and fixed) with three-terminals; drain, source, and gate, and an actuation gap (go) that separates these two parallel plates of the electrostatic switch [6, 7]. Figure 2 illustrates the generic three-terminal electrostatic switch.

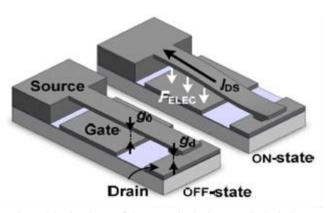


Figure 2 basic Planar of three-terminal Electrostatic Switch [7]

#### **Principle of Operation**

The principle of electro-mechanical devices operation is the electrostatic attractive force produced due to voltage applied across the plates and this will accelerate the movable electrode toward the fixed electrode. The area of the two electrodes and the actuation gap, which splits electrodes, are factors on which the weakness of the electrostatic attractive force depends [3, 8]. Another force impact on the electromechanical device is spring force produced because the moveable part is suspended by a spring, so it has an elastic constant.

In general, electro-mechanical switches have ON and OFF states. The current, from source to drain is limited and near to zero leakage current due to the air gap between drain and source. Therefore, the current does not move from one electrode to another, and the device in the OFF state. During the OFF state, Vgs (voltage between gate and source) is smaller than the release voltage (the voltage that is needed in order to pull-out the device) [9]. If electrostatic force overcomes spring force this leads to providing a conductive path for current to flow and the device becomes in an ON state.

#### Mathematical Model of Nano Electromechanical Switch

A second-order spring-mass-damper system equation has been utilized to define the mechanical model of the Nanoelectromechanical switch, at what time we applied voltage between the first electrode (drain) and the second electrode (source). Translate of a mobile part in nano switch is overseen with the aid of equation (1).

Nonlinear  $2^{nd}$  order differential structure can be expressed by utilizing three factors, namely: the inertial proof mass m, nonlinear viscous damping b, and spring constant k, [10-14].

$$F_{ele}(\mathbf{X}) + F_{vdw}(\mathbf{X}) = m_{eff} \ddot{\mathbf{X}} + \frac{\sqrt{Km_{eff}}}{Q} \dot{\mathbf{X}} + KX$$
 (1)

Where:  $F_{ele}$ : Electrostatic force,  $F_{vdw}$ : Van der Waals' force,  $m_{eff}$ : is the effective mass,

X: displacement of a gate in Nano switch, Q: quality factor  $[10^3-10^4]$ , K is spring constant

#### Simulink Model of NEMS

The system shown in Figure 3 was modeled in MATLAB / Simulink, input square wave signal (70% duty cycle) with 10 HZ frequency of input signal. This signal is multiplied by 9.81 gains to give us an equivalent acceleration by utilizing equation (2).

$$\mathbf{a} = \left(\frac{V^2}{2}\right) \frac{\partial \mathbf{c}}{\partial \mathbf{x}} \tag{2}$$

Where: v is the input voltage, x is the displacement of the gate and c denotes capacitance and can be calculated by equation (3).

$$c=\frac{\varepsilon_o\varepsilon_r}{x} \frac{\textit{A}}{\textit{X}} \tag{3}$$
 As displayed in Fig 3, the square first signal (input) before amplification could be gotten.

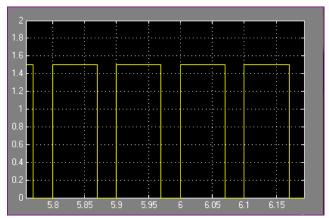


Figure 3 Waveform of First Signal (Input Signal)

Nano switch test process provides an on-line test by using a bias superposition method, this process is active when the second signal is put in the construction of NEMS to test it, if it works without any fault and results in the right outputs or not due to some kind of fault. Then the output is filtered by a Butterworth structure of a second-order high pass filter with a cutoff frequency equal to 100 Hz was designed to remove unwanted signals and get input signal as shown in Figure 4.

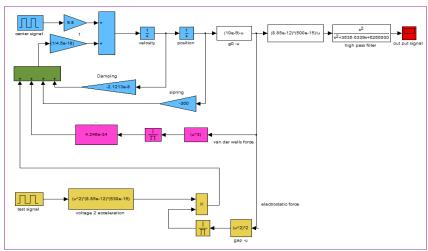


Figure 4 the Simulink Model of Nano Electromechanical Switch

#### Nano Electromechanical Switch (NEMS) Simulation Test Results

The output characteristics of the above model (NEMS) are presented in Figure 5 (without any defect), are tested by employing an on-line test through the bias superposition method. The influence of wear, fracture, creep, and crack is considered in this test. Where a square wave is entered to this model, a 1.5 V peak amplitude, for 70% of the cycle, will activate the ON state and a 0 V, for 30% of the cycle, will activate the OFF state. The output wave of this model can be seen with two levels, the high level is 2.55\*10<sup>-22</sup> V denoting the ON state, while the low level is roughly equal to zero denoting to OFF state. This outcome can be offered when the Nano switch normally works (without failure mechanism).



Figure 5 Output of Nano Switch without any defect

To test Nano switch whether it works in failure mode or not, a comparison must be carried out between the output signal of Nano switch (under testing) and the output signal when the switch runs normally. If the two signals have the same frequency, identical in phase, and equal in amplitude, this signalizes that the switch operates without any fault while any difference in these three properties is attributed to some defects or failures in the Nano switch.

#### Creep in Nano Electromechanical Switch

The creep in the switch variation spring factor k affects the value of the young modules E. This will alternate the response of Nanoelectromechanical switch, when the spring factor increases from  $10 \text{ Nm}^{-1}$  to  $500 \text{ Nm}^{-1}$ , this leads to an increase in the level of output voltage from  $1.14*10^{-23} \text{ V}$  to  $2.5*10^{-22} \text{ V}$  as seen in **Error! Reference source not found.**.

#### Wear in Nano Electromechanical Switch

The corrosive in Nanoelectromechanical switch, because of the environmental impacts, will result in wear in the switch and impact on the system parameters (effective mass and damping factor), then will decrease pull-in voltage accordingly to increase in overlapped area between gate and electrode body as shown in **Error! Reference source not found.** 

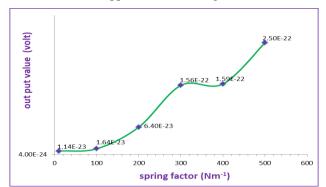


Figure 6 increasing in the output of Nano switch due to an increase in the value of spring Factor

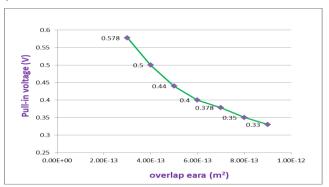


Figure 7 Inverse proportionality between pull-in voltage and overlap area

#### **Cracks in Nano Electromechanical Switch**

The crack in the beam of Nano switch affects resonance frequency and stiffness and leads to an increase in the effective mass also variates in the response of Nano switch. Figure 8 shows a reduction in the response of the Nano switch from 5\*10<sup>-16</sup> V to 3.89\*10<sup>-17</sup> V when the effective mass increased from 6.5\*10<sup>-18</sup> to 6.9\*10<sup>-18</sup> g this change in response denoted that the Nano switch works in failure mode due to the crack in its beam.

Figure 9 explains that the resonant frequency is changed due to increasing the effective mass, where decreasing the resonant frequency leads to increasing the time that is required to change the state of Nano switch from ON to OFF and this will decrease the speed of Nano switch.

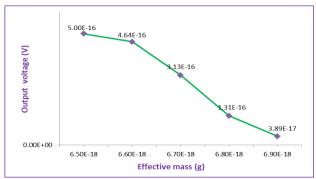


Figure 8 decreasing output signal because of increasing effective mass

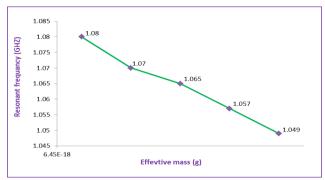


Figure 9 Resonant Frequency is decreased when the effective mass is increased from 6.5\*10-18 g to 6.9\*10-18 g

#### Conclusion

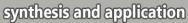
The nanoelectromechanical switch had been modeled in MATLAB/ Simulink and then had been tested by utilizing an online test through a bias superposition technique. Here, there is no need for any modifications to the switch to apply this test technique. Only the test signal was injected in the bias structure of the sensor to achieve the correct test operation. Low cost and on-line test capability were presented. Therefore, this test technique had been used. Downsizing of the switch in the Nano scale was led to increasing the random collision of air molecules, ultra-small mass and Van der Waals had been great affected in this design. The test results showed Wear and Crack in the beam of Nano switch (NS) was increased the effective mass and was decreased output signal. While Creep in Nano switch (NS) was led to increasing output signal.

#### References

- [1] Rieth, M. and W. Schommers, Handbook Of Theoretical And Computational Nanotechnology. Volume 7: Magnetic Nanostructures And Nano-Optics. 2007: American Scientific Publishers.
- [2] Lyshevski, S.E., Nano-and micro-electromechanical systems: fundamentals of nano-and microengineering. 2018: CRC press.
- [3] Alrudainy, H., A. Mokhov, and A. Yakovlev. A scalable physical model for nano-electro-mechanical relays. in 2014 24th International Workshop on Power and Timing Modeling, Optimization and Simulation (PATMOS). 2014. IEEE.
- [4] Jeffrey, C., et al., Sensor testing through bias superposition. Sensors and Actuators A: Physical, 2007. 136(1): p. 441-455.
- [5] Dumas, N., et al., Online testing of MEMS based on encoded stimulus superposition. Journal of Electronic Testing, 2008. 24(6): p. 555-566.
- [6] Pott, V., et al., Mechanical computing redux: Relays for integrated circuit applications. Proceedings of the IEEE, 2010. 98(12): p. 2076-2094.
- [7] Liu, T.-J.K., et al. Prospects for MEM logic switch technology. in 2010 International Electron Devices Meeting. 2010. IEEE.
- [8] Alzoubi, K.A., Nano-Electro-Mechanical Switch (NEMS) for ultra-low power portable embedded system applications: Analysis, design, modeling, and circuit simulation. 2010, Case Western Reserve University.
- [9] Vaddi, R., et al., Design, modeling and simulation of an anchorless nano-electro-mechanical nonvolatile memory. 2012.
- [10] Dinarvand, A.-m., N. Dinarvand, and M.K.Q. Joogh, Behavioral Modeling and Simulation of an Open-loop MEMS Capacitive Accelerometer with the MATLAB/SIMULINK. parameters, 2014. 7: p. 2.
- [11] Spencer, M., et al., Demonstration of integrated micro-electro-mechanical relay circuits for VLSI applications. IEEE Journal of Solid-State Circuits, 2010. 46(1): p. 308-320.
- [12] Fraden, J., Handbook of modern sensors: physics, designs, and applications. 2004: Springer Science & Business Media.
- [13] Nathanael, R., Nano-electro-mechanical (NEM) relay devices and technology for ultra-low energy digital integrated circuits. 2013, CALIFORNIA UNIV BERKELEY DEPT OF ELECTRICAL ENGINEERING AND COMPUTER SCIENCE.
- [14] Mucheru, G., Operation of Gyro sensor and 3-axis Accelerometer: Scc 1300 gyro combo sensor. 2014.



# Iraqi Journal of Nanotechnology





Journal Homepage: https://publications.srp-center.iq/index.php/ijn

# A Review of Important Prerogatives Using of Atmospheric-Pressure Plasma Jet to Sterilize Hospitals and Quarantine Room to Reduce the Spread of Diseases in

#### Ahmed Abed Anber<sup>1</sup>, Mohammed Shaalan Essa<sup>2</sup>, Hiba Nabeel Abbas<sup>3</sup>

- 1- Al-Karkh University of Science, College of Energy and Environmental Sciences, Department of Renewable Energy Science, Baghdad, Iraq, E-mail: <a href="mailto:ahmedkrm88@gmail.com">ahmed.abed@kus.edu.iq</a>.
- 2- Ministry of Science and Technology, Renewable Energy Directorate, Solar Energy Research Center, Baghdad, Iraq.
- 3- Al-Karkh University of Science, College of Science, Department of microbiology, Baghdad, Iraq.

#### **Keywords:**

Atmospheric –pressure plasma jet system; Pathogenic bacteria; Nanostructured materials.

#### **Abstract**

Today, the world lives in the worst conditions because of the outbreak of bacteria and an increase in the number of people infected with the different diseases due to contact of minerals, wood, papers, hospitals, and laboratories. The physical devices used can support the current crisis and can be used as tools for sterilization and reducing the spread of the diseases. The methods that have been used to prepare nanostructured materials to play an important role in the biological and medical fields, because very tiny particles can inter the membranes of microorganisms. Atmospheric-pressure plasma jet system has sufficient power to sterilize and kill the bacteria, also is an important tool to employ in the medical field.

#### Introduction

The atmospheric-pressure plasma jet technique is described, wherever the plasma generated at the electrolyte media (gas and solution interface) as the electrode (cathode) for the preparation of different nanostructure materials or using directly to exposure on surfaces contaminated with virus/bacteria. Much attention has been attentive on discovering the effects of several parameters like the kind of system electrolyte [1,2]. The plasma jet system has huge importance from the organization of plasma because of its features of small physical size, generation [3-4], the stability of atmospheric-pressure [5], and non-equilibrium thermodynamics [6-7]. This property makes atmospheric-pressure plasma jet a good choice for many applications, such as medical treatment, surface modification, and nano-fabrication [8]. The characterization of plasma gives the unlimited potential to study the field of biomedical. plasma jet or needle is skillful of diseases (bacteria and virus) decontamination and removal cell without affecting necrosis to treat cells [9]. Furthermore, it has a modest design. A high-voltage electrode (cathode) usually make from a needle syringe and a metal pin. The discharge gas flows over the pin at a different flow rate and uses the controller to regulate the gas flow rate [10], the conditions for biomedical applications are that the needle should be near room temperature and conveys a low current. To date, applications such as cancer treatment sterilization, bleaching (dentistry), and healing of wound treatment have been demonstrated [11]. The plasma system is used in many applications such as industrial, biomedical, and environmental effectiveness, it is essential to know the parameters of plasma-like electron temperature and density of electron. To measure these parameters at lowpressure plasma, Langmuir probe measurement is used [12].

The hospital-acquired infections or called Nosocomial infections (NI), are developed through hospital care is not existing at entry fees but appearing after discharge [13].

The genus of Pseudomonas is the best common (gram-negative) bacteria involved in hospital-infections causing opportunistic infection in humans, particularly among immunodeficiency patients [14]; [15]. The explanations to determine most infections nosocomial when the PAeruginosa rarely attacks healthy tissues, it may infect virtually whole tissues in the body. [16]; [17]. This microorganism produces some of the enzymes which are associated with the pathogenesis of P. Aeruginosa infections. Despite developments in antibiotic treatment, P. Aeruginosa is fundamentally resistant to a number of that antibiotic [18]. Cold plasma can help as an alternative to other conventional decontamination methods such as heat, chemical, and irradiation sterilization methods, especially for sterilize heat-sensitive tools. It promotes an effective killing of the microbes and reduces the degree of destruction of the materials. The photons of UV and reactive species such as atoms and radicals play a major role in the cold plasma decontamination. Cold plasma can inactivate microorganisms and cell wall rupture and destroy biomolecules, such as DNA and proteins [19]. Therefore, plasma proved an effective "bactericidal" agent a "decontamination" technology to address the contamination of surgical instruments [20].

#### **Preparation of Nanoparticles (Copper Oxide)**

The nanoparticles of Copper oxide CuO have been synthesized by atmospheric-pressure plasma jet. The experimental system of the schematic diagram is shown in Figure 1. [21]. The copper oxide was prepared with and without adding CuCl2 into the electrolyte medium, as shown in Figure 2 [21]. Many crystal planes have been observed in Figure 2a. It was referred into polycrystalline, and containing four peaks belong to copper oxide nanostructures was observed via (ICDD, USA (1979) JCPDS 1979), C 29-1133. Also, the addition of CuCl2 powder on the compositions and distilled water led to an increase in the appearance of peaks.

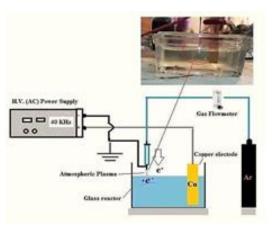


Figure 1 The atmospheric-pressure plasma jet system uses to synthesis of cooper oxide nanoparticles.

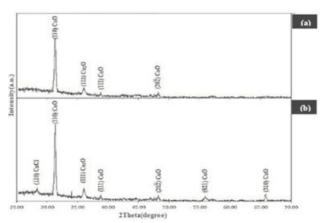


Figure 2 The x-ray diffraction patterns of the copper oxide nanoparticles were synthesized via atmospheric-pressure plasma jet system at different arrangements: (a) without CuCl2 (b) with CuCl2

It was shown that the copper oxide nanostructure prepared because of the existence of Cu with Cl2 and contributing to structure into the electrolyte system, see Figure 2b. This difference may have observed from change the color powder, see Figure 3 [21].

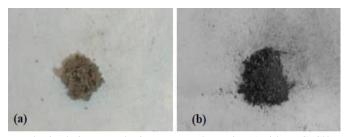


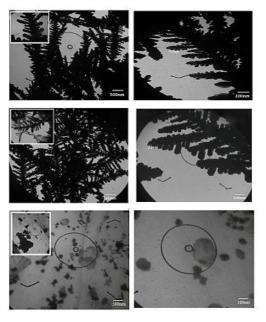
Figure 3 The photographs of powders synthesized via atmospheric-pressure plasma jet (a)without CuCl2 and (b) with CuCl2.

Copper oxide nanoparticles have extensive applications like adsorption of organic pollutants and solar cells. The outcome can be considered high and the work can be a good attempt to prepare copper oxide via this technique as a new preparation method to use it in important applications such as in biomedical.

#### **Fabrication of Nanostructured Silver Nanoparticles**

Silver nanoparticles have fascinated much attention because of their greater antibacterial property, it has a high fraction of surface atom [22]. All methods were informed to create Ag nanoparticles with required particle size, including physical, chemical, and biological approaches [23,24]. Silver nanoparticles were prepared by atmospheric plasma jet [25].

Figures 4a and 4b, show the TEM image of the Ag nanostructures prepared at 80 wt.% AgNO3 and 20 wt.% sucrose with preparation time 25min. As shown, approximately uniform shaped like (palm fronds) were grown and the minimum particle size was 20nm. While these shapes have been disappeared when the concentration becomes 60 wt.% AgNO3 and 40 wt.% sucrose at the same preparation time (25min), and then, it can be seen the Ag nanoparticles with minimum particle size was 10nm as shown in Figure (4c).



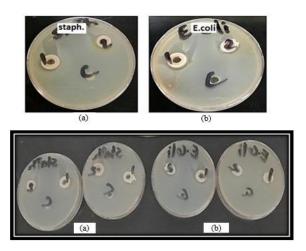


Figure 4 TEM images of Ag nanoparticles prepared at (a) at 80 wt% AgNO3 and 20 wt% sucrose with preparation time 10 min, (b) at 80 wt% AgNO3 and 20 wt% sucrose with preparation time 25 min, and(c) at 60 wt% AgNO3 and 40 wt% sucrose with preparation t

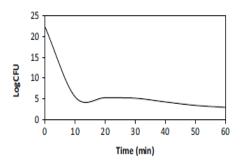
Figure 5 The disks show antimicrobial activity of Ag nanoparticles (a)Staphylococcus and (b) Escherichia coli

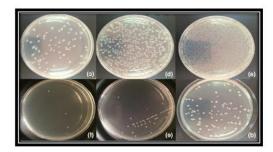
The two results were confirmed the sucrose prevented the aggregation, besides, the new features are dependent on the fractional composition of the prepared sample and preparation time. These results were helped to employ the Ag nanoparticles for killing and sterilizing bacteria and viruses. Figure 5 exhibits the antibacterial activity of silver nanoparticles. Its clear inhibition zone after twenty-four-hour incubation of the plate at 37 °C in temperature. The strains susceptible to silver nanoparticles show a superior inhibition zone, for two types of bacteria The inhibition zone for wholly samples with the mentioned micro-organisms was shortened in Table 1 [25].

Table 1 Inhibition zone of bacteria with Ag nanoparticles in mm

Sample No.	Staphylococcus	Escherichia coli
1	15 mm	16mm
2	17mm	15mm
3	19mm	14mm
4	16mm	17mm

Bacterial description of the bacteria (Pseudomonas Aeruginosa) has been carried out via microscopic, cultural, and biochemical tests [26]. Also, verification of the Bacterial identification tests was examined by using of API 20E kit [27]. The colony of P. Aeruginosa was cultured overnight 18 hours via inoculating a single insulated colony of bacteria in the nutrient broth, at 37 oC. Cells of bacteria were Precipitates by centrifuge at 8000g for 10 min; the supernatant was removed and the bacterial cell pellet was rinsed twice with sterile phosphate-buffered saline (PBS) and re-suspended in 10 ml of PBS [28]. Figures 6 and 7 indicate the outcomes from culturing the exposure P. Aeruginosa on a nutrient agar plate. Furthermost of the inactivation curves followed a biphasic pattern. Especially, a decline in populations usually looked after plasma exposure from early exposure time, shadowed via a decrease at the rate of inactivation after high exposure time.





**Figure 6** The decline curve of all isolates of bacteria (P. aeruginosa) signifying log CFU/ml as a function of exposure time of plasma

**Figure 7** The inactivation of P. aeruginosa culture after plasma exposure at different time (a) 10, (b) 20(c) 30 (d) 40 (e) 50 and (f) 60 min [28]

Genomic deoxyribonucleic acid has been taken out from P. Aeruginosa bacteria via Kit (Intron Biotechnology, Korea). A specific primer was used for gene amplification. Figures (8 and 9) indicated the amplified 16S rRNA fragment using a molecular size around 956 bp in length.

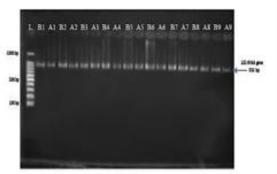


Figure 8 Electrophoresis Technique of P. aeruginosa, lane (L), DNA ladder, lanes (B1–B9): bacterial samples before plasma exposure, lanes (from A1 to A9): bacterial samples after Plasma exposure, [28].

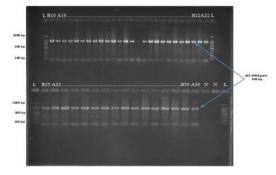


Figure 9 . Electrophoresis Technique of P. aeruginosa lane (L), (1500–100 bp DNA ladder), lanes (B10–B30): bacterial samples before plasma exposure, lanes (A10– A30): bacterial samples after plasma exposure lane (N): the negative control, [28].

#### **Conclusions**

Several recent developments prepared in the atmospheric-pressure plasma jet system has been discussed in this paper. These include the adjustment of this technique in many several applications. Together, these developments have transformed the capabilities of the plasma jet and helped to form it as the process of special for the production of imperative tools for decontaminating and sterilize the different places. The outcomes of some recent important studies in this review. Also been included the preparation of nanoparticles and it can be considered a good attempt to use in killing bacteria. Overall, hence, this paper provides a review of the current status of the atmospheric-pressure plasma jet process and considers future areas of exploitation for this technique.

#### References

- [1] Kolod. Radzimska, A. and Jesionowski, T. (2014) 'Zinc Oxide—From Synthesis to Application': A Review. Materials, 7, 2833-2881. https://doi.org/10.3390/ma7042833.
- [2] Klingshirn, C.F., Meyer, B.K., Waag, A., Hoffmann, A. and Geurts, J. (2010) 'Zinc Oxide: From Fundamental Properties towards Novel Applications'. Springer, New York. https://doi.org/10.1007/978-3-642-10577-7
- [3] El-Habachi, A. and Schoenbach, K.H. (1998) 'Generation of Intense Excimer Radiation from High-Pressure Hollow Cathode Discharges'. Applied Physics Letters, 73, 885. https://doi.org/10.1063/1.122027
- [4] Sankaran, R.M., Giapis, K.P., Moselhy, M. and Schoenbach, K.H. (2003) 'Argon Excimeremission from High-Pressure Microdischarges in Metal Capillaries'. Applied Physics Letters, 83, 4728.
- [5] Park, S.J. and Eden, J.G. (2002) 13-30 Micron Diameter Microdischarge Devices: Atomicion and Molecular Emission at above Atmospheric Pressures. Applied Physics Letters, 81, 4127. https://doi.org/10.1063/1.1520707
- [6] Kurunczia, P., Abramzona, N., Figusb, M. and Becker, K. (2004) Measurement of Rotational Temperatures in High-Pressure Microhollow Cathode (MHC) and Capillary Plasma Electrode (CPE) Discharges. Acta Physica Slovaca, 54, 115-124.
- [7] Penache, C., et al. (2002) Characterization of a High-Pressure Microdischarge Using Diode Laser Atomic Absorption Spectroscopy. Plasma Sources Science and Technology, 11, 476-483. https://doi.org/10.1088/0963-0252/11/4/314
- [8] Mariotti, D. and Sankaran, R.M. (2011) Perspectives on Atmospheric-Pressure Plasmas for Nanofabrication. Journal of Physics D: Applied Physics, 44, Article ID: 174023. https://doi.org/10.1088/0022-3727/44/17/174023
- [9] IE Kieft (2005) Plasma needle exploring biomedical applications of non-thermal plasmas, Thesis submitted of doctor and e Technische Universiteit Eindhoven.
- [10] Hong Y, Uhm H (2006) Microplasma jet at atmospheric pressure. Appl Phys Lett 89:221504.
- [11] Goree, J., Liu, B., Drake, D. & Stoffels, E. 2006. Killing of S. mutans bacteria using a plasma needle at atmospheric pressure. IEEE Transactions on Plasma Science 34(4): 1317-1324
- [12] Wu, S., Wang, Z., Huang, Q., Tan, X., Lu, X. & Ostrikov, K. 2013. Atmospheric-pressure plasma jets: Effect of gas flow, active species, and snake-like bullet propagation. Physics of Plasmas 20: 023503.
- [13] Pinhata, M. M. and Nascimento D. D. (2001). Neonatal nosocomial infections. Journal de Pediatria, 77: 81-96.
- [14] Tsakris, A.; Pournaras, S.; Woodford, N.; Palepou MF.; Babini GS.; Douboyas J. and Livermore DM. (2000). Outbreak of infections caused by Pseudomonas Aeruginosa producing VIM-1carbapenemase in Greece. J.Clin. Microbiol. 38: 1290-1292.
- [15] Riou M.; Carbonnelle S.; Avrain L.; Mesaros N.; Pirnay JP.; BilocqF.; De Vos D.; Simon A.; Piérard D.; Jacobs F.; Dediste A.; Tulkens PM.; Van Bambeke F. and Glupczynski Y. (2010). In vivo development of antimicrobial resistance in Pseudomonas Aeruginosa strains isolated from the lower respiratory tract of intensive care unit patients with nosocomial pneumonia and receiving antipseudomonal therapy. Int J Antimicrob Agents. 36(6):513-22.
- [16] Jeffery, B. Lyczak; Carolyn, L. Cannon and Gerald B. P. (2000). Establishment of Pseudomonas Aeruginosa infection. Lessons from a versatile opportunist, vol (2): 1051-1060.
- [17] Yvonne, A.; Hang, L.; and Siri, J.(2006). AMP-activation protein kinase protects against anti-epidermal growth factor receptor Pseudomonas exotoxin A immunotoxin induced MA11 breast cancer cell death. Mol. Cancer Ther., 5:1050-1059.

- [18] Ana Lúcia Peixoto and Freitasand Afonso Luis Barth (2002). Antibiotic resistance and molecular typing of Pseudomonas Aeruginosa: Focus on Imipenem. The Brazilian Journal of Infectious Diseases. 6(1):17.
- [19] Sharma, A.; Pruden, A.; Yu, Z.; Collins, G. J.(2005). Bacterial inactivation in open air by the afterglow plume emitted from a grounded hollow slot electrode. Environ. Sci. Technol., 39, 339–344.
- [20] Felipe Iza, G.J. Kim; S.M. Lee; Jae Koo Lee; James L. Walsh, Yuan Tao Zhang and Michael G. Kong. (2008). Microplasmas: Sources, Particle Kinetics, and Biomedical Applications. Plasma Processes and Polymers, 322-344.
- [21] Ahmed A Anber et al. (2018). "Preparation of Nanoparticles Copper Oxide using an Atmospheric- Pressure Plasma Jet", J. Phys.: Conf. Ser. 1032 012009.
- [22] C.A.D.Santos, A.F. Jozala, A.P.Jr and M.M.Seckler. (2012). Journal of Nanobiotechnology. 10,43.
- [23] Y.T.Zhang, Y.Guo, M.A.T.Cai. (2011). Chin.Phys.Lett. 28, 11.
- [24] M.B.Ahmad, M.Y.Tay, K.Shameli, M.Z.Husssein and J.J. Lim. Int. J. Mol. Sci.12,(2011).
- [25] Ahmed A Anber et al Fabrication of Nanostructured silver liquid by Atmospheric-Pressure Plasma Jet for Bacteriological Applications, 2018 Bionanoscience journal.
- [26] Benson, H.J. (2002). Microbiological Applications Laboratory manual in General Microbiology. 8t h ed. McGraw-Hi 11. New York.
- [27] Tankeshwar, A. (2015). API 20E Test System: Introduction, Procedure Results and Interpretations. Microbeonline.
- [28] Rana Kadhim Mohammed & Hiba Nabil Abbas (2018). "Bactericidal Effect of Needle Plasma System on Pseudomonas Aeruginosa", Iran J Sci Technol Trans Sci .



# Iraqi Journal of Nanotechnology synthesis and application



Journal Homepage: https://publications.srp-center.iq/index.php/ijn

# Effect of Silver Doping on Structural and Photocatalytic Circumstances of Zno Nanoparticles

#### Eitemad S. Fadhil<sup>1</sup>, Luma M. Ahmed <sup>1\*</sup> and Ayad F. Mohammed<sup>2</sup>

- 1- Chemistry Department, College of Science, University of Kerbala, Kerbala, Iraq,
- 2- Department of Chemistry, College of Women Science, University of Babylon, Hilla, Iraq
- \*Corresponding author: <a href="mailto:luma.ahmed@uokerbala.edu.iq">luma.ahmed@uokerbala.edu.iq</a>.

#### **Keywords:**

Ag doped Zinc oxide; Undoped Zinc oxide; Photocatalytic decolourization; Methyl green dye; Treatment of wastewater.

#### Abstract

This article describes the synthesis of ZnO nanoparticles (Nps) using the coprecipitation method and then calcinated at 500oC for 2 h. The photo activity of ZnO nanoparticles was examined in photo decolorization of methyl green dye under artificial UV-A light. This prepared photocatalyst (ZnO Np) was modified his surface by 2% Ag doped using the photo deposition method under inert gas for 3h. The characterization of undoped and 2% Ag doped ZnO Nps were estimated by Fourier-transform infrared spectroscopy (FT-IR), X-ray Diffraction (XRD), and Atomic force microscopy (AFM). In FT-IR analysis, the new peaks occurred around 624-778 cm-1 confirmed the Ag really is doped on prepared ZnO Np. Based on data from XRD, the mean crystal size was reduced with doped the 2% Ag. The AFM images for the prepared photocatalysts ensure that the shapes of all samples are semi-spherical with nanometer size. Series of kinetics experiments were performed for the photocatalytic decolourization of methyl green dye using undoped and 2% Ag doped ZnO nanoparticle and found to be pseudo-first-order kinetics.

#### Introduction

Zinc oxide (ZnO) is one of the important inorganic amphoteric oxides, with pHZPC of approximately 9.0[1, 2], and a boundary between an ionic material and a semiconductor [3, 4]. This oxide is deemed an n-type metal oxide semiconductor, operated at near-ultraviolet and visible spectra regions with direct band gap 3.436 eV at 0 K and (3.37±0.01) eV) at room temperature [5-7]. ZnO is also known as a II-VI semiconductor, which has various forms beyond to lie of zinc atom and the oxygen atom in the 2nd and 6th groups of the periodic table [8] such as cubic zincblende, cubic rock salt, and hexagonal wurtzite [7]. On the other hand, it has been prepared as a nanomaterial in different dimensions such as one dimensional (1D), two dimensional (2D), and three dimensional (3D) structures over the past few years, there are varying procedures for preparing them as physical methods (such as Laser ablation and Chemical vapor deposition(CVD)), chemical methods (such as Precipitation, sol-gel and hydrothermal), and bio methods (such as a green method in employing the extractions of plants and Microbes mediated like bacteria, viruses, and fungi) [9-15]. ZnO bulk or nanomaterial is used in various fields, so, they employed as a photocatalyst to degrade the organic compounds in water [16,17], protection of skin from solar irradiation[18, 19], used in the manufacture of active solar cell [20-22], employed as gas, chemical and biological sensor[23,24], employed in manufactured of cosmetic creams[25]. This research focused on synthesized of ZnO nanoparticles by co-precipitation method, and then changed its surface with doped 2 % of Ag under purged N2, in order to reduce the recombination process using the photo deposition; under illumination with UV-A light (HPML-400 watt), which have a light intensity equal to 6 x 10-5 Enstine s-1, that measured by using the chemical actinometry [26].

The employing of FT-IR, XRD, and AFM is used to investigate the properties of these prepared photocatalysts. The efficiency of decolourization of methyl green dye was achieved under the optimum conditions. A reasonable mechanism for dye decolorizing was suggested.

#### **Experimental Work**

#### Chemicals

The used chemicals were employed without any treatment in this work. Zinc sulfate heptahydrate (ZnSO4.7H2O), Sodium hydroxide (NaOH), Absolute ethanol were supplied by BDH -UK. Methyl green dye (C27H35 Cl2N3.ZnCl2) was purchased from GEORGE T. GURRL TD –UK and Silver nitrate (AgNO3) was Purchased from AppliChem GmbH-Germany. The chemical structure of Methyl green dye is depicted in Figure 1.

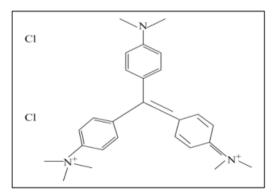


Figure 1. The chemical structure of Methyl green dye.

#### Synthesis of ZnO nanoparticles

The ZnO-NPs were prepared directly by the co-precipitation method from two aqueous solutions NaOH and ZnSO4.7H2O with molar ratio (4:1) [27, 28]. The precursor solution was prepared by completely dissolving (ZnSO4.7H2O) in distilled water. The precipitation agent was also prepared from dissolved NaOH in distilled water. 100 mL of NaOH solution added slowly as drop by drop to the precursor solution with vigorous stirring for 20 min at 25 °C. A solution with pH=7 containing a white precipitate can be observed as shown in Figure 2.



Figure 2 Real images for preparing ZnO in the co-precipitation method.

Then the white precipitate was collected, filtered, washed several times with distilled water, and then with absolute ethanol to ensure removal of all remaining sulfate particles. The white wet precipitate was dried in an oven at 86 °C and then kept overnight in a desiccator. The resulting powder was calcined at 500°C for 2h. The preparation of ZnO-Nps can be explained by the following equations,

$$ZnSO_4.7H_2O + NaOH \rightarrow Zn(OH)_2 + Na_2SO_4 + 7H_2O$$
 (1)

$$Zn(OH)_2 + 2H_2O \rightarrow [Zn(OH)_4]^{2-} + 2H \rightarrow 3H_2O + ZnO$$
 (2)

#### Synthesis of Ag doped ZnO nanoparticles

After calcined, the modification of the ZnO NPs surface is necessary to depress the recombination by 2% Ag doped using the photo deposition method: under purged N2 [29]. In a closed Pyrex photoreactor, exactly 2 g of ZnO NPs was dispersed in 20 mL from absolute ethanol and then mixed with suitable volume from the stock solution (1% Ag NO3) under purged nitrogen gas. This solution was illuminated with UV-A light for 3h. The leaden color precipitates were formed; as shown in figure 3. This leaden precipitant was filtered; washed using absolute ethanol and dried at 80 oC in an oven. The photo deposition mechanism [29,30] was used, which is basically based on the use of Philips High-Pressure Mercury Lamp (HPML) 400 watt as a UV-A light and the ZnO's photoelectron to conduct Ag+ to Ag metal photoreduction on its surface.

$$ZnO + hv \rightarrow e_{CB}^{-} + h_{VB}^{+}$$
 (3)  
 $Ag^{+} + ZnO e_{CB}^{-} \rightarrow Ag^{0}/ZnO$  (4)

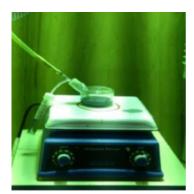


Figure 3. Real image for doped 2% from Ag on ZnO Np surface in the photo deposition method.

#### Characteristics of synthesis samples

Series of techniques were used to conduct this work, such as Atomic absorption (AA-6300-Shimadzu) analysis, which applied to estimate if all amount of Ag was doped. FTIR model 8400S -Shimadzu employed the KBr disc in the ranged of 400 - 4000 cm-1. XRD analysis style Lab X XRD 6000-Shimadzu was used to investigate whether the samples were successfully prepared and then measure the mean crystal sizes for all prepared samples by using the Scherrer's formula [31-33] with use  $2\theta$  ranging from 200 to 800. Moreover, the AFM model, AA 3000 was employed to represent the shape of the samples prepared.

#### Photoreaction of methyl green dye with synthesis photocatalysts

In order to check the efficiency of prepared photocatalysts, the undoped ZnO Np and 2 % Ag doped ZnO NPs were applied to the solution of methyl green dye. Series of preliminary experiments were performed with employed the ZnO nanoparticles (NP) in dye aqueous solution. The undoped or 2 % Ag doped ZnO NPs were dispersed in 200 mL of 25 ppm of methyl green dye solution.

At outset, the dark reaction is a vital step to reach for the homogenous equilibrium at 30 min, the adoption on the ZnO surface has happened as physical adsorption [34, 35]. Under moderate stirring, the UV-A light was focused on the produced suspension solution. In intervals, time of illuminated; 2.5 mL of samples were collected and twice separated using a centrifuge to remove all the fine catalyst particles.

In photoreaction, the residue concentration of this dye was monitored at 630 nm using UV-Vis analysis. From based on equations 5 and 6 [36-38], the apparent rate constant (kapp.) and the photo decolourization efficiency % (PDE %) were determined.

$$\ln\left(\frac{C_o}{C_t}\right) = k_{app} t \tag{5}$$

$$PDE\% = \left(\frac{C_o - C_t}{C_o}\right) x100 \tag{6}$$

Where:  $C_0$  and  $C_t$  are the concentration of methyl green dye without and with irradiation respectively.

#### **Results and Discussion**

#### Atomic absorption analysis

The result of this analysis was indicated that the concentration of Ag that needed to doped as 2% Ag is equal to 1723.336 ppm, but the residue of Ag in solution after irradiation the colloid solution of ZnO for 3h was reached 0.36 ppm, that ensure the 2 % Ag was doped successfully on ZnO surface.

#### FTIR analysis

Based on the FT-IR spectra for undoped and 2% Ag doped on ZnO-NP surface was investigated as shown in figures 4 (a) and (b). The essential peaks of ZnO are obtained at around  $3446\text{-}3450~\text{cm}^{-1}$  for stretching vibrations of O-H and appearance two peaks approximately at 1120 and 1577 cm<sup>-1</sup>. On the other hand, the narrowband around  $410 - 500~\text{cm}^{-1}$  are assigned to the stretching vibration band of Zn-O [28,39]. Moreover, the new peaks occur in the region  $\sim 624\text{-}778~\text{cm}^{-1}$ , when Ag doped on ZnO NP, this result is approximately agreed with T. S. Vijayakumar et al [40].

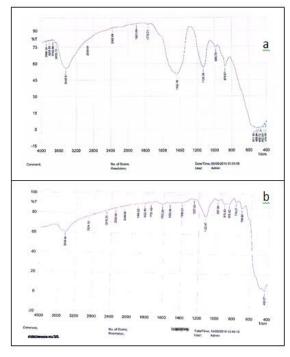


Figure 4. FT-IR Spectra for prepared a) undoped ZnO NP and b) 2% Ag doped ZnO NP

#### XRD analysis

Based on the indexed [JCPDS no. 36-1451] and [JCPDS card no. 04-0783] of the ZnO hexagonal wurtzite structure and the face-centered cubic structure of Ag [41], the XRD peaks in figure 5 were indicated the undoped and Ag doped ZnO Np samples are successfully formed. The XRD spectra were evidenced that the nine broad bands at  $2\theta$  values  $31.6^{\circ}$ ,  $34.4^{\circ}$ ,  $36.15^{\circ}$ ,  $47.45^{\circ}$ ,  $56.5^{\circ}$ ,  $62.7^{\circ}$ ,  $66.4^{\circ}$ ,  $67.8^{\circ}$ , and  $69^{\circ}$  are beyond the miller indexes equal to (100), (002), (101), (102), (110), (103), (200), (112) and (201) respectively [28, 42]. Moreover, a new broad peak has confirmed the Ag doped on ZnO NP surface, and noticed at  $44.50^{\circ}$  with miller index (200); this result did not form a silver oxide.

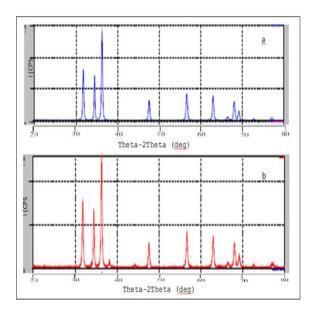


Figure 5 The XRD Spectra of a)Undoped ZnO Np, b) 2 % Ag doped ZnO Np.

Using the Scherer equation [31,43], the highest three peaks at  $2\theta$  31.6°, 34.4°, 36.15° were selected to calculate the mean crystallite size of ZnO NPs. The magnitudes of mean crystallite size of undoped and 2% Ag doped ZnO NP were proved the Ag doped ZnO NPs is less value than it's for ZnO NP that due to incorporate of Ag(I) (with ionic radius 0.115 Å) with Zn(II) (with ionic radius 0.74 Å) in ZnO lattice [44]; these values were displayed in table 1.

Table 1. The Mean Crystallite Sizes of Undoped ZnO and 2% Ag doped ZnO NP.

Mean Crystallite sizes /nm	Crystal components
29.0090	(0)% Ag doped ZnO NP
28.2010	(2)% Ag doped ZnO NP

#### **AFM** analysis

Figures 6 and 7 display, that the undoped and 2% Ag doped ZnO Nps are semi-spherical and nanoparticles. The particle size of prepared ZnO Np increased with 2% Ag doped on ZnO Np from 7.28 nm to 22.6 nm, which leads to improvement in the agglomerated process when metal-doped [45,46].

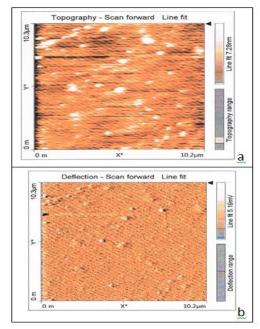


Figure 6 . AFM images for a)2- Dimensions Image (Topography) and b) 2- Dimensions Image(Deflection) of Udoped ZnO Np.

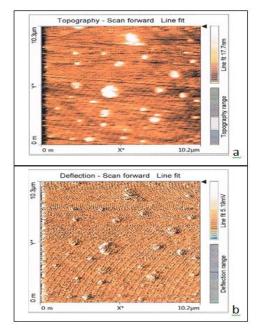


Figure 7 . AFM images for a) 2- Dimensions Image (Topography) and b) 2- Dimensions Image(Deflection) of 2% Ag doped ZnO NP.

#### Photocatalytic activity reaction of undoped and Ag doped on ZnO NPs

Figures 8 (a,b) illustrates, that the Ag doped ZnO Np indicates to increase the photoreaction with increment the apparent rate constant and PDE% values. Since Ag acts as a sink of electrons, so, the recombination process will reduce [41,47, 48]. The best PDE% with using ZnO Np increases from 37.000 % to 87.368 % with 2% Ag doped on ZnO NP for 40 min at 25 ppm dye, 0.7g. /200 mL catalyst, pH 5.4, and 298.15 K.

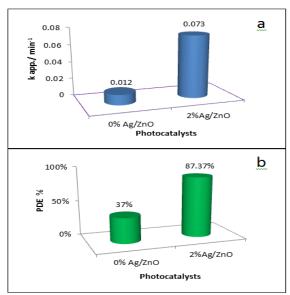
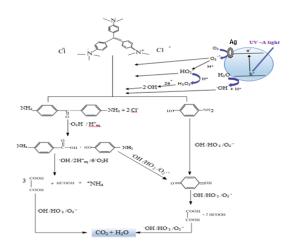


Figure 8. The relation between a) Kapp verse photocatalysts, b) PDE % verse photocatalysts.

#### Suggested mechanism

According to scheme 1, the more acceptance mechanism for photo decolourization of methyl green dye was suggested to use the undoped ZnO NP or Ag 2% ZnO NP. This mechanism was based on a series of redox processes [49-51], which leading in essential to produce a hydroxyl free radical as a key to starting the photo decolourization of this photoreaction[52-56].



Scheme 1. The schematic diagram for decolourization mechanism in (methyl green Dye/undoped or Ag 2% ZnO NP/ UV-A light) system.

#### **Conclusions**

The main conclusions in this work can be summarized by the undoped ZnO NP and 2% Ag doped ZnO NP, respectively, which were successfully prepared by using co-precipitation and photodeposition. That was evidenced by FT-IR, XRD, and AFM. The mean crystal size at Ag 2% doped on ZnO Np was found to be reduced compared without doping. All prepared photocatalysts have been shown in the AFM images as semispherical. The FT-IR spectra were conformed to ZnO NP and Ag-Zn bond form. At working conditions, the photocatalytic decolourization of methyl green dye using prepared samples was performed and obeyed to pseudo-first-order. with 2% Ag doped on ZnO Np surface, the PDE % was found to be increased.

#### Acknowledgment

The authors would like to recognize anyone at the University of Kerbala and the University of Babylon, College of Science in the Department of Chemistry and, College of Women Science in the Department of Chemistry in Iraq respectively, who supports this project in practical components.

#### References

- [1] Pera-Titus, M., Garc´ıa-Molina, V., Baños, M., Giméneza, J. and Espluga, S., Decolourization of Chlorophenols by Means of Advanced Oxidation Processes: A General Review, Applied Catalysis B: Environmental, 2004, vol. 47, 219-256.
- [2] Crosby, D. G., Environmental Toxicology and Chemistry, Oxford University Press, New York, 1998.
- [3] Ashrafi A., and Jagadish, C., Review of zincblende ZnO: Stability of metastable ZnO phases, Journal of Applied Physics, 2007, vol.102, 071101-1 071101-12.
- [4] Lu, Y. and Zhong, J., Zinc Oxide-Based Nanostructures—CH6", Semiconductor Nanostructures for Optoelectronic Applications, Editing by T. Steiner, Artech House, Inc., Boston, 2004.
- [5] Hull, R., Jagadish, C., Osgood, R. M., Parisi, Jr. J., Wang, Z., and Warlimont, H., Zinc Oxide From Fundamental Properties Towards Novel Applications, Springer-Verlag Berlin Heidelberg, 2010.
- [6] Janotti A., and Van de Walle, C. G, Fundamentals of zinc oxide as a semi-conductor, Rep. Prog. Phys., 2009, vol. 72, 126501, 1-29.
- [7] Klingshirn, C. F., Meyer, B. K., Waag, A., Hoffmann, A. and Geurts, J., Zinc Oxide-From Fundamental Properties Towards Novel Applications, 1st edition, Springer, Heidelberg, 2010.
- [8] Onodera, A., and Takesada, M., Electronic Ferroelectricity in II-VI Semiconductor ZnO, CH 11, Advances in Ferroelectrics, A. Peláiz-Barranco (Ed.), InTech, DOI: 10.5772/52304,2012.

- [9] Ul Haq, A. N., Nadhman ,A., Ullah, I., Mustafa, G., Yasinzai, M., and Khan, I., Synthesis Approaches of Zinc Oxide Nanoparticles: The Dilemma of Ecotoxicity, Journal of Nanomaterials, 2017, 1-14
- [10] Sabir, S., Arshad, M., and Chaudhari, S. K., Zinc Oxide Nanoparticles for Revolutionizing Agriculture: Synthesis and Applications, The Scientific World Journal, 2014, 1-8.
- [11] Kołodziejczak-Radzimska, A. and Jesionowski, T., Zinc Oxide-From Synthesis to Application: A Review, Materials, 2014, vol. 7, 2833-2881.
- [12] Brintha, S.R., Ajitha, M., Synthesis and characterization of ZnO nanoparticles via aqueous solution, sol-gel and hydrothermal methods, IOSR Journal of Applied Chemistry (IOSR-JAC), 2015, vol. 8, no. 11, 66-72.
- [13] Janice Low, J. N., Wong, W. Y., Rashmi, W., Kadhum, A. A. H and Mohamad, A. B., Synthesis of Zinc Oxide Nanoparticles Using Liquid-Phase Laser Ablation and Its Antibacterial Activity, Journal of Engineering Science And Technology, 6th Eureca 2016 Special Issue May 2017, 2017, 29 42.
- [14] Djenadic, R., and Winterer, M., Chemical Vapor Synthesis of Nanocrystalline Oxides, CH2, Nanoparticles from the Gasphase Formation, Structure, Properties, A. Lorke, M. Winterer, R. Schmechel, C. Schulz, (Eds.), 1st edition, Springer, 2012.
- [15] Meruvu, H., Vangalapati, M., Chippada, S. C., And Bammidi, S. R., Synthesis And Characterization of Zinc Oxide Nanoparticles and Its Antimicrobial Activity Against Bacillus Subtilis and Escherichia Coli, Rasayan Journal of Chemistry, 2011, vol.4, No.1, 217-222.
- [16] Abbas, S. K., Hassan Z. M., and L. M. Ahmed, Influencing the Artificial UV-A light on decolorization of Chlorazol black BH Dye via using bulk ZnO Suspensions, IOP Conf. Series: Journal of Physics: Conf. Series, 2019, vol. 1294, 1-8.
- [17] Kzar, K. O., Mohammed, Z. F., Saeed, S. I., Ahmed, L. M., Kareem, D. I., Hadyi, H. and Kadhim, A. J., Heterogeneous photo-decolourization of cobaltous phthalocyaninate dye (reactive green dye) catalyzedby ZnO, AIP Conference Proceedings, 2019, vol. 2144, 020004-1 020004-10.
- [18] Tsuzuki, T., and Wang, X., Nanoparticle Coatings for UV Protective Textiles, RJTA, 2010, vol. 14, no. 2, 9-20.
- [19] Klimová, Z., Hojerová, J. and Pažoureková, S., Current problems in the use of organic UV fi lters to protect skin from excessive sun exposure, Acta Chimica Slovaca, 2013, vol. 6, no. 1, 82-88.
- [20] Yu, X., Wang, D., Lei, D., Li, G. and Yang, D., Efficiency improvement of silicon solar cells enabled by ZnO nanowhisker array coating, Nanoscale Research Letters, 2012, vol.7, no. 306, 1-5.
- [21] Han, J., Fan, F., Xu, C., Lin, S., Wei, M., Duan, X., and Wang, Z. L., ZnO nanotube-based dye-sensitized solar cell and its application in self-powered devices, Nanotechnology, 2010, vol. 21,1-7, 2010.
- [22] Apostolopoulou, A., Karageorgopoulos, D., Rapsomanikis, A. and Stathatos, E., Dye-Sensitized Solar Cells with Zinc Oxide Nanostructured Films Made with Amine Oligomers as Organic Templates and Gel Electrolytes, Journal of Clean Energy Technologies, 2016, vol. 4, no. 5, 311-315.
- [23] Leonardi, S. G., Two-Dimensional Zinc Oxide Nanostructures for Gas Sensor Applications, Chemosensors, 2017, vol. 5, no. 17, 1-28.
- [24] Marie, M., Mandal S., and Manasreh, O., An Electrochemical Glucose Sensor Based on Zinc Oxide Nanorods, Sensors, 2015, vol. 15, 18714-18723.
- [25] Spoialaa, A., Albub, M. G., Ficaia, A., Andronescua, E., Voicua, G., and Ungureanu, C., THE SiO2/ZnO Composite Materials for Cosmetic Creams, Digest Journal of Nanomaterials and Biostructures, 2014, vol. 9, no. 4, 1729 1737.

- [26] Ahmed, S., Photo electrochemical study of ferrioxalateactinometry at A glassy carbon electrode, Journal of Photochemistry and Photobiology A: Chemistry, 2004, vol.161, 151-154.
- [27] Ahmed, M. T., Abd-Elhamid, M. I., Sarhan, A., Hassan, A., Preparation and Characterization of ZnO Nanoparticles by Simple Precipitation Method, International Journal of Science, Engineering and Technology, 2016,vol. 4, no. 3, 507-512.
- [28] Behnajady, M. A., Modirshahla N., and Ghazalian, E., Synthesis of ZnO Nanoparticles at Different Conditions: A Comparison of Photocatalytic Activity, Digest Journal of Nanomaterials and Biostructures, 2011,vol. 6, no.1, pp. 467-474.
- [29] Nghia, N. V., Trung, T. N., Truong, N. N. K. and Thuy, D. M., Preparation and Characterization of Silver Doped ZnO Nanostructures, Open Journal of Synthesis Theory and Applications, 2012, vol. 1, 18-22.
- [30] Ahmed, L. M. and Hussein, F.H., Roles of Photocatalytic Reactions of Platinized TiO2 Nanoparticales, LAP Lambert Academia Published, Germany, 2014.
- [31] Patterson, A., The Scherrer Formula for X-Ray Particle Size Determination, Physical Review, 1939, vol. 56, 978-982.
- [32] Jawad, T. M. and Ahmed, L. M., Direct Ultrasonic Synthesis of WO3/TiO2 Nanocomposites and Applying them in the Photodecolorization of Eosin Yellow Dye, Periódico Tchê Química., 2020, vol.17, no.34, 621-633.
- [33] Hayawi, M. K., Kareem, M. M. and Ahmed, L. M., Synthesis of Spinel Mn3O4 and Spinel Mn3O4/ZrO2 Nanocomposites and Using Them in Photo-Catalytic Decolorization of Fe(II)-(4,5-Diazafluoren-9-One 11) Complex, Periódico Tchê Química, 2020, vol.17, no. 34, 689-699.
- [34] Alattar, R. A., Saleh, H. M., AL-Hilfi, J.A., Ahmed, L. M., Influence the addition of Fe2+ and H2O2 on removal and decolorization of textile dye (dispersive yellow 42 dye), Egypt. J. Chem., DOI: 10.21608/EJCHEM.2020.23542.2400 (In press).
- [35] Karam, F. F, Noor Saeed, H.M., Al Yasasri, A. H., Ahmed, L. M., Saleh, H., Kinetic Study for Reduced the Toxicity of Textile Dyes (Reactive yellow 14 dye and Reactive green dye) Using UV-A light/ZnO System, Egyptian Journal of Chemistry, 2020, vo. 63,no. 8, 211-223.
- [36] Ahmed, L. M., Saeed, S. I., and Marhoon, A. A., Effect of oxidation agents on photo-decolorization of Vitamin B12 in the presence of ZnO/UV-A system, Indones. J. Chem., 2018, no.2, 272 278.
- [37] Marhoon, A. A., Saeed, S. I., and Ahmed, L. M., Application of some effects on the Degradation of the aqueous solution of Fuchsine dye by photolysis, Journal of Global Pharma Technology, 2019, vol. 11, no.9, 76-81.
- [38] Abass, S. K., Al-Hilfi,, J. A., Abbas, S. K., and Ahmed, L. M., Preparation, Characterization and Study of the Photodecolorization of Mixed-Ligand Binuclear Co(II) Complex of Schiff Base by ZnO, Indones. J. Chem., 2020, vol. 20, no. 2, 404 412.
- [39] Kleinwechter, H., Janzen, C., Knipping, J., Wiggers, H., Roth, P., Formation and properties of ZnO nanoparticles from gas phase synthesis processes, J. Mater. Sci., 2002, vol. 37, 4349-4360.
- [40] Vijayakumar, T. S., Karthikeyeni, S., Vasanth, S., Ganesh, A., Bupesh, G., Ramesh, R., Manimegalai, M., and Subramanian, P., Synthesis of Silver-Doped Zinc Oxide Nanocomposite by Pulse Mode Ultrasonication and Its Characterization Studies, 2013,1-7.
- [41] Kuriakose, S., Choudhary, V., Satpati, B., and Mohapatra, S., Enhanced photocatalytic activity of Ag–ZnO hybrid plasmonic nanostructures prepared by a facile wet chemical method, Beilstein J. Nanotechnol.,2014, vol. 5, 639–650.

- [42] Awad, A., Abou-Kandil, A. I., Elsabbagh, I., Elfass, M., Gaafar, M., and Mwafy, E., Nanoparticles synthesized via novel calcination method polymer nanocomposites part 1: structural characterization of zincoxide, journal of thermoplastic composite materials , 2014, 1-6.
- [43] Mohammed, B.A., and Ahmed, L.M., Improvement the photo-catalytic properties of ZnS nanoparticle with loaded manganese and chromium by co-precipitation method, JGPT, 2018, vol. 10, no. 7,129 –138.
- [44] Zeferino, R. S., Flores, M. B., and Pal, U., Photoluminescence and Raman Scattering in Ag-doped ZnO Nanoparticles, Journal of Applied Physics, 2011, vol. 109, 014308, 014308-1 014308-8.
- [45] Ahmed, L. M., Hussein, F. H. and Mahdi, A. A., Photocatalytic Dehydrogen-ation of Aqueous Methanol Solution by Naked and Platinized TiO2 Nanoparticles, Asian Journal of Chemistry, 2012, vol. 24, no. 12, 5564-5568.
- [46] Ahmed, L. M., Ivanova, I., Hussein, F. H. and Bahnemann, D. W., Role of Platinum Deposited on TiO2 in Photocatalytic Methanol Oxidation and Dehydrogenation Reactions, International Journal of Photoenergy, 2014, 1-9.
- [47] Montalti, M., Credi, A., Prodi, L. and Gandolfi, M. T., Handbook of Photo-chemistry, 3rd edition, Taylor &Francis Group, London,, CH12, 2006, 601-603.
- [48] Behnajady, M.A., Modirshahla, N., Shokr, M., and Rad, B., Enhancement of Photocatalytic Activity of TiO2 Nanoparticles by Silver Doping: Photodeposition Versus Liquid Impregnation Methods, Global Nest Journal, vol. 10, no. 1, pp. 1-7, 2008.
- [49] Hussein, Z. A., Abbas, S. K, and Ahmed, L. M., UV-A activated ZrO2 via photodecolorization of methyl green dye, IOP Conference Series: Materials Science and Engineering, 2018, vol. 454, 1-11.
- [50] Jasim, K. M., and Ahmed, L. M., TiO2 Nanoparticles Sensitized by Safranine O Dye using UV-A Light System, IOP Conference Series: Materials Science and Engineering, 2019, vol. 571, 1-9.
- [51] Fakhri, F. H., and Ahmed, L. M., Incorporation CdS with ZnS as nanocomposite and Using in PhotoDecolorization of Congo Red Dye, Indones. J. Chem., 2019, vol. 19, no. 4, 936 943.
- [52] Neppolian, B., Choi, H.C., Sakthivel, S., Arabindoo, B., and Murugesan, V., Solar light induced and TiO2 assisted degradation of textile dye reactive blue 4, Chemosphere, 2002, vol.46, 1173-1181.
- [53] Hussein, F., Photochemical Treatments of Textile Industries Wastewater, Advances in Treating Textile Effluent, Peter J. Hauser (Ed.), ISBN: 978-953-307-704-8, InTech, 2011.
- [54] Ahmed, L. M., Photo-Decolourization Kinetics of Acid Red 87 Dye in ZnO Suspension Under Different Types of UV-A Light, Asian J. Chem., 2018, vol.30, no. 9, 2134-2140.
- [55] Ahmed, L. M., Jassim, M. A., Mohammed, M. Q. and Hamza, D. T., Advanced Oxidation Processes for Carmoisine (E122) Dye in UVA/ZnO System: Influencing pH, Temperature and Oxidant Agents on Dye Solution, Journal of Global Pharma Technology, 2018, vol. 10, no. 7, 248-254.
- [56] Skriver H., Rosengaard N. Surface Energy and Work Function of Elemental Metals, The American Physical Phenomena, 1992, vol. 46, no. 11, pp. 7157-7168.



# Iraqi Journal of Nanotechnology synthesis and application



Journal Homepage: https://publications.srp-center.iq/index.php/ijn

# Synthesis and Characteristics of (PAV-PAVC-Ti) Nanocomposites

Waleed Khalid Kadhim<sup>1</sup>, Maha Khalid Alshmmari<sup>2</sup>, Maryam Adnan Al-Ethary<sup>3</sup>

- 1- Ministry of Education, Directorate of Educational Babylon, Hela, Iraq email: welidkalid37@gmail.com,
- 2- Ministry of Higher Education and scientific research, College of Engineering, Department of Biomedical Engineering, University of Karbala, Karbala, Iraq, email: <a href="mailto:maha.k@uokerbala.edu.iq">maha.k@uokerbala.edu.iq</a>.
- 3- Ministry of Education, Directorate of Educational Babylon, Hela, Iraq, email: <a href="mailto:mariem20132420@gmail.com">mariem20132420@gmail.com</a>

#### **Keywords:**

### Nanocomposite; Fourier Transform Infrared Spectroscopy (FTIR); Scanning Electron Microscope (SEM); Poly (vinyl alcohol); Poly (vinyl acetate); Titanium Nanoparticles;

#### **Abstract**

PVA-PVAC-Ti nanocomposites have been prepared by using the 'casting method' with different weight percentages of titanium nanoparticles. The (PVA-PVAC-Ti) nanocomposites have been diagnosed by different routes such as the 'Fourier Transform Infrared Spectroscopy (FTIR)', 'scanning electron microscope (SEM)' images, and optical microscope images. The experimental results (FTIR) showed increasing the value of the absorbance of the (PVA-PVAC-Ti) nanocomposites with an increase in the proportion of titanium nanoparticles. All peak characteristics remain the same and the most bond in the same wavenumber. The morphology of the (PVA-PVAC-Ti) nanocomposites films has been studied using (SEM) technique, which showed grain distribution at surface morphology and grain aggregates with increasing of titanium nanoparticles. Photos optical microscope shows the distribution of titanium nanoparticles atoms for all nanocomposite's films, it also shows a continuous network of ions inside the polymers in a ratio (16 wt.%) of (Ti. nanoparticles).

#### Introduction

In recent days, Nanomaterials based on polymers are viewed as multi-use materials, including scientific applications and part of technological advances, this is due to the incorporation of nanoparticles into polymer synthesis that affects extensively the surface morphology, and visual qualities [1], While preserving the original characteristics. A new way to improve the performance of materials in many applications such as biomedical, medical, coating materials, optical devices, and biological sensors [2].

Nanocomposites can be defined as are substances that appear at least one dimension in the nanometer range", and the size of the addition to the nano-miter, and the interactions become highly significant and result in significant changes in the properties of the final material. The nanocomposite consists of two parts, "filler and matrix", a traditional material in addition to padding is a nanomaterial [3,4]. Polymers are made up of large parts as a result of the replication of small building units associated with the polymerization process [5]. Polyvinyl alcohol is commonly written (PVA) by polymers which are very well known, used in many applications and quite common ones are semiconductors. PVA is a water-soluble polymer used widely in adhesives, paints, sealants, coatings, textiles, plastics... etc. Visible light transmittance is extremely high, and polymers have been used in the manufacture of optical devices because they contain distinct natural properties. [6], Such as high flexibility, ease of operation and mechanical strength are acceptable etc. are particularly useful in technical applications as in Table 1 [7]. Produced commercially at the hydrolysis of polyvinyl acetate (PVAC) as in Figure (1).

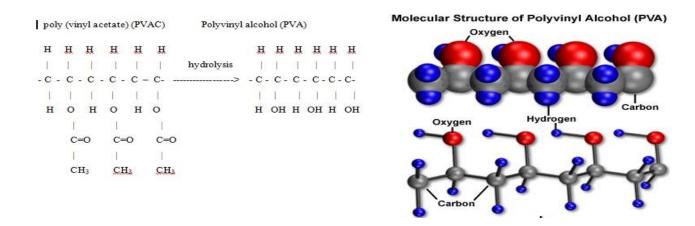


Figure 1 Preparation and molecular structure of polyvinyl alcohol

Table 1 Physical and chemical properties of polyvinyl alcohol [7, 8]

Appearance	White-to-cream granule				
	powder				
Molecular formula	(C2H4O) x				
Resin density kg/m <sup>3</sup>	1294				
Specific gravity	1.3				
Solution PH	5.0-7.0				
Specific heat J/kg.K	1674				
Refractive index	1.54				
Melting point (unplasticized	230 for fully hydrolyzed				
C°)	grades				

PVAC is a rubber polymer plant that holds the formula "C4H6O2"n, as in Figure 1. There are numerous labels for nanoparticles, nano-dot matrix, nano-powder, and titanium nanomaterials are usually (10-80) nm [9]. (Ti. Nan) have high purity and properties as shown in Table 2. (Ti. Nan) are resistant to radiation, strong, as well as have a high absorption of (U.V) rays and high transparency of (vis. L). Some applications of (Ti. Nan) are written below [10]: "nanowires and textiles, space materials, antimicrobials, antibiotics, and anti-fungal agents, plastic and soap, micro-microscopes, optical filters, coatings, nanoparticles, bandages". Applications of polymeric nanocomposites are suspended: matrix and nanofillers: Automobile bumpers, gasoline tanks, interior, and exterior panels, electronics and electrical (printed circuits, electric components), etc.

Table 2 Physical and chemical properties of titanium nanoparticles [9, 11]

Appearance	Black
True density g/cm <sup>3</sup>	4.506
Melting point co	1600
Boiling point co	3287
Average particle point	25-40
Atomic number	22
Specific surface area m <sup>2</sup> /g	50

FTIR spectra were recorded by the FTIR spectrometer in the wavenumber range (401 - 3999) cm-1. The peaks that are sharply defined are determined by which the vibration formulas correspond to the chemical bonds of all prepared films. The (SEM) is an electron microscope that takes a picture of sample surfaces with a packet of high-energy electrons in the form of a scan. The specimens for an SEM testing it is electrically connected from the surface and are electrically charged for not accumulating electrical charges on the surface [12].

#### **Experimental Part**

Materials used in this paper, (Ti nano.) "PVA - PVAC". Prepare a solution by mixing (PVA, PVAC) with (0.7, 0.3 mg) respectively with distilled water (40 ml) and make it more homogeneous use the Magnetic Stirrer) at 70C. Use nanotitanium with a weight ratio of (0, 4, 8, 12, and 16%) for some time (120-180)minutes, with the casting technique attended all samples. The samples (PVA-PVAC-Ti) nanocomposites are examined by using the "optical microscope", which is supplied from Olympus name (Toup View), under magnification (10 x) and (30 x). "FTIR spectra were recorded by FTIR (Bruker company, German origin, type vertex -70) Fourier transform infrared spectrometer in the wavenumber range (400 – 4000) cm-1". PVA, PVAC powder with (KBr) matrix was tested to prove the structure of polymerization product, we have also tested the films (polyvinyl alcohol - polyvinyl acetate) and testing of films after the addition of the weight ratios of titanium nanoparticles. The (SEM) accurate imaging device, which depicts the surface of the sample by a beam of high-energy electrons scanning.

#### Results and discussion

Figures (2) and (3) show the images of (PVA-PVAC-Ti) nanocomposites films by two magnification power, examine the samples in a magnification force (10x), and (30x) for different percentages of deflection. As shown in the image (A, B, C, D, E), the difference in the samples is indicated by the high proportion of "Ti. Nano" in poly films (PVA-PVAC), In the last film (E) with a weight of 16%, nanoparticles formed nets and chains within the polymer body, enabling these charge carriers to pass through, causing a change in the material properties [13, 14].

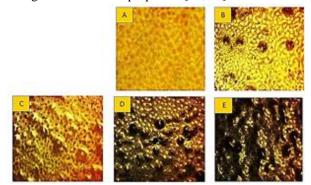


Figure 2 Photomicrographs (10x) for (PVA-PVAC-Ti) nanoparticles: (A) for (PVA-PVAC), (B) for 4wt.% Ti, (C) for 8wt.% Ti, (D) for 12wt.% Ti, (E) for 16wt.% Ti

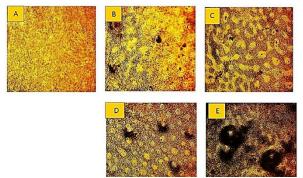


Figure 3 Photomicrographs (30x) for (PVA-PVAC-Ti) nanoparticles: (A) for (PVA-PVAC), (B) for 4wt.% Ti, (C) for 8wt.% Ti, (D) for 12wt.% Ti, (E) for 16wt.% Ti.

The interactions between ions and atoms (PVA-PVAC-Ti) nanocomposites were analyzed by the FTIR spectrometer, these interactions change due to changes in vibratory conditions of the nanocomposites. Figures 4 and 5 represent the FTIR spectra of powder PVA, PVAC, and(PVA-PVAC-Ti) nanocomposites films respectively, in the wavenumber range (400-4000) cm-1. In the case of pure PVA and PVAC Figure 4 curve a and b, a strong and broad signal at " 3200 - 3500 cm - 1 is determined to the (O - H) expansion frequency, indicating the presence of hydroxyl groups ". The bands observed at "2920 and 1720 cm-1 correspond to (C-H) and (C=O) stretching vibrations respectively, and the absorption band at 1660 cm - 1 arises due to (C=C) stretching "

In the bond 1380 cm -1 which shows the coupling (O-H), while the vibrations at 1430 cm -1 are the correlation (C - H) by oscillations. At the vibrations of (1140-1000) cm -1, a wide range of bonding bonds for these extensions were set within (C-O) and (C-O-C) groups in PVA powder, table (1.3) shows the links in polyvinyl alcohol and polyvinyl acetate. The FTIR spectroscopy of the original PVAC powder showed (C-H) bonds within strong frequencies in the range of (2800-3000 cm -1), a double bond between carbon and oxygen (C = O) at (1738 cm-1), single bonds (C-O-C) at (1241 cm-1) as (CH-O) at (1022 cm-1) and (O-CO) vibrations at (605 cm -1) and (794 cm -1), it is interesting to note that the weak absorption returns to the group of hydroxide (O-H) in the range of (3500 cm -1) [15].

Table 3 FT-IR Transmittance bands positions and their assignments for pure PVA and PVAC

Vibration frequency	Band assignment of PVA powder		
(cm <sup>-1</sup> )			
3500-3200	O-H stretching		
2950	CH <sub>2</sub> , C-H stretching vibrations		
1720	C=O stretching vibrations		
1660	C=C stretching		
1430	C-H wagging vibrations		
1380	O-H bending		
1140-1000	C-O and C-O-C stretching		
	vibrations		
3500	O-H stretching		
3000-2800	C-H stretching vibrations		
1738	C=O stretching vibrations		
1241	C-O-C stretching		
1022	CH-O stretching		
794	O-CO bending		
605	O-CO bending		

In Spectra (FTIR) of (PVA-PVAC-Ti) nanocomposite films, with the different ratio of (Ti) nanoparticles are shown in figure 5 a-b-c-d and e. The complete mission for the frequencies of distinct groups and vibrational formulas of (PVA-PVAC-Ti) nanocomposite, is presented in Table 4. From the IR spectra, we observe the proportions of different nanoparticles (Ti) differentiated by the observed changes in the spectrum (PVA-PVAC). Some of the bonds and minor changes in absorption bonds, defects, and distortions resulting from the reaction are connected to chains carrying the charge between the dopant and the polymer chain. From the spectra, the FTIR FILE Spectra of powder (a) PVA, (b) PVAC, and strong bands are observed at (3264 cm-1) is assigned to (O-H) stretching vibration of hydroxyl groups and (2911 cm-1) is assigned to (C-H) stretching vibration. A weak band is observed at (1733 cm<sup>-1</sup>), which has been assigned to the combined frequency of (C=C). The bands at (1660 cm<sup>-1</sup>) correspond to an acetyl (C=O) group. The strong band at (1417-1141 cm-1) has been attributed to the stretching mode of (C-H) and (C-O) groups. In the case of (PVA-PVAC-Ti) with different Ti ratio, when comparing spectra with pure PVA-PVAC films, it shows the change and transformation of some bands and their intensity. This reinforces the lack of significant interaction between polymers and Ti nanocomposites [15], as shown in Table 4, and Figures 5 and 6.

As shown in Figure 6 a decrease in transmittance at increasing the proportion of titanium nanoparticles. Because of the increased density of the films, and this means an increase of atoms and ions in the light path and increases the absorbance at UV inverse the IR.

Table 4 FT-IR transmittance band's positions and their assignments for (PVA-PVAC-Ti) films with different ratios of Ti nanoparticles.

Band assignment		0 wt.% Ti	4 wt.% Ti	8 wt.% Ti	12 wt.% Ti	16 wt.% Ti
O-H stretching	n <sup>-1</sup> )	3264	3255	3255	3257	3264
C-H stretching vibrations		2911	2920	2919	2921	2920
C=C stretching	rat	1733	1711	1732	1716	1731
C-H stretching	Vibr	1660	1579	1577	1575	1655
C-H bending	lrec [	1417	1413	1417	1414	1415
C-O stretching		1141	1083	1141	1085	1084

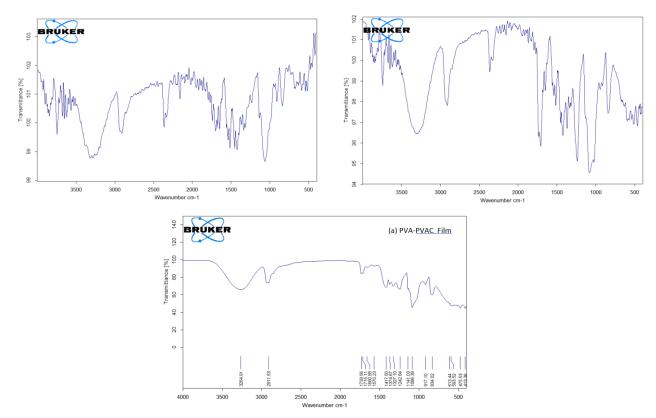
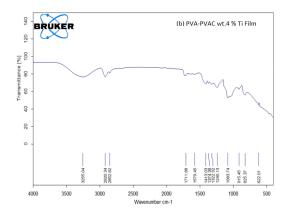
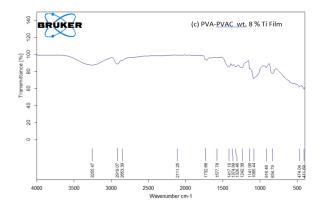
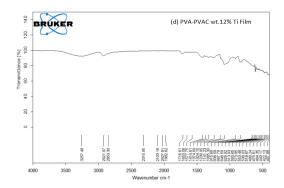


Figure 4 FTIR spectra of powder (a) PVA, (b) PVAC







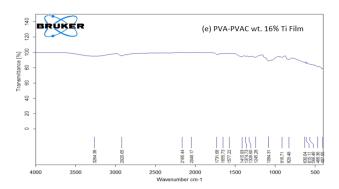


Figure 5 The FTIR spectra for (PVA-PVAC-Ti) nanocomposites film, a- pure(PVA-PVAOC)film ,b- 4wt.% Ti ,c- 8wt.% Ti, d-12wt.% Ti, e 16wt.% Ti.

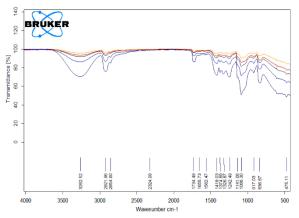


Figure 6 FTIR spectra for (PVA-PVAC-Ti) nanocomposites films to all samples.

Use the SEM micro-microscope to find images of samples and the effect of nanoparticles in the crystal structure of polymer chains. Figures 7 and 8 show images of concentrations of titanium molecules in different films (PVA-PVAC-Ti) nanocomposites. He explains, film (a) in Figures 7 and 8 shows homogeneous and softer polymers. Make sure that the addition of the (Ti) nanoparticle of the composite (PVA-PVAC-Ti) changes in the surface morphology see images (b-c-d and e), the images can be seen and we notice an increase in the titanium pool with increasing ratios in the film. It appears on all films with ratios of (Ti) nanoparticles cut on the surface making transitions and chains randomly distributed.

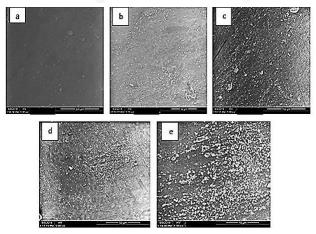


Figure 7 SEM images of (2500x) a-(0.7-0.3) PVA-PVAC film, b-4wt.% Ti, c-8 wt.% Ti, d-12 wt.% Ti, e-16 wt.% Ti nanoparticles.

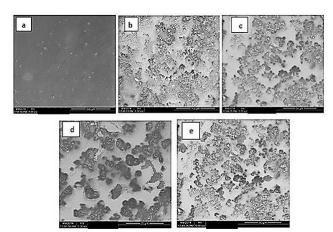


Figure 8 SEM images of (4000x) a-(0.7-0.3) PVA-PVAC film, b- 4wt.% Ti, c- 8 wt.% Ti, d- 12 wt.% Ti, e-16 wt.% Ti nanoparticles.

#### **Conclusions**

From the above, we have reached the following points:

- 1- We gave photos of the optical microscope to create a continuous network of the (Ti) nanoparticles in the nanocomposite when proportion (16wt.%).
- 2- The FTIR spectrum shows changes in some bonds between films with titanium ratios and pure (PVA-PVAC) film polymers, which indicates a great interaction. Increasing the proportion of titanium particles increases absorption, due to the increased density of films, which means increasing the ions and atoms in the light path.
- 3- Many randomly distributed pieces and aggregates formed on the surface of samples appear homogeneous and coherent, in images (SEM).

#### References

- [1] A.K. Tomar , Rishi Pal Chahal , Suman Mahendia , Shyam Kumar ,S. Sultan , Rafiuddin, M.Z. Khan, K. Umar,  $(\gamma$ -Irradiated PVA/Ag nanocomposite films) Materials for optical applications J. Alloys Compd. (2012), doi: http://dx.doi.org/10.1016/j.jallcom.2012.04.081
- [2] J. Zhao, X. Zhang, C.R. Yonzon, A.J. Haes, R.P.V. Duyne, "Nanomedicine 1", pp. 219-228 (2006).
- [3]C. Uzunpinar, "Effect of Dispersion of Swanston the Viscoelastic and Final Properties of Epoxy Based Nanocomposites", M.Sc. Thesis, Graduate Faculty, Auburn University, (2010).
- [4]J. Robertson, "Realistic applications of CNTs", Materials Today, Vol.7, No.5, pp.46-52, (2004).
- [5] M. Richardon, "Polymer Engineering Composites", Ist Ed. Applied Science Publishers Ltd. London, (1977).
- [6] A.Tawansi and H. M.Zidan, "Tunnelling and Thermally Stimulated Phenomena in Highly Filled PMMA Composites", Int. J. Polym. Mater., Vol.15, No. 2,pp.77-83,(1991).
- [7] B.L. Lopez, A.I. Mejia and L. Sierra, "Biodegrade ability of polyvinyl alcohol", Poly. Eng. and Sci., Vol.39, No. 8, pp.1346-1352,(1999).
- [8] James E. Mark, "Polymer data Handbook", Oxford University Press, Inc., (1999).
- [9] Debraj Ghosh, Sulolit Pradhan, Wei Chen and Shaowei Chen," Titanium Nanoparticles Stabilized by (Ti-C) Covalent Bonds", Journal Chem. Mater., Vol.20,No. 4, pp. 1248-1250,(2008).
- [10] Zhonghe Bi, M. Parans Paranthaman, Paul A. Menchhofer , Ryan R. Dehoff, Craig A. Bridges , Miaofang Chi , Bingkun Guo , Xiao-Guang Sun and Sheng Dai ," Self-organized amorphous TiO2 nanotube arrays on porous Ti foam for rechargeable lithium and sodium ion batteries ", Journal of Power Sources, 222 ,pp. 461-466, (2013).

- [11] Xiaohui Wei, Ralph Skomski, B. Balamurugan, and D. J. Sellmyer," Magnetism of core-shell Ti:TiO nanoparticles", J. Appl. Phys. 107, 09B516,pp.1-4, (2010).
- [12] Abdul Kareem Thottoli and Anu Kaliani Achuthanunni ," Effect of polyvinyl alcohol concentration on the ZnS nanoparticles and wet chemical synthesis of wurtzite ZnS nanoparticles", Journal of Nanostructure in Chemistry, Vol.3, No.31, pp.1-9, (2013).
- [13] Maher H. R. AL-humairi , "Study the Optical and Electrical Properties of (PVA-Ag) and (PVA-TiO2) Nanocomposites", M.Sc. thesis ,College of Education for pure sciences, University of Babylon ,(2013) .
- [14] J. Gurland, "Electrical resistivity", J. Polym. Plast. Technol. Eng., Vol.19, No.1, pp.21-51, (1982).
- [15] K. Sivaiah, K. Naveen Kumar, V. Naresh and S. Buddhudu," Structural and Optical Properties of Li+: PVP & Ag+: PVP Polymer Films ", J. Materials Sciences and Applications, Vol. 2,No.11, pp.1688-1696, (2011).



# Iraqi Journal of Nanotechnology synthesis and application



Journal Homepage: https://publications.srp-center.iq/index.php/ijn

## Dityrosine Crossed-linked Amyloid-like Fibrils as Bionanomaterials

Youssra K. Al-Hilaly<sup>1,2\*</sup>, Mahmoud B. Maina<sup>2,3</sup>, Alaa Abdul-Sada<sup>4</sup>, Louise C Serpell<sup>2\*</sup>

- 1- Chemistry Department, College of Science, Mustansiriyah University, Baghdad, Iraq,
- 2- Dementia Research group, Sussex Neuroscience, School of Life Sciences, University of Sussex, Falmer, UK
- 3- College of Medical Sciences, Yobe State University, Nigeria.
- 4- Department of Chemistry, School of Life Sciences, University of Sussex, Falmer, UK
- \*Corresponding author: Louise C Serpell email: <u>L.C.Serpell@sussex.ac.uk</u>, Youssra Al-Hilaly email: <u>youssra.alhilaly@uomustansiriyah.edu.iq</u>

#### **Keywords:**

Dityrosine cross-link; Metal-catalysed oxidation; Bionanomaterials; Functional amyloid-like fibrils

#### Abstract

Bionanomaterials have great potential for applications in tissue engineering and regenerative medicine. Recently, amyloid-like fibrils have been used in bionanomaterials preparation due to their stability and biocompatibility. Covalent dityrosine bond formation has been identified as a useful tool in the design of such bionanomaterials. In this study, two short amyloidogenic peptides containing tyrosine residues with the amino acid sequence HYFNIF and VIYKI, were used as a model system to investigate the effect of oxidation and their ability to form dityrosine cross-links. Using a range of biophysical techniques, we showed that both HYFNIF and VIYKI form dityrosine cross-linked fibrils using copper-catalysis, and phosphate buffer is more efficient in dityrosine formation. Dityrosine forms more rapidly in VIYKI fibrils compared to HYFNIF due to the fibrillar architecture. Dityrosine cross-linked HYFNIF and VIYKI fibrils could be useful to prepare bionanomaterials.

#### Introduction

Many studies have shown the utility of bionanomaterials in biomedical applications, such as regenerative medicine. These materials must be biocompatible, porous, mechanically tunable, biodegradable, easily prepared, and similar to a native cell or tissue [1, 2]. To provide some of these properties, multiple cross-linking approaches have been used in the design of bionanomaterials [3, 4] such as UV irradiation, dehydration, and chemical techniques, such as glutaraldehyde cross-linking have been used [5]. Two tyrosine residues crosslink to form dityrosine via carbon-carbon covalent bond and dityrosine has been identified as a useful tool in the design of such bionanomaterials [3]. Dityrosine is particularly interesting for bionanomaterial stabilisation because of its *in vivo* relevance as it has been shown as a cross-linker in anthropods, where it helps to stabilise resilin through the formation of a stable three-dimensional network [6]. It has been shown in several elastic and structural proteins including elastin, fibroin, keratin, cuticlin, and collagen [7-10], where it contributes to tuning the mechanical strength and subsequently the insolubility of these proteins [11]. Dityrosine also serves a protective role in proteins [12, 13]. In Ascaris suum it forms part of the structural components of the cuticle [14], and it is involved in the hardening of mosquito egg chorion [15]. In addition, dityrosine is also relevant in the context of diseases and ageing. It has been shown in amyloid plaques and lipofuscin in Alzheimer's disease [16, 17], Lewy bodies in Parkinson's disease [18],

and cataracts in the eye lens [19, 20]. The involvement of dityrosine in these amyloid diseases also highlights its importance towards understanding the working mechanism and function of functional amyloids.

To study dityrosine formation and its application to the rational design of bionanomaterials, and its relevance in functional and pathological amyloids, here, the short amyloidogenic peptides; HYFNIF and VIYKI were used as model systems. The HYFNIF is a sequence from human bloom syndrome protein and VIYKI from Drosophila chorion protein identified via the Waltz algorithm [21] and structurally validated using biophysical techniques, including transmission electron microscopy (TEM), linear dichroism (LD), circular dichroism (CD) spectroscopy and X-Ray Fiber Diffraction (XRFD) [21, 22]. Biophysical studies with short amyloidogenic peptides are particularly relevant for the development of bionanomaterials. Understanding their behaviors enables the production of new functional nanoscale materials with applications in nanotechnology and biomaterials [23]. This is especially due to their self-assembly properties that leads to very stable, ordered structures under diverse conditions, from liquid crystals to rigid nanotubes [24]. Functionalised amyloid-like fibrils with Lewis-acid-like catalytic activity were prepared from HYFNIF peptide and heterometallic Zn<sub>2</sub>Dy<sub>2</sub> complex [25]. Using HYFNIF and VIYKI peptides as a model, atomic force microscopy (AFM) has been used to provide structural basis of polymorphism within amyloid populations [26]. Both peptides contain single tyrosine (Y) each which can participate in intermolecular dityrosine cross-linking. Thus, they provide excellent model systems for investigating the structural and chemical properties of amyloids covalently cross-linked with dityrosine. Studying dityrosine cross-linking in small peptide models can enhance our understanding of dityrosine's role in the folding and assembly of other physiologically relevant peptides and proteins such as A $\beta$  and  $\alpha$ -syn, as well as, in the design of biomaterials. Here, fibrils produced from VIYKI peptide appeared to have a greater ability than HYFNIF fibrils to oxidise and form dityrosine crosslinks which suggest that the preformed VIYKI fibrils can enhance dityrosine formation by bringing two tyrosine residues in close contact for covalent cross-linking. In contrast, the tyrosine residues in the HYFNIF fibrils are oriented away from one another, and as a consequence, dityrosine formation is more restricted. The data also revealed that the pH of the oxidation environment, combined with the peptide net charge strongly influences the level of dityrosine formation. Given the stability of dityrosine cross-links, this finding will support future studies on these and similar peptides in the design of self-assembling peptides and bionanomaterials.

#### **Materials and Methods**

#### Preparation of Waltz peptide fibrils

The two lyophilised HYFNIF and VIYKI peptides capped with N-terminal acetylation and C-terminal amidation were purchased at 95% purity as TFA salts (JPT peptide Technologies, Germany). Lyophilised peptides were dissolved in Milli-Q water filtered through a  $0.22~\mu m$  filter and incubated at a concentration of 1 mg/ml for both HYFNIF and VIYKI for one week at room temperature to generate amyloid-like fibrils. TEM negative staining was used to confirm fibril formation. The stock solutions of the fibrils were stored in the dark at room temperature until required.

#### Copper-catalysed dityrosine cross-linked HYFNIF and VIYKI fibrils at neutral pH

HYFNIF and VIYKI fibrils were diluted in  $0.22 \,\mu m$  filtered Milli-Q water to a final concentration of  $0.1 \,mM$ . The diluted fibrils were incubated with CuCl<sub>2</sub> ( $0.1 \,mM$ ) and H<sub>2</sub>O<sub>2</sub> ( $2.5 \,mM$ ) at 37 °C with agitation at 300 rpm for 72 h. To monitor dityrosine formation, the fluorescence spectra were recorded over 72 h as described in fluorescence methods.

#### Tyrosine and dityrosine fluorescence

Varian Cary Eclipse fluorescence spectrophotometer (Varian Ltd., Oxford, UK) was used for fluorescence measurements using a single cell peltier accessory set at  $21\,^{\circ}$ C. Signals were collected using 1 cm path length quartz cuvette (Starna, Essex, UK). Dityrosine fluorescence was monitored with an excitation wavelength of  $320\,\text{nm}$ , and emission spectra were collected between  $340\,$  and  $500\,$  nm, with the maximum dityrosine fluorescence at around  $410\,$ –  $420\,$  nm. The tyrosine fluorescence signal was monitored with an excitation wavelength of  $280\,$  nm and emission collected at  $305\,$  nm.  $10\,$  nm excitation and emission slits were used, with  $300\,$  nm/min scan rate,  $2.5\,$  nm data intervals, and an averaging time of  $0.5\,$  s. The photomultiplier tube detector voltage was set at  $500\,$  V.

#### **Negative stain TEM**

A total of 4 µl of each fibril sample was pipetted on a Formvar/carbon-coated 400-mesh copper grid (Agar Scientific, Essex, UK). After 1-2 min incubation, excess solution was removed from the grid using filter paper. Next, the grid was washed with 4 µl filtered Milli-Q water, blotted with a filter paper and stained by the addition of 4 µl of filtered 2% (w/v) uranyl acetate. After 1 min incubation, the grid was blotted using a filter paper and allowed air-dry before examination on a Hitachi 7100 transmission electron microscope (Hitachi, Germany). The TEM was fitted with a Gatan Ultrascan 1000 CCD camera (Gatan, Abingdon, UK) and images collected at an operating voltage of 100 kV.

#### Circular dichroism spectroscopy

The conformations of the non-oxidised and copper-catalysed dityrosine cross-linked HYFNIF and VIYKI fibrils were detected by CD. Far and near UV CD spectra were recorded either in water or in 12.5 mM phosphate buffer at pH 7.4, using Jasco J-715 spectropolarimeter (Jasco UK, Great Dunmow, UK) connected to a peltier temperature control system. All spectra were recorded at  $21^{\circ}$ C with a continuous scan at a pitch of 0.1 nm and a scan rate of 50 nm/min (response time 4 sec, slit width 1 nm). The spectra were recorded between 180 - 320 nm by averaging triplicate scans and corrected by subtracting the averaged triplicate scans of blank buffer spectra. Quartz demountable cuvettes (Starna Scientific Ltd) were used to collect the CD spectra, and generally, the path lengths were between 1-0.1 mm to obtain better spectra with a high-tension voltage (HT [V]) of > 600. Raw data was processed and converted into molar ellipticity (degree.cm². dmol⁻¹) using the following equation:

$$\theta \text{ (deg.cm}^2\text{.dmol}^{-1}) = 100. \ \theta \text{ (mdeg) / c (M). 1 (cm)}$$

Where I is path length in cm, c is the molar concentration of the sample in mole/L, and  $\theta$  is ellipticity reading in mdeg.

#### Linear dichroism artifact identification

Detection of Linear dichroism artefacts, which arise from the orientation effects of fibrils, was investigated by placing the cuvette close to the detector and recording CD spectra after rotating the cuvette  $0^{\circ}$  and  $90^{\circ}$ .

#### Sample preparation for LC-ESI MS/MS analysis

Copper-catalysed dityrosine cross-inked HYFNIF (0.1 mM) and VIYKI (0.05 mM) fibrils were prepared in water and then lyophilised using a Modulyo 4K Freeze Dryer (Edwards, Crawley, England). The lyophilised fibrils were hydrolysed using evacuated sealed tubes under acidic conditions of (6 M) HCl, 10% TFA, and 1% phenol at 110 °C for 48 h. They were then dried under nitrogen gas, dissolved in 100  $\mu$ l of 0.1% formic acid in water and filtered using a Millipore 0.22  $\mu$ m filter into a 0.2 ml tube.

#### Detection of dityrosine by LC-ESI MS/MS

A total of 20  $\mu$ l of dityrosine cross-linked HYFNIF and VIYKI fibrils hydrolysate were injected on to a Phenomenex Gemini 3u C<sub>6</sub>–phenyl 110 (150 mm x 4.6 mm, 3 micron) column using an HPLC system (Waters Alliance 2695, Ireland) coupled to the mass spectrometer (Quttro Micro Premier, triple quadruple mass spectrometer, Waters, Ireland) operated in the MRM mode with positive ESI. The mobile phase solvents were A: 0.1% formic acid in water; and B: 0.1% formic acid in acetonitrile. The gradients were as follows: t = 0 min, 0% B; t = 1 min, 0% B; t = 15 min, 100% B; t = 20 min, 100% B; t = 25 min, 0% B; t = 30 min, 0% B, and the flow rate was 200  $\mu$ l/min. Mass spectrometric detection was performed by positive ion ESI tandem mass spectrometry on a triple quadrupole mass spectrometer. Argon was used as the collision gas (Argon) at 5.95e 003 mbar at 26 ev collision energy. The conditions for the mass spectrometer were as follows; ESI voltage 3 kV, the cone voltage 35 V, the source temperature was 100 °C, and the desolvation temperature was 400 °C and 300 L/h flow rate of nitrogen gas.

#### Exploring the effect of the pH and buffer type on dityrosine cross-link formation

To investigate the effect of the pH and buffer type on dityrosine cross-link formation in both HYFNIF and VIYKI fibrils, 0.1 mM HYFNIF and 0.1 mM VIYKI fibrils were incubated respectively with  $CuCl_2$  using 1:1 molar ratio and 2.5 mM  $H_2O_2$  in a) 50 mM phosphate buffer pH 7.4 and b) 50 mM HEPES buffer pH 7.4 and the oxidation reactions were performed at 37 °C with agitation at 300 rpm for 26 h. Dityrosine formation was monitored by fluorescence and the spectra were recorded over 26 h.

#### Oxidation of HYFNIF and VIYKI fibrils for circular dichroism studies

(a) HYFNIF and VIYKI fibrils were diluted in water to a final concentration of 1 mg/ml and incubated in the presence of CuCl<sub>2</sub> at a molar ratio of 1:1 (CuCl<sub>2</sub>/peptide) and (H<sub>2</sub>O<sub>2</sub> (28.3 mM) and (37.0 mM) respectively. The oxidation reactions were performed at 37 °C with the agitation of 300 rpm for 72 h. circular dichroism spectra were recorded as explained in circular dichroism measurement using a 0.1 mm path length cuvette.

(b) 0.25 mM of VIYKI fibrils was oxidised using  $CuCl_2$  (250  $\mu$ M) and  $H_2O_2$  (6.25 mM) in 12.5 mM phosphate buffer at 37 °C with agitation at 300 rpm for 72 h. CD spectra were recorded every 24 h.

#### Immunogold labelling negative stain TEM

Dityrosine cross-linked HYFNIF and VIYKI fibrils were prepared in 12.5 mM phosphate buffer and immunogold labelled 'on grid' for dityrosine using a well described protocol [27]. A modified phosphate-buffered saline (called PBS+) was used for all dilutions and washes. Briefly, 4  $\mu$ l aliquots of the fibrils were placed onto Formvar/ carbon coated 400 mesh copper support grids, left for 1 min, then blotted with a filter paper. The grids were next blocked in normal goat serum (1:10) for 15 min at room temperature and incubated with (10  $\mu$ g/ml) mouse dityrosine monoclonal antibody (Japan Institute for the Control of Aging JaICA, Shizuoka, Japan) for 2 h at room temperature. The grids were next washed three times for two min with PBS+, and then immunolabelled in a 10 nm gold nanoparticle-conjugated goat anti-mouse IgG secondary probe (BBI solution Ltd, UK, 1:10 dilution) for 1 h at room temperature. After 5x2 min PBS+ and 5x2 min distilled water rinses, the grids were negatively stained as described in the TEM negative staining section.

#### Results

#### Using VIYKI and HYFNIF as models for preparing functional amyloid-like fibrils

Two amyloidogenic peptides previously characterised using WALTZ algorithm, VIYKI and HYFNIF [22] were selected as simple amyloid models to better understand dityrosine formation at a structural level due to their highly organised fibrillar structure and the positions of the tyrosine residues allowing for potential dityrosine formation Figure 1.

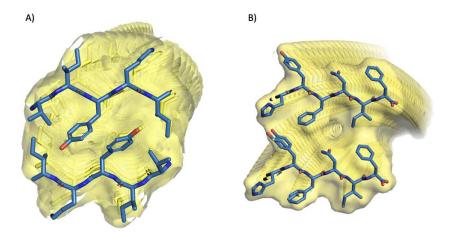


Figure 1 Structural models of protofibres formed from the two Waltz peptides, VIYKI and HYFNIF. Predicted models of amyloid protofibres made from a) VIYKI and b) HYFNIF. These models were generated and validated by comparing simulated and experimental XRFD data as described in [22].

#### Characterization of VIYKI and HYFNIF amyloid-like fibrils

VIYKI and HYFNIF form amyloid-like fibrils in water and have been previously studied using TEM, CD, LD, and XRFD (Morris et al., 2013). Here, the VIYKI and HYFNIF peptides were dissolved in water at a concentration of 1mg/ml and allowed to assemble to fibrils at room temperature for 7 days. TEM negative staining confirmed the expected long straight unbranching amyloid-like fibrils. Both peptides assembled to form laterally associated protofilaments and twisted morphologies (Figure 2, A and B). Tyrosine fluorescence spectra of the preformed amyloid-like fibrils at a concentration of  $100 \,\mu\text{M}$  revealed a strong peak at 305 nm, characteristic of the fluorescence arising from tyrosine residues (Figure 2, A and B). Comparison of the signal intensity arising from the two peptides revealed a significantly stronger signal (a.u. ~125) for fibrils formed by VIYKI compared to HYFNIF (a.u. ~40). This may reflect differences in the arrangements of the peptides within the fibrils and the exposure/burial and axial stacking of the tyrosine residues.

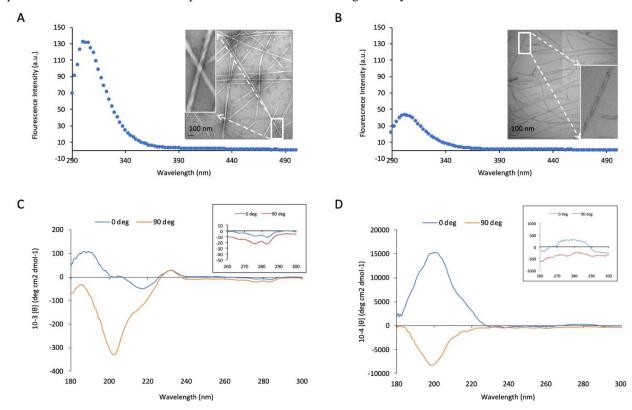


Figure 2 Structural characterisation of amyloid-like fibers. Tyrosine fluorescence spectra and transmission electron microscopy images of A) VIYKI amyloid-like fibrils and B) HYFNIF amyloid-like fibrils in the water at a concentration of  $100 \,\mu\text{M}$ . Upon excitation at  $280 \,\text{nm}$  the tyrosine residue results in a peak at  $305 \,\text{nm}$ . CD and LD spectra of C) VIYKI fibrils and D) HYFNIF recorded by positioning the cuvette at  $0 \,\text{and} \, 90 \,\text{deg}$ , showing the inversion the signal at  $200 \,\text{nm}$  which is attributed to the artefactual LD signal. The upper panel inset shows that the signal arising from contribution of tyrosine residues does not invert by positioning the cuvette at  $90 \,\text{deg}$ .

To detect the conformation of VIYKI and HYFNIF amyloid-like fibrils, the CD spectra of 1mg/ml VIYKI and HYFNIF were recorded (Figure 2, C and D). The CD spectra of HYFNIF and VIYKI fibrils showed features that were unlike commonly observed spectra shown for cross- $\beta$  rich amyloid fibrils. Although a classic  $\beta$ -sheet conformation shows a typical signal at ~ 195 (positive) and ~ 218 nm (negative), HYFNIF and VIYKI fibrils exhibited slightly shifted signals (Figure 2, C and D). VIYKI fibrils exhibited a negative signal maximum at 218 – 220 nm (Figure 2, C) that corresponds to the negative  $\beta$ -sheet signal. On the other hand, a positive maximum signal at 200 nm was observed in CD spectra of both HYFNIF and VIYKI fibrils, which could be attributed to an artefactual LD signal. Additionally, two signals arising from tyrosine were observed at 275 and 235 nm. The signal at 275 nm split into two peaks at 276 and 282 nm and was taken to arise from electron coupling of the tyrosine residues indicating proximity of tyrosines within the amyloid-like fibril structure [22, 28]. To test if the signal at 200 nm is arising from the artefactual LD signal, CD spectrum was recorded by positioning the cuvette at 90 deg, and showing the inversion signal at 200 nm which in turn indicates the orientation dependent of this signal (Figure 2, C and D).

#### Copper-catalysed dityrosine formation at neutral pH

Preformed amyloid-like fibrils (0.1 mM) HYFNIF and (0.1 mM) VIYKI were incubated for 72 h with CuCl<sub>2</sub> at 1:1 molar ratio and (2.5 mM) H<sub>2</sub>O<sub>2</sub> in water (pH of 5.0 and 6.1 respectively) at 37 °C with agitation at 300 rpm. Dityrosine formation was detected by tyrosine fluorescence, and it shows a signal at 410 nm (Figure 3, A and B) and a decline in the intensity of the in the tyrosine signal at 305 nm.

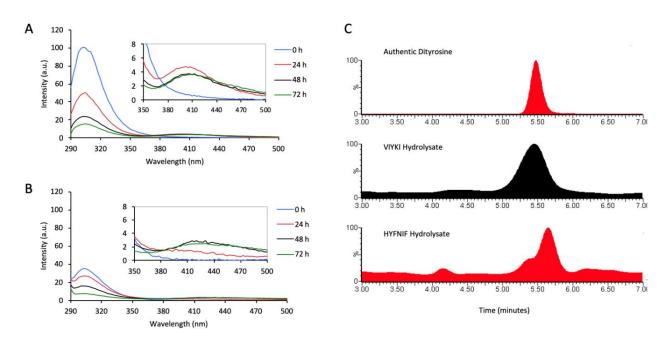


Figure 3 Dityrosine identification using tyrosine fluorescence and mass spectrometry. 0.1 mM of (A) VIYKI and (B) HYFNIF fibrils were incubated in the presence of  $\text{CuCl}_2/\text{H}_2\text{O}_2$  in water for three days at 37 °C with agitation of 300 rpm and dityrosine formation was recorded by tyrosine fluorescence. The insets showing dityrosine fluorescence signal arising at 410 nm. C) LC-ESI MS/MS chromatograms recorded in the MRM mode for dityrosine from authentic dityrosine, VIYKI and HYFNIF fibrils hydrolysate. Oxidised VIYKI and HYFNIF fibrils were obtained from the incubation of 0.05 mM VIYKI and 0.1 mM HYFNIF fibrils with  $\text{CuCl}_2/\text{H}_2\text{O}_2$  in water at 37 °C with agitation of 300 rpm.

To further confirm the dityrosine cross-links formation, hydrolysate from acidic hydrolysis of the oxidised VIYKI and HYFNIF fibrils was tested by LC-ESI MS/MS. The dityrosine formation was identified using transition reactions ions 361.1 315, the most intense transition reaction ion, and has a retention time of 5.5 min (Figure 3, C), consistent with that of authentic dityrosine.

#### Investigation of the conformational changes during dityrosine cross-links formation

CD spectra of oxidised HYFNIF and VIYKI fibrils were measured to gain insight into the effect of dityrosine cross-linking on the secondary and tertiary structures upon dityrosine formation. CD spectra of 1 mg/ml HYNIF fibrils and 1 mg/ml VIYKI fibrils before and after incubation with CuCl<sub>2</sub>/H<sub>2</sub>O<sub>2</sub> in water were recorded (Figure 4). CD showed interesting development in both near and far UV CD spectra of dityrosine cross-linked amyloid-like fibrils. Incubation of HYNIF fibrils with CuCl<sub>2</sub>/H<sub>2</sub>O<sub>2</sub> causes an appearance of a positive CD band at 190 nm, which is thought to be masked by the strong LD signal in the CD spectra of non-oxidised fibrils, and a negative signal 220 nm and is accompanied by a loss of positive LD band at 200 nm. These results suggest that oxidised fibrils have lost their ability to self-align and that may be due to formation of dityrosine cross-linked fibrils, which prevents the lateral alignment that leads to LD artefacts (Figure 2, D). The near UV CD spectrum of non-oxidised VIYKI fibrils exhibits two prominent negative signals at 276 and 282 nm, which arise from tyrosine residues. Dityrosine cross-linked VIYKI fibrils showed a significant decline in tyrosine signals at 276 and 282 nm which may correspond to the loss of tyrosine residue due to tyrosine oxidation to form dityrosine

crosslinks (Figure 4). CD spectra from dityrosine cross-linked amyloid-like fibrils are consistent with more commonly observed signatures for  $\beta$ -sheet structure and disappearance of the artefactual LD signal in the resulting CD spectra indicates less alignment of dityrosine cross-linked fibrils.

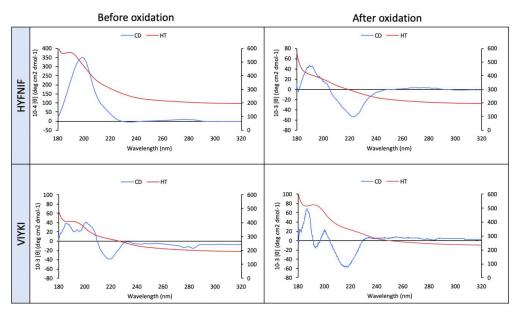


Figure 4 Structural development during dityrosine crosslink formation. CD spectra of 1 mg/ml HYNIF fibrils and 1 mg/ml VIYKI fibrils before and after incubation with  $CuCl_2/H_2O_2$  in water. Incubation of the peptides with  $CuCl_2/H_2O_2$  leads to loss of LD signal at 200 nm and increase in the  $\beta$ -sheet signals.

#### Optimization of dityrosine cross-link formation using two different buffers at pH 7.4

It has been shown that the copper ion coordination varies in different buffer conditions [29] and can form ternary complex with phosphate and precipitate as copper(II) phosphate. To optimise dityrosine formation and to explore the performance of the metal-catalysed oxidation system using different types of buffers, phosphate and HEPES buffers were used. VIYKI and HYFNIF fibrils (0.1 mM) were incubated with CuCl<sub>2</sub>/H<sub>2</sub>O<sub>2</sub> in two different buffers at pH 7.4 (50 mM HEPES buffer and phosphate buffer). The oxidation process was undertaken for 26 h at 37 °C, and dityrosine formation was monitored using an excitation wavelength of 320 nm (Figure 5 A and B). After 26 h oxidation, dityrosine signal intensity around 410 nm for VIYKI was (a.u. ~354) in phosphate buffer, while it was around (a.u. ~28) in HEPES buffer, which is about 12 times more in phosphate buffer (Figure 5, A iii). In the same manner, fluorescence data shows that HYFNIF fibrils form dityrosine in phosphate buffer better than in HEPES buffer (Figure 5, B iii). However, the results revealed that VIYKI fibrils exhibited more susceptibility to form dityrosine linkages than HYFNIF fibrils in both HEPES and phosphate buffer, and also more rapidly, as it took just 15 min to give a significant dityrosine signal in VIYKI fibrils (Figure 5, A ii), compared to the 2 h required to yield dityrosine in HYFNIF fibrils (Figure 5, B ii). In total, our results show that using phosphate buffer to perform the copper-catalysed oxidation process produces increased dityrosine formation in both HYFNIF and VIYKI peptides and that VIYKI fibrils form dityrosine linkage rapidly and more efficiently than HYFNIF. This could be attributed to the differences in the amino acid sequences of the amyloidogenic peptide and their structural architecture that affect their ability to produce dityrosine cross-links.

The morphology of the dityrosine cross-linked amyloid-like fibrils was visualised by electron microscopy and displayed a remarkable diversity (Figure 5, C). The TEM images of dityrosine cross-linked fibrils in phosphate buffer showed evidence of shortening of the VIYKI fibrils (49.0 – 863.0 nm) compared to those non-oxidised (1762.0 – 1855.0 nm), and also clumping of short fibrils. Less fragmentation was observed after 26 h of oxidation in HEPES buffer (Figure 5, C), and that may reflect the extent of oxidation using different types of buffers. Similar to VIYKI fibrils, HYFNIF fibrils underwent fragmentation upon oxidation in phosphate buffer, but TEM images showed that after 26 h of oxidation in phosphate buffer both long and short HYFNIF fibrils were observed (Figure 5, C). The fluorescence results (Figure 5, B) revealed that

HYFNIF fibrils have less ability to form dityrosine cross-links and this may result in the less affected morphology of oxidised HYFNIF fibrils. It is clear from the TEM micrographs of both dityrosine cross-linked HYFNIF and VIYKI fibrils in HEPES buffer that they underwent less fragmentation, and the main morphological change is that the fibrils became thicker and clumped together along the fibril length.

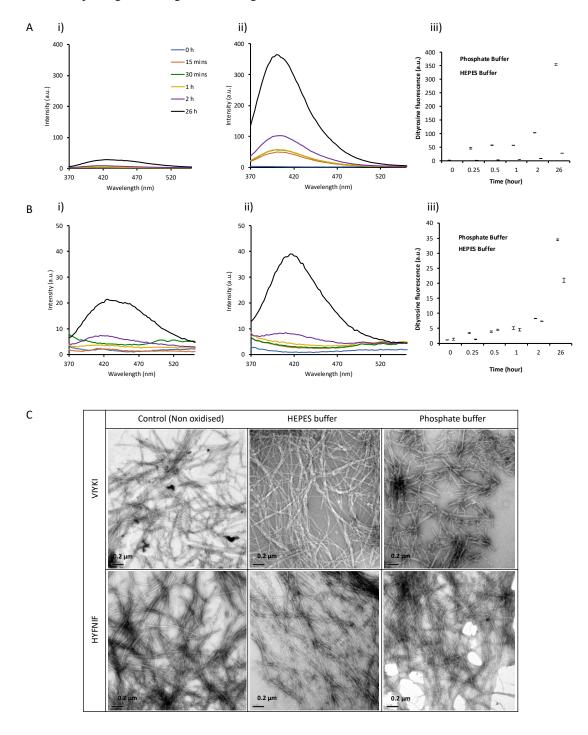


Figure 5 Copper-catalysed dityrosine cross-links formation at pH 7.4. (A) Oxidation of VIYKI fibrils in i) HEPES and ii) phosphate buffer respectively. B) Oxidation of HYFNIF fibrils in i) HEPES and ii) phosphate buffer respectively. Dityrosine formation was monitored using excitation wavelength of 320 nm. Copper-catalysed dityrosine formation in phosphate buffer was significantly higher compared to that in HEPES buffer (A, iii and B, iii). C) TEM micrographs of dityrosine cross-linked VIYKI fibrils and HYFNIF fibrils in HEPES buffer and phosphate buffer. While VIYKI fibrils underwent noticeable morphological changes upon oxidation in both HEPES and phosphate buffer, HYFNIF fibrils showed less changes especially in HEPES buffer.

As VIYKI shows more ability to form dityrosine cross-links in phosphate buffer, and to gain more insight into the conformational change for dityrosine cross-linked VIYKI fibrils, further CD experiments were performed to monitor changes in the main chain conformation of (0.25 mM) VIYKI fibrils during dityrosine cross-linking formation at pH 7.4 over 48 h. A significant decline in the intensity of the tyrosine signals at 275 nm and 235 nm was observed, indicating the loss of the tyrosine during the oxidation. Additionally, there was a significant increase in minima at 218 nm suggesting an increase in β-sheet content (Figure 6, A). No LD effect was observed after oxidation, indicating that the fibrils underwent a structural development upon oxidation that prevents fibrils from be aligned and consequently abolished the artefactual LD signal (Figure 6, B). The pH of the oxidation environment has a strong influence on the dityrosine production and that is due to the net peptide charge. Although the CD and TEM data of the oxidised fibrils revealed interesting structural and morphological changes upon the oxidation processes, no dityrosine characteristic signal was observed in CD.

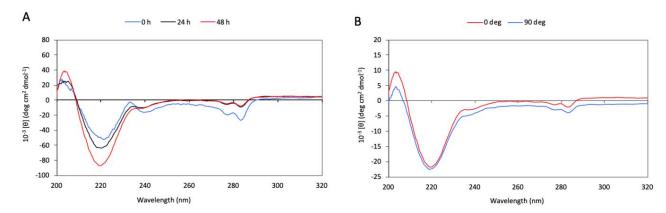


Figure 6 Conformational developments during dityrosine cross-links formation. A) CD spectrum development over oxidation of (0.25 mM) VIYKI fibrils in phosphate buffer, pH 7.4. B) LD effect was detected by collecting CD spectra of (0.1 mM) VIYKI fibrils after 48 h of oxidation in phosphate buffer, pH 7.4. The spectra were obtained by positioning the cuvette at 0 and 90 deg to the detector.

#### The distribution of dityrosine crosslinks on fibrils

To further detect the dityrosine cross-links, and show the dityrosine distribution in the oxidised fibrils, TEM immunogold labelling using a dityrosine specific monoclonal antibody was performed. Figure 7 shows labelling using an anti-dityrosine, gold-conjugated antibody on HYFNIF and VIYKI amyloid-like fibrils, revealing gold distributed close to the fibrils that were grown in an oxidising environment. Non-oxidised HYFNIF and VIYKI fibrils did not label with the dityrosine antibody. Very strong evidence of dityrosine identity was provided using these specific monoclonal dityrosine antibodies. Electron micrographs of oxidised VIYKI fibrils, which had been labelled with the gold-conjugated dityrosine antibody, revealed that dityrosine cross-links are distributed along the fibrils (Figure 7, A ii) suggesting that dityrosine coupling occurs within fibrils. Although fluorescence data showed that much higher dityrosine fluorescence intensity was generated in oxidised VIYKI fibrils (Figure 5, A), it is obvious that less gold labelling was observed in oxidised VIYKI fibrils (Figure 7, A ii) compared to oxidised HYFNIF fibrils (Figure 7, B ii), and this may support the view that dityrosine cross-link is formed internally within fibrils. Consequently, the dityrosine cross-link epitope is less accessible to bind the antibody. No labelling was observed for non-oxidised fibrils providing a strong evidence of dityrosine antibody specificity toward dityrosine versus tyrosine.

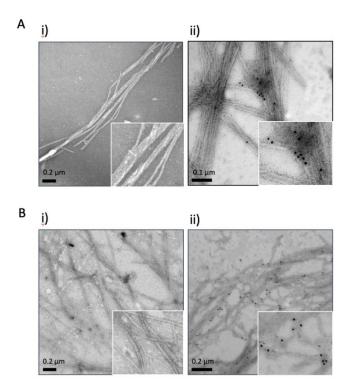


Figure 7 TEM immunogold labelling. A) VIYKI fibrils and B) HYFNIF fibrils immunogold labelled to detect dityrosine crosslinks before (i) and after (ii) oxidation. 0.1 mM VIYKI and HYFNIF fibrils were oxidised for 3 h using 0.1 mM CuCl<sub>2</sub> and 2.5 mM H<sub>2</sub>O<sub>2</sub> in 50 mM phosphate buffer, pH 7.4. The oxidation process was undertaken at 37° C, and agitation 300 rpm. The immunogold labelling micrographs shows positive labelling for dityrosine in oxidised fibrils compared with non-oxidised fibrils that did not label with dityrosine antibody.

Data presented here, suggest that the phenol groups of tyrosine residues are in close proximity to one another in VIYKI fibrils and proximity may make the carbon–carbon covalent bonding easier than in HYFNIF fibrils in which the phenol groups were arranged further away from each other (Figure 8).

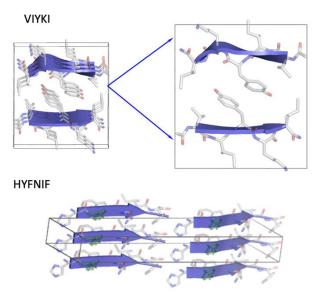


Figure 8. Proposed cell units of VIYKI and HYFNIF fibrils are determined from XRFD [22]. In VIYKI fibrils the phenol groups of tyrosine residues are orientated to be close enough to form dityrosine linkages. While, in HYFNIF the tyrosine residues are oriented away from one another, and as a consequence, dityrosine formation is more restricted. Graphics generated using PyMol.

#### **Discussion**

Dityrosine cross-links represent one of the most important modifications resulting from the oxidation of many proteins under oxidative stress conditions and could affect the protein folding and the structure. Many different models of peptides that contain tyrosine residues have been used to investigate the oxidative modification of tyrosine and formation of dityrosine linkages applying different oxidation system including MCO systems and enzymatic systems [30, 31]. Among these MCO systems, CuCl₂/H₂O₂ was the most effective to generate dityrosine and also showed a specificity to produce dityrosine [30, 31]. Dityrosine cross-links were found to increase the stability of *in vitro* amyloid-β and alpha-synuclein [16, 18]. In the current study, two short peptides containing tyrosine residues were used as a model system to generate dityrosine crosslinked amyloid-like fibrils as bionanomaterials. Fluorescence data shows that dityrosine crosslinks formed more effectively in phosphate buffer than HEPES buffer for both HYFNIF and VIYKI peptides. It has been revealed that HEPES buffer is a more suitable buffer in the protein-copper coordination studies, since it does not form ternary complexes with copper ions [29], thus HEPES would not compete with peptide and proteins to bind copper ions. However, it seems from our data that HEPES buffer is less efficient to produce dityrosine. This might be due to the formation of stable CuCl₂/peptide complexes in HEPES buffer, which in turn may have less catalytic activity.

Tyrosine fluorescence decreases when the residue goes from a more buried environment to a more solvent-exposed environment [28]. Moreover, it has been reported that in aqueous solvents the fluorescence of tyrosine (that is solvent-exposed) is quenched by the carbonyl group in the peptide bond. However the quenching mechanism is unknown [28]. From the structural model of VIYKI fibril, it is clear that tyrosine residues are located away from the fibril surface (Figure 8) which could result in less fluorescence quenching, whilst in HYFNIF fibrils, tyrosine residues are located on the fibril surface, and this may explain the tyrosine fluorescence quenching.

The potential contribution of other amino acid groups must be taken into account. It has been demonstrated that Histidine residues can form Histidine-bridge in  $A\beta$  via coordination with copper ions [32, 33]. In the same manner, we hypothesis that the HYFNIF peptide could coordinate with copper ions to form Histidine-bridges. As a result, this could affect the extent of dityrosine cross-linking. Formation of Histidine-bridged species could lead to more steric hindrance that prevents dityrosine production. Moreover, as explained previously that Histidine residue has a high affinity toward copper ions, forming a stable complex that may have less catalytic activity, yielding less dityrosine.

The structural model of the VIYKI fibrils (Figure 8) suggests that dityrosine cross-links can be formed within and between the fibrils. These results are consistent with other studies conducted on the structural features of HYFNIF and VIYKI fibrils and can be rationalized from structural models which suggest that there is close packing of the aromatic side groups, specifically tyrosine [22]. It seems that peptide side-chain packing in the structure of amyloid-like fibril significantly affects the efficiency of dityrosine cross-link formation.

#### Conclusion

In this study, the oxidative modification of the two short peptides, HYFNIF and VIYKI, using CuCl<sub>2</sub>/H<sub>2</sub>O<sub>2</sub> oxidation system was explored, and the morphological and conformational changes of these amyloid fibrils over the oxidation process were studied. The results showed that VIYKI fibrils have a greater ability than HYFNIF fibrils to oxidise and produce dityrosine cross-links, and demonstrated that the preformed fibrils could enhance dityrosine formation by bringing two tyrosine residues close enough to cross-link covalently. The results are in good agreement with structural models of HYFNIF and VIYKI fibrils from a previous study, which revealed that phenolic groups of the tyrosine residues in VIYKI fibrils pack closely together and become arranged in a proximity that could make the tyrosine cross-link more favourable. In contrast, the structural model of HYFNIF fibrils suggested that the side chain of the tyrosine residues is further away from each other, and as a consequence, dityrosine formation is more restricted. Dityrosine cross-linked amyloid-like fibrils can be prepared from both HYFNIF and VIYKI peptides and could be utilised as bionanomaterials.

#### Acknowledgements

The authors would like to thank Mustansiriyah University (www.uomustansiriyah.edu.iq) Baghdad- Iraq for its support in the present work. TEM work was performed at the School of Life Sciences TEM imaging centre at the University of Sussex and we are grateful for Dr. Julian Thorpe for his valuable help. LCS is supported by Alzheimer's Society and Alzheimer's Research UK Southcoast Network. MBM is funded by Alzheimer's Society.

#### **Author contributions**

YA planned and carried out the work and wrote the paper. MBM edited and wrote the paper. LCS and AA managed the project and wrote the paper.

#### References

- 1. Chen, Q., S. Liang, and G.A. Thouas, Elastomeric biomaterials for tissue engineering. Progress in Polymer Science, 2013. 38(3): p. 584-671.
- 2. Abbott, R.D. and D.L. Kaplan, Engineering Biomaterials for Enhanced Tissue Regeneration. Current Stem Cell Reports, 2016. 2(2): p. 140-146.
- 3. Partlow, B.P., et al., Dityrosine Cross-Linking in Designing Biomaterials. ACS Biomaterials Science & Engineering, 2016. 2(12): p. 2108-2121.
- 4. Shi, R., et al., Recent advances in synthetic bioelastomers. International journal of molecular sciences, 2009. 10(10): p. 4223-4256.
- 5. Weadock, K., R.M. Olson, and F.H. Silver, Evaluation of collagen crosslinking techniques. Biomater Med Devices Artif Organs, 1983. 11(4): p. 293-318.
- 6. Andersen, S.O., Cross-Links in Resilin Identified as Dityrosine & Trityrosine. Biochimica Et Biophysica Acta, 1964. 93(1): p. 213-215.
- 7. Labella, F., et al., Evidence for Dityrosine in Elastin. Biochemical and Biophysical Research Communications, 1967. 26(6): p. 748-&.
- 8. Raven, D.J., C. Earland, and M. Little, Occurrence of Dityrosine in Tussah Silk Fibroin and Keratin. Biochimica Et Biophysica Acta, 1971. 251(1): p. 96-&.
- 9. Fujimoto, D., Occurrence of Dityrosine in Cuticlin, a Structural Protein from Ascaris Cuticle. Comparative Biochemistry and Physiology B-Biochemistry & Molecular Biology, 1975. 51(2): p. 205-207.
- 10. Waykole, P. and E. Heidemann, Dityrosine in Collagen. Connective Tissue Research, 1976. 4(4): p. 219-222.
- 11. Skaff, O., K.A. Jolliffe, and C.A. Hutton, Synthesis of the side chain cross-linked tyrosine oligomers dityrosine, trityrosine, and pulcherosine. Journal of Organic Chemistry, 2005. 70(18): p. 7353-7363.
- 12. Kanwar, R. and D. Balasubramanian, Structure and stability of the dityrosine-linked dimer of gamma B-crystallin. Experimental Eye Research, 1999. 68(6): p. 773-784.
- 13. Bailey, A.J., The chemistry of natural enzyme-induced cross-links of proteins. Amino Acids, 1991. 1(3): p. 293-306.
- 14. Fetterer, R.H., M.L. Rhoads, and J.F. Urban, Jr., Synthesis of tyrosine-derived cross-links in Ascaris suum cuticular proteins. J Parasitol, 1993. 79(2): p. 160-6.
- 15. Li, J., B.A. Hodgeman, and B.M. Christensen, Involvement of peroxidase in chorion hardening in Aedes aegypti. Insect Biochem Mol Biol, 1996. 26(3): p. 309-17.
- 16. Al-Hilaly, Y.K., et al., A central role for dityrosine crosslinking of Amyloid-beta in Alzheimer's disease. Acta Neuropathol Commun, 2013. 1: p. 83.
- 17. Al-Hilaly, Y.K., et al., The involvement of dityrosine crosslinks in lipofuscin accumulation in Alzheimer's disease. Journal of Physics: Conference Series, 2019. 1294: p. 062107.
- 18. Al-Hilaly, Y.K., et al., The involvement of dityrosine crosslinking in alpha-synuclein assembly and deposition in Lewy Bodies in Parkinson's disease. Sci Rep, 2016. 6: p. 39171.
- 19. Wells-Knecht, M.C., et al., Oxidized amino acids in lens protein with age. Measurement of o-tyrosine and dityrosine in the aging human lens. The Journal of biological chemistry, 1993. 268(17): p. 12348-52.
- 20. Bodaness, R.S. and J.S. Zigler, Jr., The rapid H2O2-mediated nonphotodynamic crosslinking of lens crystallins generated by the heme-undecapeptide from cytochrome C: potential implications for cataractogenesis in man. Biochem Biophys Res Commun, 1983. 113(2): p. 592-7.
- 21. Maurer-Stroh, S., et al., Exploring the sequence determinants of amyloid structure using position-specific scoring matrices. Nature Methods, 2010. 7(3): p. 237-242.
- 22. Morris, K.L., et al., Exploring the sequence-structure relationship for amyloid peptides. Biochem J, 2013. 450(2): p. 275-83.

- 23. Lee, J., et al., Tyrosine-Rich Peptides as a Platform for Assembly and Material Synthesis. Advanced Science, 2019. 6(4): p. 1801255.
- 24. Cherny, I. and E. Gazit, Amyloids: not only pathological agents but also ordered nanomaterials. Angew Chem Int Ed Engl, 2008. 47(22): p. 4062-9.
- 25. Sampani, S.I., et al., Zinc-dysprosium functionalized amyloid fibrils. Dalton Transactions, 2019. 48(41): p. 15371-15375.
- 26. Aubrey, L.D., et al., Quantification of amyloid fibril polymorphism by nano-morphometry reveals the individuality of filament assembly. bioRxiv, 2020.
- 27. Vadukul, D.M., Y.K. Al-Hilaly, and L.C. Serpell, Methods for Structural Analysis of Amyloid Fibrils in Misfolding Diseases. Methods Mol Biol, 2019. 1873: p. 109-122.
- 28. Marshall, K.E., et al., Hydrophobic, aromatic, and electrostatic interactions play a central role in amyloid fibril formation and stability. Biochemistry, 2011. 50(12): p. 2061-71.
- 29. Tougu, V., A. Karafin, and P. Palumaa, Binding of zinc(II) and copper(II) to the full-length Alzheimer's amyloid-beta peptide. Journal of Neurochemistry, 2008. 104(5): p. 1249-1259.
- 30. Ali, F.E., et al., Metal catalyzed oxidation of tyrosine residues by different oxidation systems of copper/hydrogen peroxide. Journal of Inorganic Biochemistry, 2004. 98(1): p. 173-184.
- 31. Kato, Y., et al., The hydrogen peroxide/copper ion system, but not other metal-catalyzed oxidation systems, produces protein-bound dityrosine. Free Radical Biology and Medicine, 2001. 31(5): p. 624-632.
- 32. Smith, D.P., et al., Copper-mediated amyloid-beta toxicity is associated with an intermolecular histidine bridge. J Biol Chem, 2006. 281(22): p. 15145-54.
- 33. Curtain, C.C., et al., Alzheimer's disease amyloid-beta binds copper and zinc to generate an allosterically ordered membrane-penetrating structure containing superoxide dismutase-like subunits. J Biol Chem, 2001. 276(23): p. 20466-73.



# Iraqi Journal of Nanotechnology synthesis and application



Journal Homepage: https://publications.srp-center.iq/index.php/ijn

# Optical and Structural Properties of CdS Quantum Dots Synthesized Using (MW-CBD) Technique

Ahmed S. Abed<sup>1\*</sup>, Sattar J. Kasim<sup>1</sup>, Abbas F. Abbas<sup>2</sup>

- 1: Physics Department, College of Science, University of Basra, Iraq
- 2: Chemistry Department, College of Science, University of Basra, Iraq
- \*Corresponding author: Ahmed S. Abed email: ahmedalkhanjjar3@gmail.com

#### **Keywords:**

#### Nanoparticles; Quantum Dots (QDs); CdS, MW-CBD method.

#### Abstract

In the present study, the microwave heating method has been used to prepare cadmium sulfide quantum dots CdSQDs films. CdS nanoparticles size average obtained as (7nm). The morphology, structure and composition of prepared CdSQDs were examined using (FE-SEM), (XRD) and (EDX). Optical properties of CdSQDs thin films formed and deposited onto glass substrates have been studied at room temperature using UV/ Visible spectrophotometer within the wavelength of (300-800nm), and Photoluminescence (PL) spectrum. The optical energy gap (Eg) which estimated using Tauc relation was equal (2.6eV). Prepared CdS nanoparticles thin films are free from cracks, pinholes and have high adhesion to substrate.

#### Introduction

Recently, interest in nanomaterials has increased due to their unique properties in fields different [1]. The fundamental properties of materials such as electrical, optical and magnetic properties, can be controlled using controlling the size of nanomaterials without changing their chemical composition [2]. The importance of semiconductor nanomaterials is connected to industrial research and development, due to its electronic and optical properties dependent on the size of nanomaterials. thus, it is used in different fields [3,4]. In particular, sulfides of transitional metals acquired attention for applications such as sensors, optical filters, solar cells, and photovoltaic systems among others because the optical properties characteristic of the size and morphology of the crystal, essentially characterized by the transition phase from the electrical conductivity [3]. There are different methods for preparing nanomaterials [5-7].

Inorganic nanocomposites such as (CdS, CdSe and CdTe) have many properties such as, can be controlled optical energy gap and high light absorption [8]. The great importance of CdS nanoparticles due to has properties and its high absorption in the visible region, so many methods were used to prepare, such as (CBD), (MW-CBD), (SILAR) [9-12]. Because of CdS properties, widely used in different applications [13]. It is one of the most studied materials with a direct bandgap of 2.42 eV [14]. CdS nanoparticles have been studied due to its potential technological applications in field-effect transistors, solar cells [15], light-emitting diodes, photocatalysis, fluorescence probe [16], infrared photodetector, environmental sensors and biological sensors [5]. The study of optical and electrical properties CdS quantum dots has become of great importance to more researchers. [17]. By defining and controlling the methods and variables can be the preparation of CdS nanoparticles is high-quality [18]. There are many techniques to prepare CdS quantum dots, but they are costly, at high temperatures and

requires long preparation time, making those methods either expensive, explosive, moisture sensitive, extremely toxic, and energy-consuming [19,20].

The use of (MW-CBD) technique in preparing nanomaterials showed very rapid growth due to the homogeneous molecular thermal reaction [21]. The size and structure of prepared nanomaterials can be influence by the solvent at using (MW-CBD) technique [22]. Because of polarity has water, it is considered one of the best solvents used in the (MW-CBD) technique [23]. Therefore, due to (MW-CBD) technique properties are widely used in the preparation of nanomaterial.

In the present paper, CdS nanoparticles are deposited using (MW-CBD). The structural, morphological, and optical properties of CdS nanoparticles have been charactered and studied.

#### **Experimental Work**

Quantum dots CdS is deposited on substrates (glass) using (MW-CBD) method. The solution containing (0.01M) in deionized water (DW) of [Cd(NO<sub>3</sub>)<sub>2</sub>] (purity (98%), Sigma Aldrich), and (0.01M) in DW of [CH<sub>4</sub>N<sub>2</sub>S] (purity (99%), Sigma Aldrich), are given a Cd<sup>+2</sup>, S<sup>-2</sup> ions source. [NH<sub>4</sub>CH<sub>3</sub>COO] (purity (98%), HoneyWell), with (1M) in DW to control reaction rate, a buffer solution is added [24]. Ammonia solution (purity (98%), HoneyWell), is added to adjust the pH of the solution to (10). After stirred the solution for (5min), the solution in the beaker is transferred to a microwave oven with (2.45GHz frequency, LG, Korea) and the temperature is fixed at (70°C) and the duration time is (45min). Finally, washed the samples by DW after completing the preparation to take off any impurities. The yellowish layer indicates the preparation CdS nanoparticles. The CdS nanoparticles thin films obtained were free of cracks and high adhesion on substrates.

Structural properties studied using X-ray diffraction (XRD) (X'Pert PRO, Philips Company, Holland). The composition of CdSQDs films was studied by energy dispersion X-ray spectroscopy (EDX) (NOVA NanoSEM, FEI Company, USA). Morphology studded by (FE-SEM) (NOVA NanoSEM, FEI Company, USA) operating at 10.0 kV. Optical measurements at RT using (UV–Vis. SHIMADZU Company, 1800, Japan) spectrophotometer and photoluminescence (PL) spectrum was recorded using a (SHIMADZU Company, RF-5301, Japan).

#### The reaction of preparation CdS nanoparticles

The reaction below refers to the production of ammonium ions and hydroxide as a result of adding an ammonia solution to the water:

$$NH_3 + H_2O \longleftrightarrow NH_4^+ + OH^- \tag{1}$$

Dissolution [Cd(NO<sub>3</sub>)<sub>2</sub>] in DW leads to provide free (Cd<sup>+2</sup>) ions, (Cd<sup>+2</sup>) ions react with the ( $OH^-$ ) produce [Cd(OH)<sub>2</sub>]. Finally, react with ( $NH_3$ ) obtained [Cd(NH<sub>3</sub>)<sub>4</sub>] <sup>+2</sup>. As shown in the interaction below [2].

$$Cd^{+2} + 2OH^{-} \longleftrightarrow Cd(OH)_{2} \tag{2}$$

$$Cd(OH)_2 + 4NH_3 \leftrightarrow [Cd(NH_3)_4]^{+2} + 2OH^-$$
 (3)

Adding (CH<sub>4</sub>N<sub>2</sub>S) leads to the production of S<sup>-2</sup> ions, shown equations below:

$$(NH_2)_2 CS + OH^- \longleftrightarrow SH^- + CN_2H_2 + H_2O$$
 (4)

$$SH^- + OH^- \longleftrightarrow S^{-2} + H_2O \tag{5}$$

Finally, CdS nanoparticles obtained using reaction [Cd(NH<sub>3</sub>)<sub>4</sub>]<sup>2+</sup> complex with S<sup>-2</sup> ions as shown below:

$$[Cd(NH_3)_4]^{+2} + S^{-2} \longleftrightarrow CdS + 4NH_3 \tag{6}$$

The concentration of  $OH^-$  ions is very dependent on the pH value that in turn very affected by the temperature. Furthermore, the stability constant of a complex is temperature-dependent where increasing temperature led to increasing dissociation of the complex. Therefore, the temperature of the reaction is a very important parameter in the (MW-CBD) method [20].

### Results and Discussion Structural analysis

Figure 1 shows XRD pattern CdSQDs prepared. The pattern refers, three diffraction peaks consistent to angle  $(2\theta)$  23.37°, 26.66° and 29.05° for the sample. This peaks positions consistent with planes of h (100), h (002) or c (111) and h (101) which refers to a Zincblend a hexagonal structure, correspond with (ICCD-PDF4 No.00-001-0647 and 00-001-0780) [2]. Other peaks consistent to angle  $(2\theta)$  39.03°, 44.20°, 47.37° and 51.78° consistent to planes h (102), h (110) or c (220), h (103) and h (112) [25,26]. In general, it is difficult to determine whether the primary lattice phase of a compound CdS is hexagonal or cubic due to convergence diffraction peaks. However, the plans (100), (101), (103) and (112) if the primary lattice phase is hexagonal. The grain size CdS nanoparticles were estimated by Scherer's relationship [27].

$$G \cdot S = \frac{0 \cdot 9\lambda}{\beta \cos \theta} \tag{7}$$

Where (G.S) grain size,  $\lambda$  wavelength,  $\beta$  FWHM (radians), and  $\theta$  diffraction angle. The grain size average was CdS nanoparticles (12.23 nm).

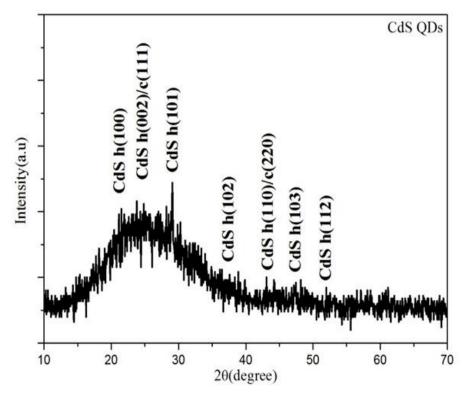


Figure 1 XRD of CdSQDs thin film.

#### Morphological and EDX characterization

Morphological characteristics of CdS quantum dots were analyzed using (FE-SEM) captured at different magnifications as shown in Figure 2 (a and b), which refers to formation of quantum dots. Particles form larger groups [2]. It showed that the particles exhibited spherical granules like structure [28]. It should be noted that generally, CdS layers have good adhesion

with the surface of the substrate. The thickness of thin-film CdSQDs was measured using field emission scanning electron microscopy (cross-section) shown in Figure 2 (c). The thickness of the sample was ranged (37.77nm). In addition, Figure 2 (d) illustrates the diameters average distribution of the CdSQDs sample on the substrate. it should be noted that in the manufacture of optical-electronic devices, especially solar cells, the porous structure materials are the best to use. The results of (EDX) are analyzed to confirm the purity of (CdS). (EDX) of CdS quantum dots is shown in Figure 3 and data in Table 1. The results confirm purity present in the sample and from this data, the cadmium to sulfur ratio was found (1.15).

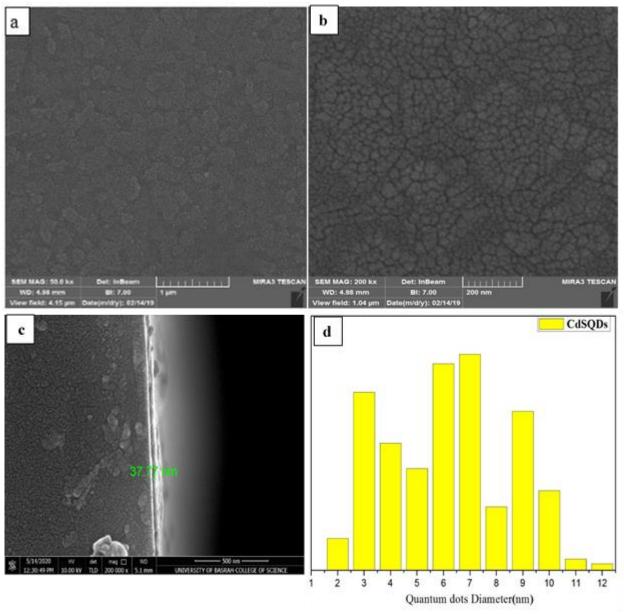


Figure 2 (a and b) FE-SEM images of CdS quantum dots thin film at different magnifications, (c) cross-section images of CdS quantum dots thin film, (d) diameters average distribution.

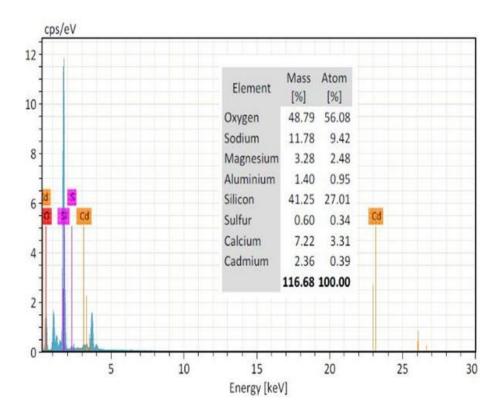


Figure 3 EDX of CdS quantum dots thin film prepared on a glass substrate

#### **Optical properties**

#### **Optical absorption**

The most dramatic property of semiconductor nanoparticles is the size evolution of optical absorption spectra. Hence UV-visible absorption spectroscopy is an efficient technique to monitor the optical properties of quantum-sized particles. The bulk bandgap of CdS is 2.42eV [29]. UV-visible absorption studied at RT within the wavelength of 300-800 nm. The UV-visible absorption of CdSQDs sample prepared is shown in Figure 4. The maximum absorption for CdS as a bulk material is around 460 nm. This result is the corresponding value reported [3]. Absorption of CdS changes with the particle size. A shift of 460 nm absorption compared with the characteristic absorption of bulk CdS may be due to quantum confinement effects. In our study (Eg) is estimated by the Tauc relationship [30]. The absorption coefficient ( $\alpha$ ) was estimated by the relationship [31].

$$\alpha = \frac{2 \cdot 303}{d} A \tag{8}$$

Where (d) thin-film thickness and (A) absorption. Optical energy bandgap (Eg) was estimated by relationship [32].

$$\alpha h \nu = B(h \nu - Eg)^{1/2} \tag{9}$$

The (Eg) value determined from Figure 5 is (2.6eV), bandgap value was higher than the bulk CdS band gap (2.42 eV) due to the confinement effect due to small particle size. Particle radius (R) was estimated by relationship [2]:

$$\Delta E_g = \frac{\hbar^2 \pi^2}{2R^2} \left( \frac{1}{m_e^*} + \frac{1}{m_h^*} \right) - \frac{1 \cdot 8e^2}{4\pi\varepsilon\varepsilon R}$$
 (10)

Where  $(m_e^*)$  and  $(m_h^*)$  effective masses electron and hole, (h) Planck's constant, (e) electron charge,  $(\varepsilon_{\circ})$  permittivity of free space  $(8.854 \times 10^{-12} \text{ C2N}-1\text{m}-2)$ ,  $(\varepsilon)$  relative permittivity.

Particle size (P·S) of CdS (P·S = 2R), estimated size CdS 7.5 nm (Table 1) which indicate quantum size effect. It can be observed the results estimated size nanoparticles CdS prepared were close to all methods used. The observed result of (XRD) estimated particle size was different, because (XRD) measures size particle group (grain size) corresponding to the

diffraction peaks using the Bragg relationship. Therefore, the grain size obtained from Scherrer's relationship, an estimate of the average unit cell size [2].

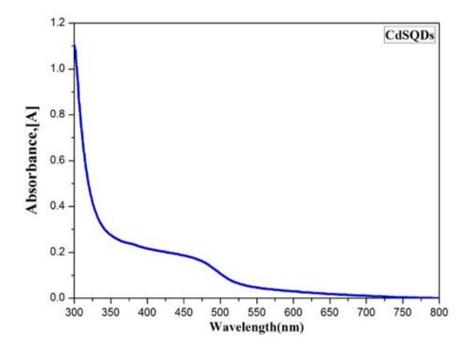


Figure 4 Absorption spectrum for CdS quantum dots.

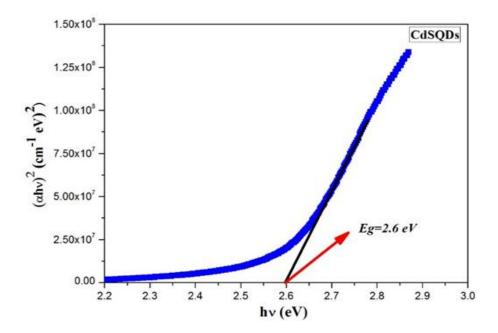


Figure 5 Estimated bandgap from the optical absorption spectrum for CdS quantum dots.

Table 1 Eg and CdS particle size (P·S).

Sample	<b>Eg</b> (eV)	P·S average (nm)		
	Ly (CV)	XRD(G.S)	FE-SEM	Mass model
CdS	2.6	12.23	7	7.5

The photoluminescence (PL) spectrum of CdS quantum dots, refers to light emission due to the return electrons from the excited state to the ground state after an incident with a monochromatic wavelength on it. Most, light incident onto CdS quantum dots is absorbed by atoms in the outside layers of nanoparticles, due to the low intensity of the lamp used. The result of (PL) spectra should refer to available energy states at the outside layers of CdS quantum dots. Figure 6 shows the room temperature photoluminescence (PL) spectrum of the quantum dots CdS at 220 nm excitation wavelength. The emission spectrum shows four important bands. Its band at 440 nm (highest peak) is the band-edge photoluminescence peak for CdS quantum dots [33]. The second band at (470) nm refers (Eg) the transition of CdS quantum dots. The third band at (480-525) nm refers to the (Eg) transition of bulk CdS, band at 658 nm refers to electron transition of defects in CdS structure. [34]. The (FWHM) of PL is 10nm, it reveals that the narrow size distribution of nanoparticles [5]. Crystalline defects or impurities may be due to a high reaction temperature or solution pH values. The blue shift and high peak intensity observed in the figure indicate quantization in CdS nanoparticles particles [35,36].

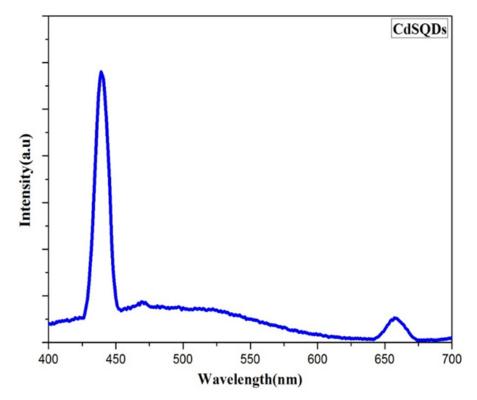


Figure 6 Photoluminescence (PL) spectrum of CdS quantum dots.

#### Conclusion

In the present work, the synthesis of CdS nanoparticles (Quantum Dots) thin film at size average (7) nm via (MW-CBD) on substrates (glass) successfully. The presented route can easily fabricate CdS nanoparticles with small dimensions in short periods and at (70°C) temperature. CdS quantum dots have been analyzed by XRD, FE-SEM, EDX, UV-Vis, and PL. The result of XRD studies, illustrated all XRD peaks corresponded to CdS quantum dots. Great homogeneity and fewer pinholes and cracks of CdSQDs thin film prepared are illustrated (FE-ESM) results. The results of (EDX) are analyzed confirm the purity of (CdS), the results confirm purity present in the sample and from this data, the cadmium to sulfur ratio

was found (1.15). The optical band gap (Eg) of CdSQD was determined by using UV-Vis spectra it was found of (2.6 eV). The (Eg) value was higher than the bulk CdS band gap due to the confinement effect due to small particle size. In addition, the blue shift and high peak intensity observed in the PL spectrum indicate quantization in CdS nanoparticles particles. From the results obtained, it can be concluded the CdSQDs thin films prepared can be used in optoelectronic applications. The use of (MW-CBD) technique to prepare semiconductor nanoparticles is an appropriate and effective option in terms of accelerating the reaction and homogeneous heat distribution.

#### References

- [1] Chen, Y., Pepin, A, Nanofabrication: Convention and nonconventional methods, Electrophoresis, 2001, 187-207.
- [2] Mahdi, M.A. Hassan, Z, Ng ,S.S, Hassan, J.J, Mohd Bakhori, S.K, Structural and optical properties of nanocrystalline CdS thin films prepared using microwave-assisted chemical bath deposition, Thin Solid Films, 2012, 3477–3484.
- [3] De la cruz terrazas, E. C. R, Ambrosio lazaro, C, Mota gonzalez, M.L, Luque, P.A, Castillo, S. J, Carrillo-Castillo, A, A simple method for the synthesis of CdS nanoparticles using a novel surfactant Chalcogenide Letters, 2015, 147 153.
- [4] Zhu, J, Zhou, M, Xu, J, Liao, X, Preparation of CdS and ZnS nanoparticles using microwave irradiation, Materials Letters, 2001, 25–29.
- [5] Srinivasa rao, B, Rajesh kumar, B, Rajagopal reddy, Subba rao, V.T, Preparation and characterization of CdS nanoparticles by chemical co-precipitation technique, Chalcogenide Letters, 2011, 177 185.
- [6] Filipponi, L. and Sutherland, D. Nanotechnologies. Luxembourg: Europen Union, 2013.
- [7] A. Mishra, S. Saha, Fabrication and comparison of Heterojunction solar cells from CdS/PbS nanoparticles and CdS/PbS bulk, Nano Express, 2020, 1-9.
- [8] Y. Hu, B. Wang, J. Zhang, T. Wang, R. Liu, J. Zhang, X. Wang, H. Wang, Synthesis and photoelectrochemical response of CdS quantum dot-sensitized TiO<sub>2</sub> nanorod array photoelectrode, Nanoscale Research Letters, 2013, 1-5.
- [9] Ali N, Iqbal MA, Hussain ST, Waris M, Munair SA, Optoelectronic properties of cadmium sulfide thin films deposited by thermal evaporation Technique, Key Engineering Materials, 2012, 510–511.
- [10] GM, W, ZQ, Z, YY, Z, Cao, Y, Zhou, Y, GJ, X, Study of transmittance of CdS thin films prepared by spray pyrolysis, Applied Mechanics and Materials, 2012, 130–134.
- [11] Zhou LM, Hu XF, Wu SM, Effects of pH value on performance of CdS films with chemical bath deposition, Advanced Materials Research, 2012, 557–559.
- [12] Senthamilselvi, V, Saravanakumar, K, Begum, J, Anandhi, R, Ravichandran, A, Sakthivel, B, Photovoltaic properties of nanocrystalline CdS films deposited by SILAR and CBD techniques comparative study. Mater Sci Mater Electron, 2012, 302–308.
- [13] Farooq, U, Naz, F, Phul, R, Pandit, N.A, Jain, S.T, Ahmad, T, Development of Heterostructures Ferroelectric SrZrO<sub>3</sub>/CdS Photocatalyst with Enhanced Surface Area and Photocatalytic Activity, Journal of Nanoscience and Nanotechnology, 2020, 3770-3779.
- [14] Ekinci, A, Horoz, S, Şahin, O, Effect of Ce doping on the characteristic properties of CdS nanoparticles, Chalcogenide Letters, 2020, 263-268.
- [15] Ramazanov, M.A, Hajiyeva, F.V, Babayev, Y.A, Valadova, G.V, Nuriyeva, S.G, Shirinova, H.A, Synthesis and optical properties of PVC-CdS based nanocomposites, Journal of Elastomers & Plastics, 2020, 159-166.
- [16] Sheng, C.K, Alrababah, Y.M, The Role of pH on Infrared Spectral, Structural and Morphological Properties of Room-temperature Precipitated CdS Nanoparticles, Journal of Nano and electronic physics, 2020, 1-4.
- [17] Dasa, H, Boruahb, P.K, Dattaa, P, Microwave Assisted Synthesis of CdS & CdS/ZnS Core-Shell Nanoparticles and Their Characterization, International Journal of Advanced Research in Physical Science (IJARPS), 2015, 18-23.
- [18] Murray, C.B, Norris, D.J, Bawendi, M.G, Synthesis and characterization of nearly monodisperse CdE (E = sulfur, selenium, tellurium) semiconductor nanocrystalline, J.Am.Chem. Soc.,1993), 8706-8715.
- [19] Ayodhya, D, Venkatesham, M, Kumari, A.S, Mangatayaru, K.G, Veerabhadram, G, Synthesis, Characterization of ZnS nanoparticles by Coprecipitation method using various capping agents Photocatalytic activity and Kinetic study, Journal of Applied Chemistry, 2013, 1-9.
- [20] Pinilla, M.A, Moreno, L.C, Guzman, G.G, Optical and morphological properties of CdS nanoparticles thin films deposited by CBD process, Chalcogenide Letters, 2011, 601-609.
- [21] Panda, A.B, Glaspell, G, Samy, M, Microwave synthesis of highly aligned ultra-narrow semiconductor rods and wires, J. Am. Chem. Soc., 2006, 2790.

- [22] Choubey, S.K, Tiwary, K.P., Microwave assisted synthesis of CdS nanoparticles for structural and optical Characterization, International Journal of Innovative Research in Science Engineering and Technology, 2014, 10670-10674.
- [23] Entezari, M.H., Ghows, N., Micro-emulsion under ultrasound facilitates the fast synthesis of quantum dots of CdS at low temperature, Ultrason. Sonochem., 2010, 127-134.
- [24] Husham, M, Hassan, Z, Mahdi, M.A, Selman, A. M, Nanocrystalline CdS thin films growth on silicon substrate via microwave-assisted chemical bath deposition synthesis and characterization, International Journal of Technical Research and Applications, 2014, 11-13.
- [25] Devenderan, P, Alagesan, T, Panding, K, Single Pot Microwave Synthesis of CdS Nanoparticles in Ionic Liquid and Their Photocatalytic Application, International Conference on Nanoscience & Nanotechnology, 2013, 79-82.
- [26] Ibrahim, A.O, Suhail, M. A, Synthesis CdS nanocrystal by using nanoparticle in chemical method, Proceeding of 3rd scientific conference, 2009, 2175- 2180.
- [27] Soltani, N, Saion, E, Hussein, M.Z, Yunus, R.B, Navaseri, M, Characterization of CdS Nanoparticles Synthesized using Microwave assisted Polyol Method, Advanced Materials Research, 2013, 122-127.
- [28] Ashok, C.H, Venkateswara, K, Shilpa, C.H, Rajendar, V, Structural Properties of CdS Nanoparticles for Solar Cell Applications, Int. J. Pure Appl. Sci. Technol., 2014, 8-12
- [29] Al-Taay, H. F, Preparation and Characterization of Chemical Bath Deposition synthesis CdS Nanocrystalline Thin Films Iraqi Journal of Science, 2017, 454-461.
- [30] Holloway, T, Mundle, R, Dondapati, H, Bahoura, M, Pradhana, A. K, Al-doped ZnO aligned nanorod arrays: Significant implications for optic and opto-electronic Applications, Center for Materials Research.
- [31] Akhiruddin, Sugianto, Irmansyah, The Influence of Hydrothermal Duration on Structures and Optical Properties of ZnO Nanoparticles, Journal of Materials Physics and Chemistry, 2014, 34-37.
- [32] Soltani, N, Salon, E, Erfani, M, Bahrami, A, Navaseri, M, Rezabe, K, Zobir, M, Facile synthesis of ZnS/CdS and CdS/ZnS core-shell nanoparticles using microwave irradiation and their optical properties, Chalcogenide Letters, 2012, 379 387
- [33] Martinsson, L, "Low-temperature synthesis of CdS nanocrystals in aliphatic alcohols", thesis, Uppsala University, (2010.)
- [34] Carlos, A, Castaneda, R, Paola, M, Romero, M, Alonso, C.M, Hailin, H, Microwave Synthesized Monodisperse CdS Spheres of Different Size and Color for Solar Cell Applications, Journal of Nanomaterials, 2015, 1-10.
- [35] Chaudhuri, R. G, Paria, S, Core/shell nanoparticles: classes, properties, synthesis mechanisms, characterization, and applications, Chemical Reviews, 2012, 2373–2433.
- [36] Shankar, H.S, Dhote, D, Vidhale, M, A facile route for preparation of CdS nanoparticle, Sci. Revs. Chem. Commun., 2012, 427-431.



# Iraqi Journal of Nanotechnology synthesis and application



Journal Homepage: https://publications.srp-center.iq/index.php/ijn

# **Effect of Nano-coating on Molten Salts for Turbine Blades**

### Abbas Khammas Hussein 1\*, Haider Hashim Abbas<sup>2</sup>

- 1- Nanotechnology and Advance Materials Research Center, University of Technology, Baghdad, Iraq
- 2- Nanotechnology and Advance Materials Research Center, University of Technology, Baghdad, Iraq
- \*Corresponding author: 130032@uotechnology.edu.iq

#### **Keywords:**

Grey Relational Analysis; K417G; Pack Cementation; Taguchi Method.

#### **Abstract**

The purpose of this study is to optimize hot corroded pack coated Ni-based superalloy K417G using grey relational analysis. Optimization of the pack cementation parameters was performed using quality characteristics of diffusion coatings for pack cementation process, i.e., salt activator, Nanopowders master alloy powder, and wt.% Y2O3. Analysis of variance (ANOVA) was used for observing the most influencing pack cementation parameters on the quality characteristics, i.e., Na2So4-6% wt. V2O5 (kp1), 100 wt% NaSO4 (kp2), and 75 wt. % NaSO4-25 wt % NaCl (kp3). The optimal process parameters were calculated using a grey relation grade and a confirmation test was performed. Based on the analysis of variance results, the wt.% Y2O3 is the most significant controllable diffusion coating factor for the hot corroded pack coated K417G at optimum setting conditions (A2, B3, C3) i.e., activator (NaCl), master alloy (94Cr-6Al), and wt.%Y2O3 (4%). according to the quality characteristics. Grey relational analysis was successfully applied to optimization of hot corroded pack coated K417G using multi-performance characteristics.

### Introduction

High-temperature coatings are used for protecting the high-temperature components from environmental attack due to oxidation and hot corrosion. These coatings have developed from simple aluminide coatings to complex overlay and duplex coatings. Aluminide coating was prepared using a pack cementation method. Pack cementation is one of the widely used surface coating technologies to economically improve high-temperature oxidation and corrosion resistance of components [1] . Recently, the surface operating temperature of the K417 G Ni-base superalloy used in turbine blades has increased to 1200 C° and even more. High temperature has a big potential to degrade the surface of the components resulting in oxidation or corrosion which can shorten the lifetime of the components [2]. Many efforts have been undertaken to overcome this severe problem, one of them is by applying the aluminizing or chromizing coating to prevent the oxidation process on the surface of the components [3].

Aluminizing – chromizing diffusion coatings are widely used for high-temperature oxidation and hot corrosion protection of turbine blades used in engine hot sections [2]. The pack cementation method is used for the position of protective coatings on the protection against oxidation, corrosion, and damage [4]. At high temperatures, Al and Cr in the coating are oxidized and forms a thin Al2O3 and Cr2O3 scale, which works as the diffusion barrier and reduces the oxidizing speed of the base material. The coated elements are placed in the closed or half-closed containers and covered with mixture powder, which consists of metals used for deposition (Al and Cr), the halide activating agent, and inactive filler. The coating is fabricated through the reduction of metal-halide vapors on the surface of base material followed by diffusion in the solid-state between the introduced metal and the substance [5].

The good repeatability of the manufacturing process and low costs are the main advantages of the pack cementation method [6]. Generally, the pack cementation process can be classified into two types depending on its process temperature and the activity of deposition metal available in the pack. They are high-temperature low-activity and low-temperature high-activity[7]. Recently novel pack cementation coating with improved hot corrosion and oxidation resistance due to "reactive element effect"(REE)" produced using pack cementation method at low temperature on the substrate was developed [8]

In the present, the multi-objective methodology based-on the Taguchi approach and Grey Relational Analysis (GRA) has been used for the optimization of multiple parameters of coating for hot corroded of K417G alloy. The outcome of this study shall be used to explore the possible use of the developed coating for high-temperature components.

### **Experimental procedure**

The experimental work was performed by using a sample of Ni-based super alloy K417G. the Spectro-chemical analysis substrate material is reported in Table 1.

Table 1. Spectro-chemical analysis of K417G Alloy

Ele.	Cr	Co	Mo	Si	Y	Ti	Al	Ni
Wt.%	8.8	10.1	2.9	-	-	3.93	5.7	Bal.

Specimens with dimensions of approximately 20×20×5 mm were prepared. A hole of 2mm in diameter was drilled in each sample in order to hang the sample in the thermos-balance by means of a platinum wire. All surfaces, including the edges, were wet ground using 3201800 and 1200 grit silicon carbide papers.

These samples were then cleaned with water, degreased with acetone and then ultrasonically cleaned for 20 min using ethanol as a medium. After drying, the samples were stored in polyethylene Zip lock bags.

The pack powder mixture consisted of a Cr-Al master-alloy, halide salt activator (NH4Cl, NaCl and NaF) and aluminum powder as a filter. In selected packs, some alumina was replaced by Y2O3 Nano-powder (90 nm) which acted as a source of reactive yttrium (Y).

The sample was placed in a sealed stainless steel cylindrical retort of 50 mm in diameter and 80 mm in a height in contact with the packed mixture. The crucible was then put in another stainless-steel crucible of 80 mm in diameter and 140 mm

in a height. The pack cementation process was conducted at  $1150 \, \text{C}^{\circ}$  for 7 hours in the pure Ar atmosphere. A schematic illustration of the coating process is shown in Figure 1.

Following the diffusion coating process, the samples were ultrasonically cleaned and cut perpendicular to the interface. Finally, the surfaces and cross-sections were examined by scanning electron microscope (SEM) and X-ray diffraction (XRD). To characterize the surface and cross-sectional morphology of the coatings at optimum setting conditions.

Cyclic hot corrosion studies were performed in molten salts (Na2So4, NaCl, and V2O5) for 20 cycles, each cycle consisted of 5 hours heating at 700 C° in a programmable tube furnace specimens were deposited with each of these salts until a total coating weight of 5 mg/cm3. Was reaching salt coated specimens were then kept in the oven for 4 hours at 100 C°. Then they were weighed again on digital balance before exposing to hot corrosion tests in a tube furnace.

The studies were conducted for all coated specimens. After testing the specimens were cleaned in an ultrasonic bath, first in distilled water, and then in ethanol. Then they were weighed on a digital balance to determine the weight change. The parabolic rate constants. (Kp) of hot corrosion are calculated by the linear least square algorithm of the following equation [9]:

$$(W/A)^2 = K_P t \tag{1}$$

Where (W/A) = weight gain per unit area (mg/cm²), t=time of exposure (hour) and kp=parabolic rate constant (hot corrosion rate) (mg² cm⁻⁴ S⁻¹). Many efforts were made to formulate the kinetics of hot corrosion- SEM and XRD techniques were used to analyze the hot corrosion products at optimum setting conditions.

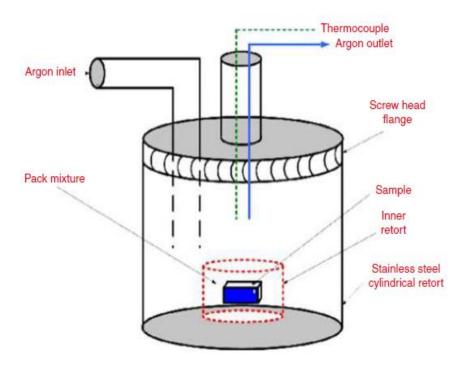


Figure 1. Pack Cementation Set-up

Experiments of hot corrosion were conducted based on the design of experiments (DOE) using the Taguchi method of three levels, each level with three factors (L9-3<sup>3</sup>) as shown in Table 2.

Control factor and levels RUN A В 

Table 2. Taguchi-Array L9

Taguchi orthogonal array- the values are taken by a factor that is termed to be leveled. The Taguchi approach is a more effective method than the traditional design of experiment methods such as factorial design, which is resource and time-consuming. It is correct to point out also the limitations of the Taguchi method. The most critical drawback of the Taguchi method is that it does not account for higher-order interactions between design parameters. Only main effects and two-factor interactions are considered. Taguchi methods, developed by Dr.Genichi Taguchi, are based on the following two ideas[10]

- 1- Quality should be measured by the deviation from the specified target value rather than by conformance to present tolerance limits.
- 2- Quality cannot be ensured through inspection and rework but must be built-in through the appropriate design of the process and product

In the Taguchi method, two factors such as the control factor and the noise factor are considered to study the influence of output parameters. The controlling factors are used to select the best conditions for a process, whereas the noise factors denote all factors that cause variation.

The following three parameters were chosen for this study: halide salt activator (A), Nano-powders (70 nm) of the master alloy (B), and weight percent of yttria (Y<sub>2</sub>O<sub>3</sub>). The values or levels for the pack cementation parameters were determined according to the thermodynamics mechanism and kinetics of the position of elements in diffusion coatings by the pack cementation method [7]. The parameters and their levels used in the experiments are shown in Table 3.

S. alad. Carrel Farre		Levels			
Symbol	Control Factor	1	2	3	
A	Activator	NH4Cl	NaCl	NaF	
В	Master Alloy	90Cr-10Al	92Cr-8Al	94Cr-6Al	
С	Wt.% Y <sub>2</sub> O <sub>3</sub>	1	2	4	

Table 3. Parameters and their levels used in the experiments

To evaluate the performance of the pack cementation process, the following output characteristics were selected: parabolic rate constants (Kp1) for hot corrosion coated Ni-based superalloy K417G in the molten salt environment, Na2So4-6% wt. V2O5 (kp1), 100 wt% NaSO4 (kp2), and 75 wt. % NaSO4-25 wt % NaCl (kp3). A simplified multi-characteristics methodology based on Taguchi's approach and grey relational analysis (GRA) has been used to optimize the performance of pack cementation coating.

### **Results and discussion**

Hot corrosion kinetics can be monitored using weigh change plots. The weight gain square (mg2/cm4) vs time (number of cycles) plots were plotted to establish the rate law for the hot corrosion. These graphs have been plotted to know the hot corrosion kinetics of specimens subjected to cyclic hot corrosion in the molten salt environment, Na2SO4, V2O5 and NaCl at 700  $^{\circ}$ C. it is observed that the coating follows a nearly parabolic rate low. The parabolic rate (hot corrosion rate) constant kp was calculated by a linear least square algorithm to function in the form (W/A)2 = kpt. The values of parabolic rate constant kp are reported in Table 4. The lower the value of kp, the higher will be the hot corrosion resistance and vice versa.

Exp.No	$K_{P1}$	$K_{P2}$	$K_{P3}$
1	1.33	1.10	1.01
2	1.24	1.21	1.91
3	1.43	0.91	0.79
4	1.35	1.13	0.80
5	1.11	1.05	0.75
6	1.02	1.14	0.97
7	1.27	1.07	0.73
8	1.92	0.81	0.88
9	1.30	0.85	0.76

Table 4. Parabolic rate constant (hot corrosion rate) kp (10<sup>-10</sup> mg<sup>2</sup> cm<sup>-4</sup> s<sup>-1</sup>)

Grey relational analysis (GRA) is a decision-making technique based on grey. The theory which is originally developed by Deng Julong. According to grey theory, there are two kinds of data that can exist namely "known" and "unknown" in the experimental investigation. These data are called in the "Grey" theory as black and white data respectively.

The black and white represent unknown information, whereas white data represents known information. Between the white and black data, there is incomplete information exists in all experiments. This incomplete information is known as the Grey system [11].

The range of each input and output factors and their respective units are different. Therefore, data must be normalized. The data processing transforms the original sequence into a comparable sequence. Hence, each response is normalized between 0 and 1. [12].

Some performance characteristics may need larger-the-better and some performance characteristics may need smaller-the-better. These two requirements use the following equations (2) and (3) respectively [13]:

$$X_{i}(k) = X_{i}(k) - \min X_{i}(k) / \max X_{i}(k) - \min X_{i}(k)$$

$$(2)$$

$$X_{i}(k) = \max X_{i}(k) - X_{i}(k) / \max X_{i}(k) - \min X_{i}(k)$$
 (3)

Where,  $X_i(k)$  and  $X_i(k)$  are the sequences after the data processing and comparability sequence respectively, min  $X_i(k)$  is the smallest value of  $X_i(k)$  for the  $k^{th}$  response and max  $X_i(k)$  is the largest value of  $X_i(k)$  for the  $k^{th}$  response, k=1, 2, 3, ... n.

$$\Delta_{0i}(k) = |X_0^*(k) - X_0^*(k)|$$
 (4)

 $\Delta_{min}$  is the minimum deviation

 $\Delta_{\text{ max}}$  is the maximum deviation

In data processing, it is necessary to establish a relation between ideal and actual normalized experimental valves. It is done by calculating the grey relational coefficient which is obtained from the relation given below:

$$\xi_{i}(k) = \Delta \min + \xi \Delta \max / \Delta_{oi}(k) + \xi \Delta \max$$
 (5)

Where:

 $\xi$  (k) = Grey relational coefficient

Σ is distinguishing coefficient fall

The parameters are given equal preference is taken as 0.5.

After obtaining the grey relational Coefficient; the grey relational grade is computed by averaging the grey relational coefficient corresponding to each performance characteristic. The overall evaluation of the multiple performance characteristics is based on the grey relational grade [14]:

$$\mathbf{y}_{i} = 1/\mathbf{n} \; \mathbf{\Sigma}^{\mathbf{n}} \; \mathbf{\Sigma}_{i} \; (\mathbf{k}) \tag{6}$$

where  $y_i$  is the grey relational grade for the i<sup>th</sup> experiment and n is the number of performance characteristics.

Based on the data sequence characteristics, data pre-processing have different methodologies pre started for the GRA [13].

Response or output can be converted into the comparative series according to Eq. (3) "smaller-the-better" characteristics.

Every one of the sequences of each performance characteristic after data processing utilizing Eq. (3) as shown in Table 5 normalization of performance characteristics.

Table 5. normalization of performance characteristics

Ex.no	Kp1	Kp2	Kp3
Reference sequence	1.000	1.000	1.000
1	0.66	0.28	0.00
2	0.76	0.00	0.36
3	0.54	0.75	0.79
4	0.63	0.20	0.75
5	0.90	0.40	0.93
6	1.00	0.18	0.14
7	0.72	0.35	1.00
8	0.00	1.00	0.46
9	0.69	0.90	0.89

Using Eq. (4) computed the deviation sequence, and the outcomes are clear in Table 6.

Table 6 deviation sequence and the outcomes of Kp values

	Δoi (1)	Δοί (2)	Δοί (3)
	1.000 7.000		7.000
Exp.no			
1	0.34	0.73	1.00
2	0.24	1.00	0.64
3	0.46	0.25	0.21
4	0.37	0.80	0.25
5	0.10	0.60	0.07
6	0.00	0.83	0.86
7	0.28	0.65	0.00
8	1.00	0.00	0.54
9	0.31	0.10	0.11

After data pre-processing is performed, GRC is determined from the normalized data to establish a relation between the preferred and real data. The distinguishing Coeff. ( $\xi$ ) has been calculated using Eq. (5) as shown in Table 7:

Table 7. grey relation grade and its order in optimization

Exp.no	13	ξ2	٤3	GRG	Rank
1	0.59	0.41	0.33	0.44	8
2	0.67	0.33	0.38	0.46	7
3	0.52	0.55	0.67	0.58	4
4	0.58	0.34	0.63	0.52	6
5	0.83	0.41	0.86	0.70	1
6	1.00	0.33	0.33	0.56	5
7	1.00	0.31	0.63	0.64	3
8	0.54	0.15	0.47	0.39	9

9 0.58 1.00	0.43	0.67	2
-------------	------	------	---

Table 7 indicates that experiment 5 has the highest GRG. It is the mal among nine experiments optimal settings of pack cementation parameters for optimization based on corrosive salts is given in Table 8.

able 8. Response table for the Grey Relational Grade

Factor	Halide salt activator	Powder of master alloy	Wt-% Yttria
Level			
1	0.4948	0.5348	0.4624
2	0.5904	0.5155	0.5481
3	0.5662	0.6012	0.6410
Rank	2	3	3

So  $(A_2B_3C_3)$  as presented in Table 8 is the optimum parameter. The level with the maximum GRG is an optimal level of the process parameter. Analysis of variance (ANOVA) results for raw data of Grey relational results, is given in Table 9 It is seen that wt%  $Y_2O_3$  (43%) significantly affects the hot corrosion rate as compared to halide salt activator (31%) and master alloy powder (26 %).

Table 9. ANOVA Table for raw data

Parameter		SS	MS	Contribution Ratio (%)
Halide salt activator	2	0.01481	0.007403	31%
Master alloy powder	2	0.01213	0.006063	26%
Wt.% Y2O3	2	0.04786	0.023930	43%

Confirmation tests a final step recommended by Grey-relational-based Taguchi approach to verify the experiment conclusion. Estimated overall grey relational Grade is calculated as follows [15]:

$$\gamma_{\text{opt}} = \gamma_{\text{m}} + \Sigma \left( \gamma_{\text{i}} - \gamma_{\text{m}} \right) \tag{7}$$

where  $\gamma_m$  is the mean of total Grey-relational Grade,  $\gamma_i$  is the mean of overall Grey relational grade at optimum level (A2, B3, C3), i the number of process parameter having significant Contribution in multiple performance characteristics. The summary results and comparison between experimental and predication results are shown in Table 10 . Figure 2 shows the cross-sectional and top-view morphology shows a thin oxide layer formed on surface which mainly contains (Cr, Al and

Y), which are playing a significant role in a protection. According to XRD pattern, it is found that  $(Cr_2O_3, Al_2O_3 \text{ and } Y_2O_3)$  oxides are mainly formed during hot corrosion and thus forms a protective oxide layer at the surface due to which further hot corrosion is prevented and the presence of yttria oxide layer in the scale improve the scale adhesion property and the scale formed are tightly adherent [16].

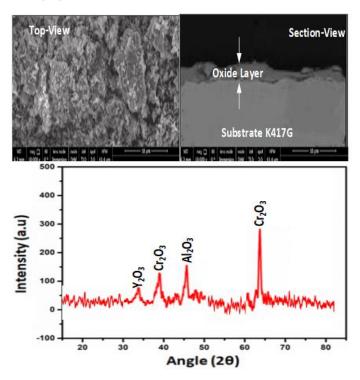


Figure 2. SEM/XRD Analysis for hot corroded pack coated K417G at optimum setting conditions

Table 10. Summary results of confirmation experiments

#### Conclusion

The results acquiring from this study can be drawn as follows:

- 1. According to grey relational analysis, the optimum.
- 2. parameters with grade value of 0.7 (closest to 1 is optimum) were A2B3C3 i.e., Activator (NaCl), master alloy (94Cr-6Al) and wt.%  $Y_2O_3$  (4%).
- 3. According to the ANOVA results, Wt.%  $Y_2O_3$  (43%) is the most significant controllable as compared to halide salt activator (31%) and master alloy powder (26 %).
- 4. According to XRD pattern, it is found that (Cr<sub>2</sub>O<sub>3</sub>, Al<sub>2</sub>O<sub>3</sub> and Y<sub>2</sub>O<sub>3</sub>) oxides are mainly formed during hot corrosion.

### References

- [1] R. Hejazi, "High Temperature Coatings For Industrial Gas Turbine Users," Accessed: Aug. 02, 2020. [Online]. Available:
- $ttps://www.academia.edu/7719406/HIGH\_TEMPERATURE\_COATINGS\_FOR\_INDUSTRIAL\_GAS\_TURBINE\_USERS.$
- [2] R. Drevet, C. Petitjean, N. David, L. Aranda, D. Veys-Renaux, and P. Berthod, "Aluminizing by pack cementation to protect CoSb3 from oxidation," *Mater. Chem. Phys.*, vol. 241, p. 122417, Feb. 2020, doi: 10.1016/j.matchemphys.2019.122417.
- [3] A. Galerie, B. Pint, and D. Monceau, "High Temperature Coatings," *Oxid. Met.*, vol. 81, no. 1, pp. 1–1, Feb. 2014, doi: 10.1007/s11085-013-9462-3.
- [4] R. Sivakumar and B. L. Mordike, "High temperature coatings for gas turbine blades: A review," *Surf. Coat. Technol.*, vol. 37, no. 2, pp. 139–160, Apr. 1989, doi: 10.1016/0257-8972(89)90099-6.
- [5] M. Okazaki, "High-temperature strength of Ni-base superalloy coatings," *Sci. Technol. Adv. Mater.*, vol. 2, no. 2, pp. 357–366, Jan. 2001, doi: 10.1016/S1468-6996(00)00022-X.
- [6] R. Rapp, "Pack Cementation Aluminide Coatings on Superalloys: Codeposition of Cr and Reactive Elements (RE). Technical Report 1. Chromium and Reactive Element(RE)- Modified Aluminide Diffusion Coatings on Superalloys: Environmental Testing. Technical Report 2," p. 115, Nov. 1992.
- [7] H. Zahedi, F. Shahriari Nogorani, and M. Safari, "Microstructure Analysis of the Pack Cementation Aluminide Coatings Modified by CeO2 Addition," *Met. Mater. Int.*, Oct. 2019, doi: 10.1007/s12540-019-00483-0.
- [8] J. Maximilien N'Gandu-Muamba and R. Streiff, "The reactive element effect (R.E.E.): a tentative classification," *J. Phys. IV Collog.*, vol. 03, no. C9, pp. C9-281-C9-290, 1993, doi: 10.1051/jp4:1993927.
- [9] "Cyclic Oxidation and Hot Corrosion Behavior of Nickel–Iron-Based Superalloy in: High Temperature Materials and Processes Volume 37 Issue 2 (2018)." https://www.degruyter.com/view/journals/htmp/37/2/article-p173.xml (accessed Aug. 02, 2020).
- [10] R. H. Myers, A. I. Khuri, and G. Vining, "Response Surface Alternatives to the Taguchi Robust Parameter Design Approach," *Am. Stat.*, vol. 46, no. 2, pp. 131–139, May 1992, doi: 10.1080/00031305.1992.10475869.
- [11] X.-C. Xiao, X.-Q. Wang, K.-Y. Fu, and Y.-J. Zhao, "Grey Relational Analysis on Factors of the Quality of Web Service," *Phys. Procedia*, vol. 33, pp. 1992–1998, Dec. 2012, doi: 10.1016/j.phpro.2012.05.313.
- [12] S.-T. Lin *et al.*, "Application of grey-relational analysis to find the most suitable watermarking scheme," *Int. J. Innov. Comput. Inf. Control*, vol. 7, Sep. 2011.
- [13] R. Sallehuddin, S. M. H. Shamsuddin, and S. Z. M. Hashim, "Grey Relational Analysis And Its Application On Multivariate Time Series.," p. 8.
- [14] Y. Kuo, T. Yang, and G.-W. Huang, "The use of grey relational analysis in solving multiple attribute decision-making problems," *Comput. Ind. Eng.*, vol. 55, no. 1, pp. 80–93, Aug. 2008, doi: 10.1016/j.cie.2007.12.002.

[15] J. Dai, X. Liu, and F. Hu, "Research and Application for Grey Relational Analysis in Multigranularity Based on Normality Grey Number," *The Scientific World Journal*, Feb. 16, 2014. https://www.hindawi.com/journals/tswj/2014/312645/ (accessed Aug. 02, 2020).

[16] D. Ghosh, S. Mukherjee, S. Das, and S. K. Mitra, "Effect of yttria(Y2O3) coating for high temperature oxidation resistance of 9Cr-1Mo steel," *Prot. Met. Phys. Chem. Surf.*, vol. 52, no. 4, pp. 737–743, Jul. 2016, doi: 10.1134/S2070205116040122.



## Iraqi Journal of Nanotechnology synthesis and application



Journal Homepage: https://publications.srp-center.iq/index.php/ijn

### **Controlling the Tube Diameter of SWCNTs Using High Melting Point Promotors**

### Haider Hassan Almkhelfe

Midland Refineries Company MRC, Ministry of Oil, Baghdad, Iraq Email: halwan@ksu.edu

### **Keywords:**

### Single-Walled Carbon Nanotubes; Ru as promoter; Chirality Control

### **Abstract**

A particular control of the diameter of Single Walled-Carbon Nanotube (SWCNT) using Chemical vapor Deposition (CVD) system will enable many promising applications in different fields. Here we demonstrate the growth of SWCNT with good control of diameter (1.5 nm  $\pm$  0.7) using a high melting temperature metal (Ru) as a catalyst promotor with the main catalyst Co at 850°C via CVD. We hypothesis that using high melting temperature metal as a promotor, like Ru can limit the mobility/change in the shape of the formed metal nanoparticles and eventually decrease the effects of Ostwald ripening (OR). FTS-GP is used as a carbon precursor. The results have been verified by high-resolution transmission electron microscopy (HR-TEM), atomic force microscopy (AFM) and multi-excitation Raman.

### Introduction

Controlling the diameter of single walled-Carbon nanotubes (SWCNTs), considered one of the challenging aspects that researchers have faced in the area of synthesizing SWNTs. Electronic and optical properties of SWCNTs highly influence their geometric orientations, like chirality index (n,m). [1] Generally, SWNT is classified either as metallic (m-SWNTs) or semiconductors (s-SWNTs) based on the tube diameter size where the tube diameter inverses proportionally with the band gap [2], which consider as the tunable electronic property of SWNTs. A big band gap tubes (s-SWNTs), preferable in the field of electronics since those big band gaps will serve as channels in the field-effective transistors (FETs) [3]. An extensive theoretical and experimental studies have concluded that catalyst particles size one of the key factors that formulate the SWCNT diameter size. [4]-[6]

The typical growth of SWNTs carpet is a coexist of both metallic and semiconductor nanotubes (wide range of SWNTs diameter) which limit their application. In order to increase the participation of SWCNTs in electronic devices, controlling the tube diameter of SWCNT is required. Recently, attempts have been focused on separating the semiconducting from metallic tubes by using physical separation like dielectrophoresis and density gradient centrifugation, also, chemical separation methods, for instance, adsorption of bromine and diazotization [7]-[10]. However, those approaches frequently lead to short and defected tube or highly contaminated which may affect the performance of the nanotube and subsequently the device performance [3]. Also, those techniques do not always offer a high selectivity besides those separation methods are non-scalable [11]. A chemical vapor deposition (CVD) method one of the processes that consider as a sufficient tool to improve the SWNTs diameter. Catalyst particle size is the main problem solver to obtain smaller diameter [12],[13], however, researchers have shown that other parameters can also be able to control the tube diameter size, such as

manipulating the growth temperature which effects the activation energy of the carbon precursor [14] or by changing the concentration of the precursor, Tian et al. was able to control the SWNTs diameter from 1.2-1.9 nm by changing the concentration of carbon dioxide [15]. An extensive survey study using density functional theory (DFT) was used to investigate different parameters that can affect the SWNTs diameter. The study concluded the catalyst particle size is one of the main parameters responsible for nucleating the SWNTs with a specific diameter [16]. Due to aggregation (Ostwald ripening), that can happen at high temperatures causing a wide range in particle size distributions. One way to overcome this problem is by leaving sufficient space between catalyst particles prevent them from aggregating and allow them to form smaller particle size [13],[16]-[19]. However, the growth results base on the catalyst particle spacing is not with sufficient dens (carpet growth) which is a very important aspect in so many applications [20]. Mattevi et al. suggested that the supporting layer AlOy plays an important rule by reducing the mobility of the iron catalyst and prevent the Ostwald ripening effects due to the strong interaction with the support at high growth temperature [21], while Kim et al. proposed the growth termination step start when the iron particles start diffuses through the alumina support [22]. Other research groups have initiate what is called "cloning growth" which is a metal-free growth system to eliminate all the termination and contamination that can be caused by metal particles [23]-[25]. This type of growth shows a good control of SWNTs chirality, and since this growth type is based on open-ends SWNTs seed, the density of the resulted growth is limited by a few tubes and they are off-substrate.

In this work, we show good control of SWNTs diameter and hence a chirality by using FTS-GP as carbon precursor and by using high melting point metals (Ru) as catalyst promoters using atmospheric pressure chemical vapor deposition (CVD). The growth results show a well-defined selective growth of narrow diameter distribution of SWNTs on cobalt and iron as main catalysts at their perspective growth temperature.

### **Experimental Work**

The morphologies and microstructures of the grown SWCNTs were studied by field emission scanning electron microscopy (FESEM) using FEI Versa 3D dual beam with multiple detectors and transmission electron microscopy (TEM). For TEM imaging, a small amount of SWCNT carpet sample was mechanically exfoliated from the substrate and dispersed in ethanol via sonication. A drop of the homogeneous suspension was deposited on a lacey carbon TEM grid and examined by TEM using FEI Tecnai F20 XT operating at 200 kv. The structure and quality of SWCNTs were characterized by Raman spectroscopy using a multi-laser wavelength of 488, 514, 633, and 785nm. Raman spectra were collected at multiple spots from the samples using a Renishaw inVia Raman microscope. Atomic force microscopy (AFM) was used for mapping the catalyst surface topography prior to and after SWCNT growth. The catalyst film with a nominal thickness of 0.5 nm Co or Fe, 0.1 nm Ru (as catalyst promotor), and 30 nm supporting layer (AlxOy) were deposited on Si (100) wafers with a native oxide layer by ion beam sputtering (IBS/e, South Bay Technology). The metal targets were etched to remove the native oxide layer prior to deposition. All films were deposited at 10-4 Torr chamber pressure using a voltage of 8 kV and a current of 6 mA under Ar flow, without exposing the films to air between depositions. The carbon feedstock (FTS-GP), supplied by Matheson Inc., had the following composition: H2 (40%), CH4 (30%), C2H6 (8%), C2H4 (6%), CO (5%), C3H8 (5%), N2 (4%), and C3H6 (2%) as a typical product mixture obtained from FTS process. [26], [27] SWCNT growth was carried out at atmospheric pressure using the EasyTube 101 CVD system (CVD Equipment Corporation), equipped with several important features including LabView-based process control software, static mixer for optimum gas mixing, and control system for precise temperature control. A typical growth run involved heating the catalyst sample to the desired temperature (850°C) at a rate of 45 °C/min in flowing Ar. At the growth temperature, the catalyst was exposed to a copious amount of H2 in combination with Ar for 2 min to reduce the catalyst; the respective flow rates were 250 standard cubic centimeters per minute (sccm) H2 and 250 sccm Ar. Thereafter, SWCNT growth under optimum conditions on a Co/Ru catalyst was initiated by introducing 10 sccm FTS-GP and 100 sccm Ar at various times. At the end of the growth run, the samples were rapidly cooled in H2, followed by slow cooling to room temperature in 700 sccm Ar.

### **Results and discussion**

A high melting temperature metal Ru was used as Co catalyst promotor to control the size of SWCNT growing by atmospheric pressure chemical vapor deposition (CVD). The dispersion without agglomeration during CVD annealing achieved with 0.1 nm of Ru used as promotors with 0.5 nm of Co. In the absence of Ru, Co catalyst experience sever Ostwald ripening (OR) as particles larger than 5 nm are formed, Figure 1, shows the atomic force microscopy of Co catalyst (a) and Co/Ru (b) after annealing in a hydrogen environment at 850°C. OR formation rate is a temperature-dependent, [28] as the growth temperature increase nanoparticles have more tendency to agglomerate via OR or sintering as an attempts to minimize their surface energy, and since the tube diameter of SWCNT is highly effected by catalyst particles size therefore an extra work needs to be invested in this area. Experiments and theoretical models have concluded that OR and subsurface diffusion are the main two critical factors affecting the size of catalyst particles, and subsequently the tube diameter in SWCNT. [29] Pretreatment of the catalyst support by ion beam bombardment and thermal annealing was found to be an effective approach to minimize the effect of OR and obtain ultra-narrow tube diameter in SWCNT. [30] Inhibiting the Ostwald ripping was also reported by introducing H2O along with H2 during annealing to reduce the diffusion rates of catalyst atoms. [31] The nanoparticles tried to minimize their surface energy by making big clusters at high temperatures.

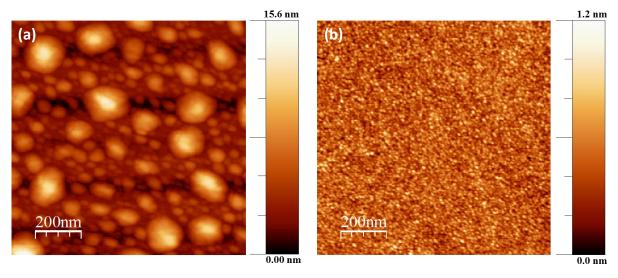


Figure 1. AFM microscopy after H2-annealing at 850°C for 5 min for Co catalyst (a) and Co/Ru catalyst (b).

Thermal dewetting of the deposited metal films into finely/homogeneously nanoparticles is highly dependent on the melting point of that metal and the porosity of the under layer.[30] We hypothesis that using high melting temperature metal as a promotor, like Ru can limit the mobility of the formed Co particles and eventually decrease the effects of OR. The same observation has been reported by using platinum (Pt) with Co as a bimetallic catalyst, [32] where Pt plays a crucial role to stabilize the Co catalyst and obtain a narrower tube diameter. Also, using Ru with Fe as a bimetallic catalyst can affordably grow SWCNT with the narrow diameter and chirality distribution.[6]

The TEM images shown in Figure 2 illustrate the morphology and tube diameter growing using AlOx supported Co-Ru (a,b) and Co (d,e). The difference in tube diameter is very obvious and further supporting the role of the high melting temperature promotor (Ru) to control the average dimeter size from 2.5 to 1.5 nm as shown in Figure 1 (c,f). Suggesting that introducing catalyst promotors can significantly impact the reaction pathway and alter the SWCNT diameter size. In comparison with adjusting the reaction parameters, Kiang et al. show that changing the reaction environment may only fine-tune the distribution.[33] The effects of Ru was investigated on Fe catalyst using TEM microscopy at 750°C with the same carbon precursor (FTS-GP). The average diameter of the grown SWCNT from Fe-Ru was smaller (1.9 nm) compared with Fe catalyst (3.1 nm). Dai et al. explained the effect of Ru in bimetallic catalyst Fe/Ru to form smaller tube dimeter to their alloying structure and strong Fe-Ru interaction to afford smaller catalyst nanoparticles stable against high temperature sintering.6

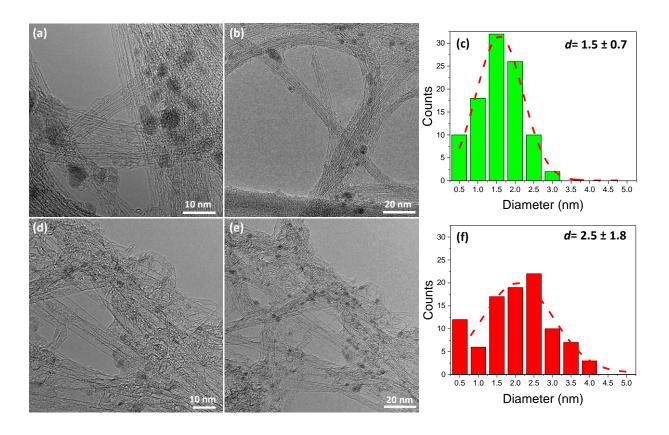


Figure 2. HR-TEM images of SWCNT growing via CVD and FTS-GP as carbon precursors at 850°C, using Co/Ru supported on AlOx (a,b) with diameter distribution (c), and using Co supported AlOx (d,e) with diameter distribution (f).

The effects of Ru were also studied on Co and Fe catalysts by using Raman scattering techniques with laser excitation wavelength in the range from 488 to 785 nm. Various Raman peaks were observed and identified with a low-frequency radial breathing mode (RBM), which is the characteristic signature of SWCNT. Figure 3 (a,b) shows the effect of Ru on Fe catalyst at its optimum temperature (750°C), where the peaks shift toward 300 cm-1 are clear. Using a laser with wavelength 488 and 514 nm introduces a new peak of Fe-Ru catalyst at Raman shift 275cm-1 while exciting the SWCNT with 633 nm, two highly intense peaks (280, 300 cm-1) are observed. Exciting the SWCNT grown by Fe-Ru catalyst with a wavelength 785 nm increase the intensity of the peak 260 cm-1 that already observed with SWCNT grown by Fe catalyst.

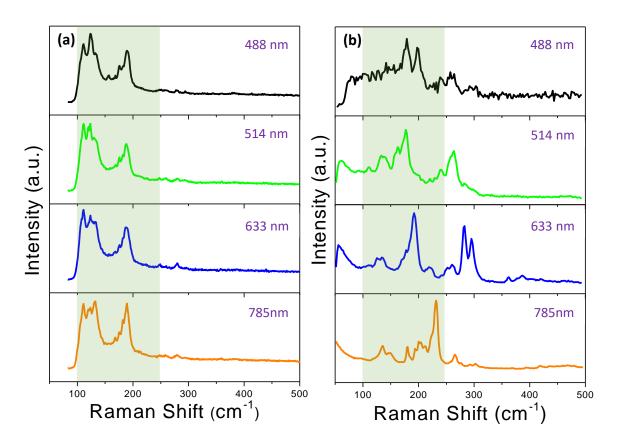


Figure 3. Multi-excitation Raman spectra of SWCNT synthesis as 750°C of Fe catalyst (a) and Fe-Ru catalyst (b).

Figure 4 Raman mapping of SWCNT grown by Co-Ru and Co at its optimum temperature (850°C). Clear differences are observed between the two samples. Although the growth of SWCNT has been carried at a much higher temperature compare with Fe catalyst, the role of Ru still effective. Multi-new peaks have been observed at high Raman shift with Co-Ru and they are in good agreement with TEM microscopy results. The laser with a wavelength of 514 nm shows the significance of using Co-Ru as an active catalyst for smaller SWCNT diameter two peaks were identified at 250 and 265 cm-1. Also, exciting the SWCNT grown by Co-Ru with 785 nm increase the intensity of the peak observed at 275 cm-1, indicating an enhancement in yield of smaller diameter size.

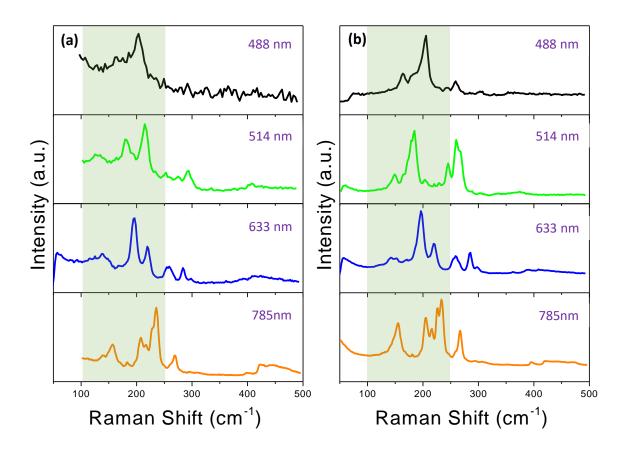


Figure 4. Figure 3. Multi-excitation Raman spectra of SWCNT synthesis as 850°C of Co catalyst (a) and Co-Ru catalyst (b).

High melting point metal tungsten (W) used with Co as a bimetallic catalyst for synthesizing SWCNT,[34] the growth results show a high selectivity toward a specific chirality (12,6). Balbuena et al. have carried a modeling simulation to predict the parameters that can influence the chirality of SWCNT.[35] Changing the catalyst shape during growth is the main factor that can impact the chirality and tube diameter size, also found by strengthening the metal-substrate interaction a more stable particle shape can be obtained. So we believe using the promotor Ru with Fe and Co catalyst controls the dewetting of the catalyst nanoparticles to offer a more stable structure shape during SWCNT growth. Using the catalyst promotor (Ru) with Co and Fe also ensures the high quality of the as-grown SWCNTs based on the intensity ratio of defect-induced D-band to tangential G-band.

Resonant Raman scattering was used to carry a comprehensive study of the chiral-index assignment of SWCANT assuming the nanotube is a homogeneous cylinder that the frequency of the RBM is linear with the inverse diameter according to empirical equation ( $\omega$ RBM= 1/d).[36] The SWCNT diameter (dt) can be calculated using the following formula: dt = 223.5/( $\omega$ RBM - 12.5) Where  $\omega$ RBM is the Raman shift of RBM of SWCNT in cm-1.

### Conclusion

SWCNT diameter size control is a prerequisite for particular applications in electronic and optoelectronic devices. We have demonstrated the role of high melting temperature metal (Ru) as a catalyst promotors with Fe and Co using ion beam sputtering for catalyst preparation. FTS-GP used as carbon precursor at 750°C for Fe catalyst and 850°C for Co. Introducing 0.1 nm of Ru into Fe or Co catalyst strongly influence the diameter size distribution of SWCNT. The average diameter size of SWCNT reduced from 2.5 nm (using Co catalyst) to 1.5 nm when Ru is used as the promoter. While using Ru with Fe catalyst reduces the diameter size of the grown SWCNT from 3.1 to 1.9 nm. Further, Ru has also enhanced the quality of the grown SWCNT by increasing the intensity of the G-band.

### References

- 1. Chiashi, S.; Kono, K.; Matsumoto, D.; Shitaba, J.; Homma, N.; Beniya, A.; Yamamoto, T.; Homma, Y. Adsorption effects on radial breathing mode of single-walled carbon nanotubes. Physical Review B 2015, 91, 155415.
- 2. Wilder, J. W. G.; Venema, L. C.; Rinzler, A. G.; Smalley, R. E.; Dekker, C. Electronic structure of atomically resolved carbon nanotubes. Nature 1998, 391, 59-62.
- 3. Li, J.; Ke, C.-T.; Liu, K.; Li, P.; Liang, S.; Finkelstein, G.; Wang, F.; Liu, J. Importance of Diameter Control on Selective Synthesis of Semiconducting Single-Walled Carbon Nanotubes. ACS Nano 2014, 8, 8564-8572.
- 4. Ding, F.; Larsson, P.; Larsson, J. A.; Ahuja, R.; Duan, H.; Rosén, A.; Bolton, K. The Importance of Strong Carbon–Metal Adhesion for Catalytic Nucleation of Single-Walled Carbon Nanotubes. Nano Letters 2008, 8, 463-468.
- 5. Ayre, G. N.; Uchino, T.; Mazumder, B.; Hector, A. L.; Hutchison, J. L.; Smith, D. C.; Ashburn, P.; Groot, C. H. d. On the mechanism of carbon nanotube formation: the role of the catalyst. Journal of Physics: Condensed Matter 2011, 23, 394201.
- 6. Li, X.; Tu, X.; Zaric, S.; Welsher, K.; Seo, W. S.; Zhao, W.; Dai, H. Selective synthesis combined with chemical separation of single-walled carbon nanotubes for chirality selection. Journal of the American Chemical Society 2007, 129, 15770-15771.
- 7. Krupke, R.; Hennrich, F.; Löhneysen, H. v.; Kappes, M. M. Separation of Metallic from Semiconducting Single-Walled Carbon Nanotubes. Science 2003, 301, 344-347.
- 8. Ghosh, S.; Bachilo, S. M.; Weisman, R. B. Advanced sorting of single-walled carbon nanotubes by nonlinear density-gradient ultracentrifugation. Nat Nano 2010, 5, 443-450.
- 9. Chen, Z.; Du, X.; Du, M.-H.; Rancken, C. D.; Cheng, H.-P.; Rinzler, A. G. Bulk Separative Enrichment in Metallic or Semiconducting Single-Walled Carbon Nanotubes. Nano Letters 2003, 3, 1245-1249.
- 10. Strano, M. S.; Dyke, C. A.; Usrey, M. L.; Barone, P. W.; Allen, M. J.; Shan, H.; Kittrell, C.; Hauge, R. H.; Tour, J. M.; Smalley, R. E. Electronic Structure Control of Single-Walled Carbon Nanotube Functionalization. Science 2003, 301, 1519-1522.
- 11. Voggu, R.; Rao, K. V.; George, S. J.; Rao, C. N. R. A Simple Method of Separating Metallic and Semiconducting Single-Walled Carbon Nanotubes Based on Molecular Charge Transfer. Journal of the American Chemical Society 2010, 132, 5560-5561.
- 12. Cheung, C. L.; Kurtz, A.; Park, H.; Lieber, C. M. Diameter-Controlled Synthesis of Carbon Nanotubes. The Journal of Physical Chemistry B 2002, 106, 2429-2433.
- 13. Nasibulin, A. G.; Pikhitsa, P. V.; Jiang, H.; Kauppinen, E. I. Correlation between catalyst particle and single-walled carbon nanotube diameters. Carbon 2005, 43, 2251-2257.
- 14. Saito, T.; Ohmori, S.; Shukla, B.; Yumura, M.; Iijima, S. A Novel Method for Characterizing the Diameter of Single-Wall Carbon Nanotubes by Optical Absorption Spectra. Applied Physics Express 2009, 2, 095006-095006-095003.
- 15. Tian, Y.; Timmermans, M. Y.; Kivistö, S.; Nasibulin, A. G.; Zhu, Z.; Jiang, H.; Okhotnikov, O. G.; Kauppinen, E. I. Tailoring the diameter of single-walled carbon nanotubes for optical applications. Nano Research 2011, 4, 807-815.
- 16. Hedman, D.; Reza Barzegar, H.; Rosén, A.; Wågberg, T.; Andreas Larsson, J. On the Stability and Abundance of Single Walled Carbon Nanotubes. Scientific Reports 2015, 5, 16850.
- 17. Lukas, D.; Jason, G.; Thomas, H.; Matthias, M.; Roland, R.; Christofer, H. Narrowing SWNT diameter distribution using size-separated ferritin-based Fe catalysts. Nanotechnology 2009, 20, 355601.
- 18. Dai, H.; Rinzler, A. G.; Nikolaev, P.; Thess, A.; Colbert, D. T.; Smalley, R. E. Single-wall nanotubes produced by metal-catalyzed disproportionation of carbon monoxide. Chemical Physics Letters 1996, 260, 471-475.
- 19. Kukovitsky, E. F.; L'Vov, S. G.; Sainov, N. A.; Shustov, V. A.; Chernozatonskii, L. A. Correlation between metal catalyst particle size and carbon nanotube growth. Chemical Physics Letters 2002, 355, 497-503.
- 20. Chen, G.; Seki, Y.; Kimura, H.; Sakurai, S.; Yumura, M.; Hata, K.; Futaba, D. N. Diameter control of single-walled carbon nanotube forests from 1.3–3.0 nm by arc plasma deposition. Scientific Reports 2014, 4, 3804.
- 21. Mattevi, C.; Wirth, C. T.; Hofmann, S.; Blume, R.; Cantoro, M.; Ducati, C.; Cepek, C.; Knop-Gericke, A.; Milne, S.; Castellarin-Cudia, C.; Dolafi, S.; Goldoni, A.; Schloegl, R.; Robertson, J. In-situ X-ray Photoelectron Spectroscopy Study of Catalyst—Support Interactions and Growth of Carbon Nanotube Forests. The Journal of Physical Chemistry C 2008, 112, 12207-12213.

- 22. Kim, S. M.; Pint, C. L.; Amama, P. B.; Zakharov, D. N.; Hauge, R. H.; Maruyama, B.; Stach, E. A. Evolution in Catalyst Morphology Leads to Carbon Nanotube Growth Termination. The Journal of Physical Chemistry Letters 2010, 1, 918-922. 23. Yao, Y.; Feng, C.; Zhang, J.; Liu, Z. "Cloning" of Single-Walled Carbon Nanotubes via Open-End Growth Mechanism. Nano Letters 2009, 9, 1673-1677.
- 24. Liu, B.; Liu, J.; Tu, X.; Zhang, J.; Zheng, M.; Zhou, C. Chirality-Dependent Vapor-Phase Epitaxial Growth and Termination of Single-Wall Carbon Nanotubes. Nano Letters 2013, 13, 4416-4421.
- 25. Liu, J.; Wang, C.; Tu, X.; Liu, B.; Chen, L.; Zheng, M.; Zhou, C. Chirality-controlled synthesis of single-wall carbon nanotubes using vapour-phase epitaxy. Nat Commun 2012, 3, 1199.
- 26. Almkhelfe, H.; Carpena-Núñez, J.; Back, T. C.; Amama, P. B. Gaseous product mixture from Fischer–Tropsch synthesis as an efficient carbon feedstock for low temperature CVD growth of carbon nanotube carpets. Nanoscale 2016, 8, 13476-13487.
- 27. Almkhelfe, H.; Li, X.; Rao, R.; Amama, P. B. Catalytic CVD growth of millimeter-tall single-wall carbon nanotube carpets using industrial gaseous waste as a feedstock. Carbon 2017, 116, 181-190.
- 28. Kharlamova, M. V. Investigation of growth dynamics of carbon nanotubes. Beilstein journal of nanotechnology 2017, 8, 826.
- 29. Sakurai, S.; Nishino, H.; Futaba, D. N.; Yasuda, S.; Yamada, T.; Maigne, A.; Matsuo, Y.; Nakamura, E.; Yumura, M.; Hata, K. Role of Subsurface Diffusion and Ostwald Ripening in Catalyst Formation for Single-Walled Carbon Nanotube Forest Growth. Journal of the American Chemical Society 2012, 134, 2148-2153.
- 30. Yang, N.; Li, M.; Patscheider, J.; Youn, S. K.; Park, H. G. A Forest of Sub-1.5-nm-wide Single-Walled Carbon Nanotubes over an Engineered Alumina Support. 2017, 7, 46725.
- 31. Amama, P. B.; Pint, C. L.; McJilton, L.; Kim, S. M.; Stach, E. A.; Murray, P. T.; Hauge, R. H.; Maruyama, B. Role of Water in Super Growth of Single-Walled Carbon Nanotube Carpets. Nano Letters 2009, 9, 44-49.
- 32. Liu, B.; Ren, W.; Li, S.; Liu, C.; Cheng, H.-M. High temperature selective growth of single-walled carbon nanotubes with a narrow chirality distribution from a CoPt bimetallic catalyst. Chemical Communications 2012, 48, 2409-2411.
- 33. Kiang, C.-H. Growth of large-diameter single-walled carbon nanotubes. The Journal of Physical Chemistry A 2000, 104, 2454-2456.
- 34. An, H.; Kumamoto, A.; Takezaki, H.; Ohyama, S.; Qian, Y.; Inoue, T.; Ikuhara, Y.; Chiashi, S.; Xiang, R.; Maruyama, S. Chirality specific and spatially uniform synthesis of single-walled carbon nanotubes from a sputtered Co-W bimetallic catalyst. Nanoscale 2016, 8, 14523-14529.
- 35. Gomez-Ballesteros, J. L.; Balbuena, P. B. Structure and dynamics of metallic and carburized catalytic Ni nanoparticles: effects on growth of single-walled carbon nanotubes. Physical Chemistry Chemical Physics 2015, 17, 15056-15064.
- 36. Maultzsch, J.; Telg, H.; Reich, S.; Thomsen, C. Radial breathing mode of single-walled carbon nanotubes: Optical transition energies and chiral-index assignment. Physical Review B 2005, 72, 205438.



## Iraqi Journal of Nanotechnology synthesis and application



Journal Homepage: https://publications.srp-center.iq/index.php/ijn

### (Au, Ag)/Al<sub>0.08</sub>In<sub>0.08</sub>Ga<sub>0.84</sub>N/ (Au, Ag) Metal-semiconductor-metal (MSM) Photodetectors

### Alaa Jabbar Ghazai\*, Marwaa Mohammed

Physics Department, Science College, Al-Nahrain University, Iraq

\*Email: alaaphys74@gmail.com

### **Keywords:**

Single- Metal-semiconductormetal;

Photodetectors; Al<sub>0.08</sub>In<sub>0.08</sub>Ga<sub>0.84</sub>N;

PA-MBE;

SBH;

QE; NEP

### **Abstract**

Metal-semiconductor-metal (MSM) photodetectors (PDs) based on gold and silver (Au, Ag)/Al0.08In0.08Ga0.84N (commercial sample)/ (Au, Ag) have been fabricated and characterized. The effect of annealing temperature of As deposit, 400, 500, and 600 0C for 30 min on the topography and electrical properties of Au contact on Al0.08In0.08Ga0.84N thin film have been characterized and optimized using Current-Voltage (I-V) characteristic. Schottky barrier height (SBH) and ideality factor (n) of Au/ Al<sub>0.08</sub>In<sub>0.08</sub>Ga<sub>0.84</sub>N interface were 1.223 eV and 1.773 at 50 0C annealing temperature for 30 min respectively, and it is found that contact has a high-quality surface. Also, with the same procedure, the effect of annealing time of 15, 30, 45 minutes, and 1 hour have been studied and optimized. The results revealed that the best annealing time is 30 min which has the highest SBH. Au contact compared with Ag contact used to first time as best our knowledge with the optimal condition to select the best metal for MSM photodetectors (PDs). The ideal characterization of Au, Ag/AlInGaN/Au, Ag MSMPDs on Si substrate depend on responsivities of 0.201 and 0.153 A W-1, quantum efficiencies of 71% and 57%, and NEPs of 3.55×10-4 and 1.45×10-3W-1, respectively have been also studied compared. The height SBH and QE for the samples grown on Si was at Au contact which proposed to use in such optoelectronic devices.

### Introduction

Although GaN has many advantages in many optoelectronic devices application however Quaternary (AlInGaN) thin films consider as promising material and it attracted much research interest because they allow almost independent control of the lattice mismatch and band off stein AlInGaN-based heterostructures. it has an attractive topic to be used in many applications for any scientific research, such as optoelectronic devices operate in a wide range of the electromagnetic spectrum. it is a benefit due to the high- quality structures and strong ultraviolet emission at RT, it also allows more freedom and independent control regarding energy gap and lattices constant [1,2]. Metal-semiconductor-metal (MSM) has been suggested in this work because of its performance. It is formed from two schottky contacts like fingers that deposit on the top of the surface as shown in Figure (1) [3].

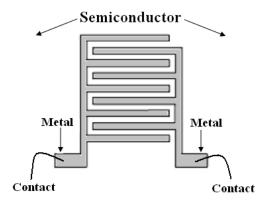


Figure 1 MSM PD structure (top view).

Gold (Au) and silver (Ag) are supposed as ideal Schottky contact for GaN due to its barrier highest (SBH) values [4]. Current-Voltage (I-V) measurements use to determine SBH depend on thermionic emission at V>3kT as following [5]:

$$I = I_0 exp[qV/(nkT)] \tag{1}$$

$$I_0 = AA^{**}T^2 \exp\left[-q\phi_B/kT\right] \tag{2}$$

where q, is the electron charge, V is the applied voltage, n represents the ideal factor, k represented the Boltzmann's constant,  $I_o$  represented the saturation current,  $\Phi B$  represented the barrier height, T represented the absolute temperature, A represented the area of the Schottky contact and  $A^{**}$  represented the Richardson coefficient. The theoretical value of  $A^{**}$  calculated as shown below:

$$A^{**} = 4\pi m * qk^2/h^3 \tag{3}$$

(3) Where  $m^*$  represented the effective electron mass and h represented the Planck's constant or AlInGaN. The literature on the effective mass of the electron in AlInGaN had not mentioned in the literature before, therefore the effective mass of AlxInyGa1-x-yN with different x, y has calculated depending on the theoretical value of AlN which  $m^*=0.4m_{\circ}$  (m0 is electron rest mass), of InN which  $m^*=0.11m_{\circ}$  and of GaN which  $m^*=0.2$   $m_{\circ}$  [6].

I-V characteristics for such devices analyzed at reverse bias using the equation as following [7]:

$$I = I_0 \exp(qv/nKT)[1 - \exp(-qv/kT)]$$
(4)

Thus, Eq. 4 can be re-written in the form [7]

$$I \exp(qv/kT)/\exp(qv/kT) - 1 = I_0 \exp(qv/nkT)$$
(5)

Based on Eq. (5), the plot of ln [I exp (qV/kT)/ exp (qV/kT)-1] against V will give a straight line.

In this paper the performance of Au, Ag/ Al0.08In0.08Ga0.84N/Au, Ag MSM PDs depend on SBH, n, Responsivity, quantum efficiency, and NEP have been examined.

### **Experimental Work**

The commercial samples of n- Al<sub>0.08</sub>In<sub>0.08</sub>Ga<sub>0.84</sub>N grown by using molecular beam epitaxy (MBE) on a silicon substrate were employed. The Radio Corporation of America (RCA) cleaning at room temperature was carried out before any fabrication process to remove any contaminations on the wafers. The procedure includes using NH4OH:H2O=1:20 solutions for 10 minutes, then washed with deionized water. Subsequently, the samples were dipped into HF:H2O=1:50 for 10 seconds then, washed again with deionized water. The cleaned samples were then chemically etched in boiling aqua regia of HCl: HNO3=3:1 for 10 minutes to reduce the amount of oxygen (O) and carbon (C) contamination of the Al<sub>0.08</sub>In<sub>0.08</sub>Ga<sub>0.84</sub>N and Si surface. Wafers were then blown dry with compressed air after cleaning. Quaternary Al<sub>0.08</sub>In<sub>0.08</sub>Ga<sub>0.84</sub>N sample must be prepared before depositing the metal contacts and then fabricating the devices.

Silver (Ag) and gold (Au) metal contacts have been deposited on Al<sub>0.08</sub>In<sub>0.08</sub>Ga<sub>0.84</sub>N film as Schottky contacts because of its high work function which equal to 5.4 eV. Au (99.9 purity) Schottky contact deposited on Al<sub>0.08</sub>In<sub>0.08</sub>Ga<sub>0.84</sub>N films grown on Si substrate was fabricated using a metal mask of 250 nm by A500 DC sputtering system while Ag contact was fabricated using the screen print method which considers as a first time as best our knowledge with the optimal condition to select the best metal for MSM photodetectors (PDs).

Then, the gold contact with a thickness of 200 nm was reached for different temperatures ranged from 400to 600 °C with different times of 15,30, 45 minutes, and 1hour to optimize the best condition for the device. The topography of Au schottky contact with different annealing temperatures and various times have been examined and optimized using SEM and AFM spectroscopes I-V characteristic of Au, Ag/n- Al<sub>0.08</sub>In<sub>0.08</sub>Ga<sub>0.84</sub>N /Au, Ag MSM carried out using UIR-210A spectrophotometer range from 200 to 1000 nm wavelengths as shown in Figure .2. Using this setting the photocurrent, dark current and I-V measurements were measured and, ideality factors and SBH were calculated.

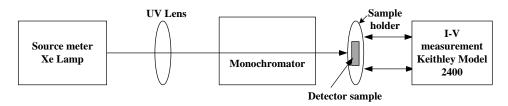


Figure 2 A typical set up of the spectral response measurements of Alo.o8Ino.o8Gao.84N -based MSM UV PDs

#### **Results and discussion**

Au and Ag metals have been used as a Schottky contact in the thin film n- Al<sub>0.08</sub>In<sub>0.08</sub>Ga<sub>0.84</sub>N grown on Si (111) substrate. Effect of annealing temperature of As deposit, 400, 500, and 600 C0 for 30 min on the topography and electrical properties of Au contact have been characterized and optimized.

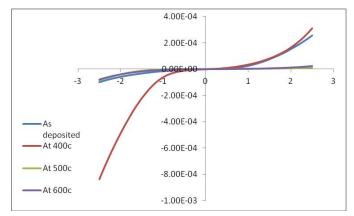


Figure 3 I-V measurements of Au Schottky contact at different annealing temperatures.

I-V characteristics to study the effects of these parameters on electrical properties of films examined by calculated SBH. Figure 3 shows the I-V property of Au/ Al<sub>0.08</sub>In<sub>0.08</sub>Ga<sub>0.84</sub>N Schottky contacts as deposited, 400, 500, 600 °C for 30 minutes on Si substrates annealing temperature were determined and ideality factors were 1.223 eV and 1.773 of Au/AlInGaN at 50C0 annealing temperature for 30 min. Also, with the same procedure the effect of annealing time of 15,30,45 minutes, and 1hour have been studied and optimized as shown in Figure (4) There results revealed that the best annealing time is 30 min which has the highest SBH.

To be sure that Au contact is the best selection between metals, the comparison with Ag contact has been done with the optimal condition get from the characterization of Au contact. I-V curve of Ag contact deposition AlInGaN prepared by screen print presented in Figure (5).

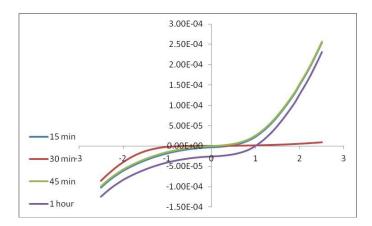


Figure 4 I-V measurements at effect of annealing time of Au Schottky contact deposited on the thin film Al<sub>0.08</sub>In<sub>0.08</sub>Ga<sub>0.84</sub>N grown on then-Si substrates.

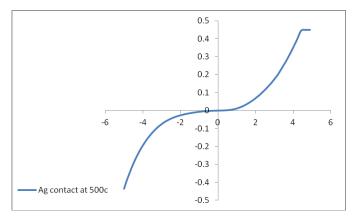


Figure 5: I-V curve of Ag contact at 50 °C deposit on AlInGaN.

These results of the Au and Ag metal at 500 0C annealing temperature for 30 min showed that the Au metal at 500 CO annealing temperature for 30 min has the highest SBH and low ideality factor in comparison with Ag metal contact as shown in Table 1.

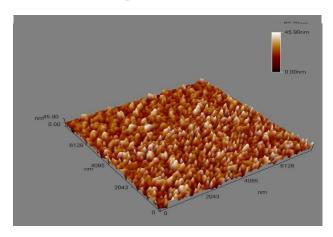
Table 1 SBH, ideality factor of Schottky contacts of films n- AloosIno.osGao.s4N grown on Si substrate with different temperature.

Electrode	Annealing temperature ( <sup>0</sup> C)	Time (min)	Schottky barrier highest SBH (eV)	Ideality factor (n)
Au	500	30	1.223	1.773
Ag	500	30	1.021	1.883

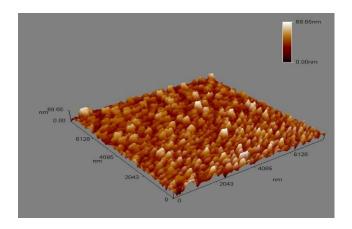
To confirm the I-V characteristics of the previous results regarding Au contact the topography test have been examined on As deposited, 400, 500, and 600 0C for 30 min which including Average diameter, Root mean square, and Roughness Despite, different annealing temperatures have been used, there is no phase change was observed, therefore the optimal annealing temperature is 500°C due to its high RMS which makes more incident beam absorbed inside the layers by increased the quantum confinement probability since its

crystalline size is 41 nm depend on Sherrier's formula [8] and bring the quantum effect to appear clearly as shown in Figures 6 and Table (2)

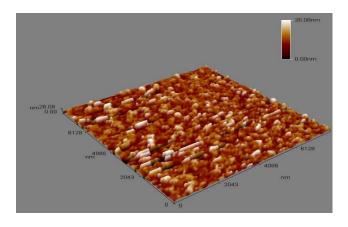
### As deposited



### At 400 °C



### At 500 $^{0}$ C



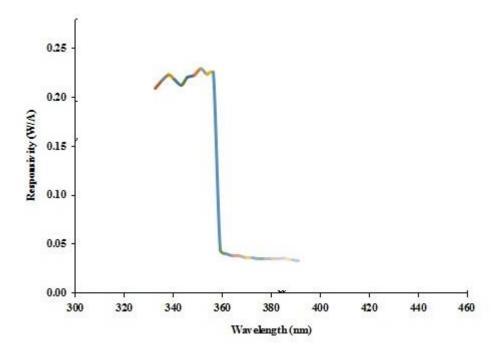
At 600  $^{0}$ C

Figure 6: AFM measurements of Au Schottky contact at various annealing temperatures.

Table 2: Average diameter, RMS, and Roughness of the Au contact of Al<sub>0.08</sub>In<sub>0.08</sub>Ga<sub>0.84</sub>N films on Si substrate.

Sample	d(nm)	RMS (nm)	Roughness
As deposited	58.19	2.89	1.7
400	119.09	9.22	7.36
500	91.63	10.3	8.11
600	75.46	4.95	3.79

Figures 7 and 8. Shows the responsivity as a function of the wavelength of the Au and Ag/  $Al_{0.08}In_{0.08}Ga_{0.84}N$  MSM photodetector grown on Si substrate, respectively. Responsivities photodetector is constant over the energy bandgap (UV region from 300 nm to 370 nm) with two orders of magnitude high cut-off drop in wavelength at 360 nm. The responsivities of Au, Ag/  $Al_{0.08}In_{0.08}Ga_{0.84}N$  /Au, Ag MSM photodetectors were 0.201 A W-1 and 0.153 A W-1. In addition, QE of Au, Ag/  $Al_{0.08}In_{0.08}Ga_{0.84}N$  /Au, Ag MSM photodetector son the Si substrate was 71.5% and 57%, respectively.



 $\label{eq:Figure 7: Responsivity of Au / Al} In_{0.08} In_{0.08} Ga_{0.84} N \ \text{MSM photodetectors grown on the Si substrate.}$ 

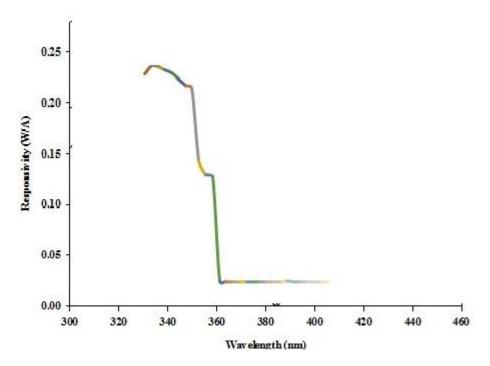


Figure 8 Responsivity of Ag/Al<sub>0.08</sub>In<sub>0.08</sub>Ga<sub>0.84</sub>NMSM photodetectors grown on Si substrate.

noise equivalent power (NEP) of Au,Ag/  $Al_{0.08}In_{0.08}Ga_{0.84}N$  /Au,Ag MSM photodetectors were on the Si substrate  $3.55\times10-4$  and  $1.45\times10-3$  W-1, respectively, as shown in Figures 7 and 8, calculated that Au metal has the high SBH and high QE of samples grown on Si substrates as summarized in Table 3.

Table (3): Dark and illumination current, responsivity, QE, ideality factor and SBH of Au, and Ag/  $Al_{0.08}In_{0.08}Ga_{0.84}N$  MSM photodetectors grown on the Si substrate.

Electrode	Id(A)	Iph(A)	$R(AW^{-1})$	η%	n	SBH(eV)
Au	6.87*10 <sup>-5</sup>	7.14*10 <sup>-5</sup>	0.201	71.5	1.773	1.223
Ag	2.20*10 <sup>-4</sup>	2.22*10 <sup>-4</sup>	0.153	57	1.883	21.2

### Conclusion

High work function metals Au successfully used as Schottky contact on n-Al0.08In0.08Ga0.84N thin film which grown on Si (111) substrate. The effect of annealing temperature of  $500\,^\circ$ c for 30 min. The electrical characteristics of these effected as well were examined through I-V measurements and their SBH values were computed. The SBH value can be deduced directly from the I-V curves, the computations of SBH and ideality factor (n) at the Au/ Al0.08In0.08Ga0.84N interface for the sample annealed at  $500\,^\circ$ C. Au contact have a higher barrier height when the annealing was performed at  $500\,^\circ$ C for 30 minutes which yielded around 1.223 eV.

The ideal characterization of Au /AlInGaN/Au MSM PD Si substrate based on responsivity of 0.201~A~W-1, quantum efficiencies of 71.5%.

Au metal has the highest SBH, the highest QE and a low dark current for the samples grown on Si substrates.

### References

[1] Wu, J., Li, D., Lu, Y., Han, X., Li, J., Wei, H., Kang, T., Wang, X., Liu, X., Zhu, Q., Wang, Z., (2004). Crack-free InAlGaN quaternary alloy films grown on Si (111) substrate by MOCVD. J. Crystal Growth, 273, pp.79-85.

[2] Aumer, M. E., LeBoeuf, S. F., Moody, B. F., & Bedair, S.M. (2001). Strain-induced piezoelectric field effects on light emission energy and intensity from AlInGaN/InGaN quantum wells. Appl. Phys. Lett., 79,pp. 3803-3805.

- [3] Liu, K., Sakurai, M., & Aono, M. (2010). ZnO-based ultraviolet photodetectors. Sensors, Vol.10, pp. 8605-8630.
- [4] Schroder, E. F. (2006). Light-Emitting Diodes (2nd Ed.): Cambridge University press.
- [5] Mohammad, S. N., Fan, Z., Botchkarev, A. E., Kim, W., Aktas, O., Salvador, A., (1996). Near-ideal platinum-GaN Schottky diodes. Electron. Lett, 32, pp. 598-599.
- [6] Averine, S., Chan, Y. C., & Lam, Y. L. (2000). Evaluation of Schottky contact parameters in metal-semiconductor-metal photodiode structures. Appl. Phys. Lett., 77, pp. 274-276.
- [7] Ghazai, A. J, Hassan, H. A, Hassan, Z, Hussein, A, (2013) Effects of thermal annealing on Ti/Al Ohmic contacts on quaternary n-Al 0.08 In 0.08 Ga 0.84 N alloy film., International Journal of Nanoelectronics & Materials, 6 (2), pp. 113-119
- [8] Alaa Jabbar Ghazai, Haslan Abu Hassan, Zanuri Bint Hassan (2016). Structural and optical properties of Si-doped Al0.08In0.08Ga0.84N thin films grown on different substrates for optoelectronic devices, Superlattices and Microstructures, 95, pp 95-107.





# raqi Journal of Nanotechnology IJN

synthesis and application







